INFLUENCE OF INDUCTION WELDING ON PEKK CRYSTALLIZATION

A COMPUTATIONAL, ANALYTICAL AND EXPERIMENTAL INVESTIGATION

Master thesis

to obtain the degree Master of Science
at the Technical Universiteit Delft,
on the authority of prof. M.A. Bessa,
in het openbaar te verdedigen op dinsdag 1 januari 2015 om 10:00 uur

door

Siard KUIPERS

master of science,
Material science and engineering, Technical university, Delft,
Born at Leiden, Netherlands.

This master thesis is approved by

promotor: Prof. dr. I.M. Richardson

formation defence committee:

prof. dr. M.A. Bessa, Technische Universiteit Delft

Independent members:
Prof. dr. I.M. Richardson
Technische Universiteit Delft
Dr. ir. M. Hagenbeek Technische Universiteit Delft

Other members:
Msc. A. mitrousias, Technische Universiteit Delft

Prof. dr. ir. M. Bessa has contributed significantly to the realization of the master thesis.

Keywords: PEKK, Crystallization, Isoconversional method, Optimazation, Induction welding
Printed by: Siard Kuipers
Front & Back: Beautiful cover art that captures the entire content of this thesis in a single illustration.

ISBN 000-00-0000-000-0

An electronic version of this dissertation is available at
http://repository.tudelft.nl/.

Sometimes something's got to happen
before something is going to happen .

Johan Cruyf

CONTENTS

SUMMARY

Current studies about crystallization kinetics of polymers are aimed at Differential Scanning Calorimetry (DSC), characterized by constant conditions of temperature, cooling and heating rate. This is of limited use to industry, as non constant cooling/ heating rates occur during most manufacturing processes. This research is aimed at predicting the crystallization kinetics for non constant cooling rates of carbon fibre (CF) and Polyetherketoneketone (PEKK) during the induction welding process.

An analytical model on the basis of the isoconversional method is developed and coupled to multi physics finite element simulations to investigate the effect of process parameters on the degree of crystallinity at the weld interface. The study was validated by static and dynamic welding experiments. Careful setting of the process parameters has to be chosen to result in an increase of the degree of crystallinity at the weld interface. Using the proposed models welding times were adjusted to optimize the degree of crystallinity at the weld interface.

The models are able to establish a relation between an arbitrary thermal program and the degree of crystallinity produced during this program. Linking the crystallization model to the simulations allowed investigation of the crystallinity throughout the work piece, which is not possible to do with experiments only. It was found that induction welding results in a localized heat point, which will result in fast cooling rates at the weld interface. In contrast to previous studies, our research is able to relate the crystallinity to non constant cooling programs, which allows direct application in the induction welding process.

1

INTRODUCTION

Thermoplastic matrix materials are advantageous over thermoset matrix composites in the way that they provide superior damage tolerance; shorter production cycles; inherent recyclability and weldability. However the need to establish new fabrication techniques and suitable joining methods has been a barrier to the introduction of thermoplastic composites. Robotics fiber placement shows to be a promising technique to manufacture complex components [1]. Typically, efficient fibre placement systems use unidirectional (UD) tapes. In particular, Fokker has already applied robotic fibre placement of carbon fibre reinforced PEKK to manufacture the tailwing of the Gulfstream G650 [2]. Induction welding in the gulfstream G650 was proven to reduce the weight as there was no need for additions fasteners [3] and increased the joining strength [2]. This research will focus on the induction welding of UD carbon fibre reinforced PEKK materials, without the use of a susceptor at the bondline.

PEKK is a semi-crystalline polymer and its the degree of crystallinity on it's processing conditions. PEKK has relatively slow crystallization kinetics compared to other semi-crystalline polymers. Induction welding with arbitrary process parameters could lead to insufficient crystallinity at the bondline.

This research sets itself apart because it focuses on the relationship between welding parameters, crystallinity and the mechanical bond strength. Knowing that crystallinity has a direct correlation with the mechanical properties of the thermoplastic composites[4]. The goal of this research is to predict the crystal development from the temperature distribution predicted by a computational model this enables to optimize the process parameter that control the quality of the weld and thus establish high quality joints.

1

1.1. INTRODUCTION INTO INDUCTION WELDING

Compared to other fusion bonding processes induction welding is unique in that it requires no contact between induction coil or the heat susceptor to fuse two opaque parts. It offers parameters to design the process such that heat outside the weld area is minimized. This makes the process very versatile and applicable to with the a wide range of materials capable to weld [6].

In induction welding an alternating voltage is passed across a conductive coil producing a alternating current within the coil. The current produces a magnetic field and the magnetic field alternates with the same frequency as the current. The part, which is to be welded needs to contain a magnetically susceptible and electrically conductive material (conductive carbon fibres or a metal mesh). When placed in the proximity of the magnetic field introduced by the coil, eddy currents are produced. The eddy currents equal the frequency of the alternating current. For eddy currents to exist the material must contain closed-loop circuits. In the case of Carbon fibre reinforced thermoplastics, the carbon fibres form a conductive network (woven fabrics or cross plies for example) that form closed-loops. Heat is produced by the energy lost by the eddy currents as a result of the material resistance. The stacking sequence and fibre orientation affect the mechanism of heating. The different mechanism of heating and the effect of fibre architecture are discussed in section 1.1.2. In order to complete the induction welding, pressure needs to be applied for sufficient diffusion of the polymers chains.

1.1.1. SET UP

The basic induction welding set-up, can be generalized into four main parts [7]. The first is the radio frequency power generator, supplying the alternating current and voltage to the induction coil. The second, the heat station which contains the induction coil. The third is the composites part being welded. The final part, is the secondary equipment: for example the water cooling system of the heat sink.

Power source

There are two models of induction power sources: the solid state and the vacuum tube [8]. The higher efficiency of the solid state power sources, makes them preferred, if available [9]. They supply frequencies up to 1 MHz. They are generally smaller than vacuum tube and have a higher efficiency of 85% -95%.

Heat station

The energy from the power source is transferred to the composite part by the induction coil. The energy transfer is similar to a transformer [10], where the induction coil is the primary coil and the conductive network in the composite is the secondary coil. Just as in the case of transformers, the goal is to strive for 100% coupling efficiency. This is achieved if 100% of the power provided is converted through the air to the composite. As in accordance to the transformer law $I_m = N_c I_c$ where the subscripts m and c express the composite material and the coil respectively and N_c is the number of winding of the

coil. The energy generated in the composite can be calculate by:

$$E_m = P_m t = I_m^2 R_m t = N_c^2 I_c^2 R_m t \tag{1.1}$$

Since the coil and the composite are isolated by air, 100% coupling efficiency is never reached, so an efficiency factor should be introduced in equation 1.1. Finding the correct efficiency factor is a complex procedure as it depends on many parameters. Examples of these parameters are, the distance between the coil and the composite, As well as the fibre architecture of the composite and the geometry of the coil. In general, its assumed that the coil should be placed as close as possible to the composite to maximize the coupling efficiency [11]. In order to produce the most efficient and uniform heating effect, one must consider the following design considerations for the coil geometry:

- The magnetic flux density decreases with increasing distance from the coil. Placing the composites as close as possible to the coil increases the coupling efficiency and assures maximum energy transfer [12].
- Symmetric parallel part in the coil which need to be prevented because it cancels out the magnetic field, and distances between parallel parts need to be altered to restrain field cancellations [11].
- The connection of the heat station to the coil affects the shape of the magnetic field, the cancelling of the magnetic field by two parallel connections resulting in a asymmetric field. Hence a asymmetric magnetic field results in asymmetric heating [11].
- The high frequencies used with composite welding can cause overloading and arcing between coil passages [7].

Composite

The voltage, power and frequency can be adjusted to achieve the highest energy transfer between the coil and the composite. The maximum efficiency of the coil itself can be reached at the resonant frequency of the coil. The input characteristics are designed to match the desired input for the composite [8].

Heatsink

The purpose of the heatsink is to alter the through thickness heat distribution within the composite, from the surface to the weld bond. The heat sink should be designed such that it converts the heat away from the composite. As a result the temperature at the surface is lowered and a reverse heat distribution is formed, preventing degradation of the material at the surface. The material of the heat sink should be chosen in such a way the generation of eddy currents is prevented, as this energy is not used for the weld and decreases the efficiency [13].

1.1.2. HEATING MECHANISMS

The magnetic field creates heat within the composite, but where and how the heat is created depends on the material properties and the fibre architecture. Conductive carbon fibres are able to act as the susceptor and no metal mesh inserts are needed. The

1

presence of a metal mesh can weaken the fusion bond and its placement is an extra production step adding cost and time to the process [14].

The magnetic field induces eddy currents in the composites if there are conductive loops present. The long and directional Carbon fibres prevent formation of conductive loops and this restriction of travel possibilities for electrons so called resistance of the fibres, causes the electrons to lose energy creating heat,

$$E = I^2 R t \tag{1.2}$$

. Where I is the current and R is the resistance and t is the time the magnetic field is applied. The resistance is influenced, by the material properties, electrical resistance, specific heat and magnetic permeability. The rate of heating is dependent on these material properties, the frequency and the eddy current [9]. The eddy current, produced by the magnetic field, creates its own small magnetic field, which hinders deeper penetration of the composite by the magnetic field of the coil [12]. The current within the composite moves along the path of least resistance, for example the conductive carbon fibres. The stacking of these conductive paths influence the path of the eddy currents, perpendicular stack prepregs show a more rectangular mirror image of the coil. Whereas woven plies produce a more circular image. This is due to more direct contact point of the fibres in the woven plies [12]. The same principle is illustrated in figure 1.1, where addition of 45 and -45 plies results in a more circular heating pattern, better mirroring the shape of the magnetic field. How the fibre architecture of the composites affects the heating generation has been a source of much discussion and two categories of heating are recognized in carbon fibre composites, namely fibre heating and junction heating [15]. The heating mechanisms will be discussed next.

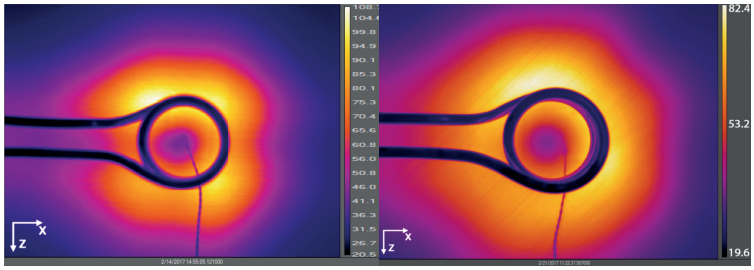

Figure 1.1: Heating pattern of UD $[0/90]_{2s}$ and Heating pattern of UD $[0/90/45/-45]_s$

Fiber heating

Joule loss results in heating of the fibres, due to the inherent resistance of the fibres. The inherent resistance, $R = \frac{\rho L}{A}$ is dependent on the ρ fibres resistivity, L the fibre length and A the cross section of the fibre. Lin et al. compared the heating of woven carbon fibre/PPS versus plain woven carbon fibres and found negligible difference between the two, concluding that the heat was produced by fibre heating [16]. For fibre heating to occur very low contact resistance between the fibres has to be present [15].

Junction heating

Two types of junction heating are distinguished, heating with a isolating polymer layer and heating with direct contact between the fibres. In general, in the production of prepregs and UD tapes the carbon fibres are enclosed on the tops by thin layer of isolating matrix material. This isolating material acts like a capacitor, upon the application of the electric field induced by the magnetic field. There is a potential created between two fibres and the dielectric heating that occurs due to the movement of charge across the matrix material and the rotation of the dipoles of the molecules between the fibres[17]. The junction heating can be expressed as a loop with a parallel placed resistor and capacitor. The resistance of the dielectric material can be calculated by [18]:

$$R_{dh} = \frac{h}{w\epsilon_0 k d_f^2 \tan\delta} \tag{1.3}$$

Where h and e_0 are the distance between two fibres and the permittivity of a vacuum respectively. k and $\tan\delta$ are the dielectric constant and the dissipation factor of the isolating matrix material, and d_f is the diameter of the carbon fibre. w is the angular frequency. Gillespie et al. concluded that for maximum junction heating of cross - and angle ply laminates, the fibre volume fraction and ply thickness above and below the interface should be maximized. The material between the fibres and the fibre diameter should be minimized [19].

If there is no isolating polymer layer between the layers and direct contact between the fibers exist heating occurs by contact resistance heating. In angled plies with high fiber volume fraction, the number of direct contact might be high and contact heating may be dominant. The resistance at the contact and the voltage drop across the fibers determine the rate of heat [15]. The resistance at the junction has a large dependence on the temperature and pressure [15]. Contact resistance heating can also take place if there is a very small layer of polymer in between, provided that electrons are able to pass through this small layer. The application of pressure during fabrication can lead to squeeze flow of the matrix and fiber waviness increasing number of contact points [20]. For uniform heating by contact resistance heating there must be a uniform distribution of contact points and a higher extent of contact results in better heating [21].

1.1.3. SECONDARY HEATING EFFECTS

The most pronounced issue in induction heat is the edge effect. The closed-loops of eddy current induced by the coil try to mirror the coil. Eddy current loops are not able to loop outside the composite part and to mirror the magnetic field of the coil the best as possible the eddy current is forced to travel as close as possible to the edge of the composite. Resulting in a higher current density at the edge and higher temperatures at the edges. [12].

1.1.4. PROCESSING PARAMETERS

Frequency

The current frequency dictates, the alternating magnetic field induces eddy current within the composite. A higher frequency results in a higher conductivity and lower penetration

1

due the cancellation of the coils magnetic field in deeper depths of the composite as illustrated in figure 1.2 [22]. Increasing the frequency results in quadratic decrease of time to heat the composite to the desired temperature [23]. So there is a balance between the penetration depth and the energy generated in the composite.

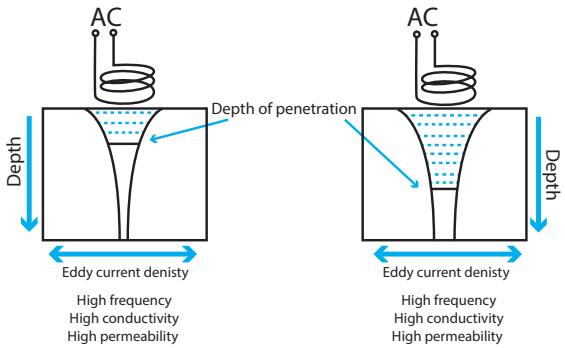

Figure 1.2: The effect of frequency on the penetration depth, conductivity and permeability [24].

Power

The amount of power generated in the composite is proportional to the power input. As described above there is a strong coupling between the power input in the coil and the power generated in the composite just like a transformer and the power generated is expressed as [23]:

$$P = \frac{(2\pi f \mu_r H(I) A)^2}{R} \tag{1.4}$$

Where μ_r is the magnetic permeability, f is the frequency and $H(I)$ is the magnetic field intensity with dependence on the current at the coil. A and R is the cross-sectional area of the conductive loop in the composite and the electrical resistance of the carbon fibres respectively. Increasing the frequency can compensate for increasing the coil distance and the resulting decrease in power.

Pressure

Pressure is important for good consolidation because it allows good intimate contact and diffusion. There is an optimum in the pressure applied, as high pressure results in matrix squeeze out and results in lower quality of the weld and with low pressure there is not enough intimate contact.

Residence time

The time of exposure of the composite to the magnetic field is called the residence time and influences the diffusion of the polymers chains across the interface. Longer residence time results in higher quality of weld because the chains get sufficient time to diffuse across the interface [25, 26]. For insufficient weld times the chains don't get sufficient time to diffuse across the interface, but for longer welding times where the temperature exceeds the maximum welding temperature of the composite, thermal degradation

of the polymer results in a decrease of the weld strength. An optimum time of exposure to the induction field resulting in a high quality weld has to be found.

2

THEORETICAL FRAMEWORK

The theoretical framework will introduce the concepts together with their definitions and the relevant literature, necessary for this research. The theory within the framework is aimed towards the Poly(aryl Ether Ketone Ketone) and the crystallization of the polymer. The literature is selected on its appropriateness, ease of application and explanatory power. Of the nature and challenges associated with crystallization of PEKK during induction welding.

2.1. MATERIAL

PAEKs

Poly(aryl Ether Ketone Ketone) (PEKK) is a member of the high-temperature, high-performance thermoplastic family of Poly(Aryl Ether Ketone)s (PAEKs). This family is known for their useful properties, for instance their high melting temperature (T_m); glass transition temperature (T_g); superior mechanical properties [27]; wide range of attainable crystallinity[28]; low flammability[29] and excellent chemical resistance[30].

The first member of the PAEKs family that was developed and commercialized was poly(aryl Ether Ether Ketone) (PEEK). Due to its pervasive use in scientific studies and industrial applications in the last decades [31–34], as well as the similarities to PEKK,[35, 36] this material will be referred frequently in this study. PEEK just like PEKK and other PEAKs is a semi-crystalline polymer characterized by sequences of aryl ether and aryl ketone functionalities in the backbone [37]. Fig. 2.1 shows the chemical structure of the repeated unit of PEEK. The chains adopt a zigzag conformation in a orthorhombic unit cell, with chains in the b-c plane and two chains in each cell (fig. 2.1). The dimensions of the unit cell for the crystal form are $a = 0.776$ nm, $b = 0.589$ nm and fibre axis $c = 0.995$ nm [38], PEEK shows no polymorphism [39]. and its melting temperature is recorded to be around 335 °C. During annealing the bulk crystallinity can reach about 45% in volume, from a nearly completely amorphous state produced by rapidly quenching from the melt. [40]

PAEKs are regarded as 'low-crystallinity' polymers, since they contain aromatic groups in their backbone [41]. The presence of crystalline regions in these polymers leads to the constraint of amorphous mobility. This process results in a positive offset of the T_g in the order of 10-20 °C for semicrystalline specimens [42]. The degree of crystallization and the imposed constrains on the motion of the amorphous phase is a function of the thermal history and the corresponding morphology that develops [43].

PEKK

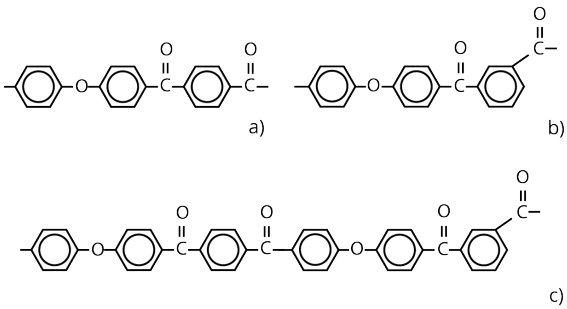

Figure 2.2: Chemical structures of the three different homopolymers of PEKK. a) all paraphenyle linkages, PEKK(T) b) one meta-phenylene linkage, PEKK(I), c) Homopolymer of perfectly alternating PEKK(I) and PEKK(T) in a 50/50 ratio [45]

Dupont was the first to manufacture PEKK, which is prepared in a more economical synthetic route than PEEK. It is a synthesis by Friedel-crafts polycondensation of diphenyl

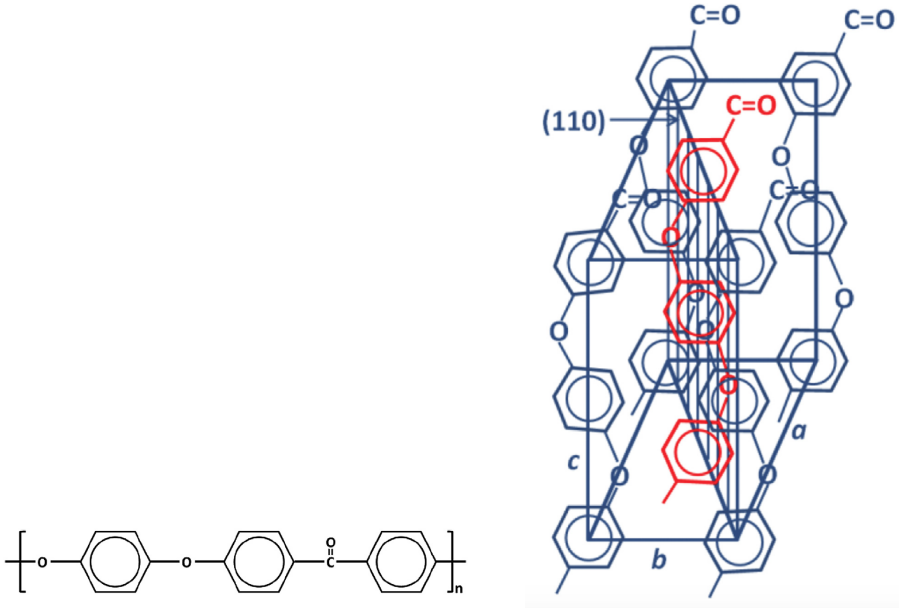

(a) Chemical structure of repeat unit of PEEK [44]

(b) (b) Unit cell of PEEK [44].

Figure 2.1: Spacial chemical orrientation PEEK

ether (DPE), terephthaloyl chloride (T) and/or isophthaloyl (I). [28]. The syntheses results in two basic structures differing in the connection point of the carbonyl link. The carbonyl connected on the fourth carbon atom has only para-phenyle linkages and is indicated as PEKK(T). The second isomer has it's carbonyl connection on the third carbon atom of the aromatic ring and has one meta-phenylene linkage in the backbone, so it is called PEKK(I)

The two isomers can be combined to form three different homopolymers, the two indicated above (T and I) and a PEKK(T/I) homopolymer containing perfectly alternating T and I isomers. It's chemical structure is shown in fig. 2.2 c. By combining different ratios of T and I different copolymers can be formed. Different ratios and stacking sequences affect the structure, morphology and properties of copolymers. This provides the manufacturers of PEKK the possibility to tailor the chemical composition and stacking sequences to reach the desired properties [28].

Compared to other PAEK's PEKK has a higher percentage of keto linkages, 67%. Keto linkages are more rigid than ether linkages [46], resulting in a higher melting temperature (T_m) of 360 °C to 380 °C as compared to PEEK which has a T_m of around 340 °C [47]. Pure PEKK(T) with a 100% T/I ratio has the highest T_g and T_m among all PEKK's ($T_g \approx 165$ °C). However, pure PEKK(T) has a melting point too close to its combustion temperature of 400 °C, limiting its practical use. Fortunately, one of the greatest advantages of PEKK over PEEK is that the melting point can be altered by changing its composition [48]. The addition of meta linkages increases flexibility of the chains and leads to a

large reduction in the melting point together with a modest decrease in glass transition temperature. Krishnaswamy et al. [43] researched the crystallinity of different (T/I) ratios of PEKK concluding that increasing meta content resulted in a decrease of the degree of crystallinity. As a consequence introducing the Isophathalate units in the backbone leads to a decrease in crystallization rate [48]. The increase in flexibility by addition of these units also reduces the constraint of the chains imposed by the crystalline phase as compared to the PEKK(100/0) homopolymer.

MORPHOLOGY

PEKK shows two stable crystalline polymorphs, unlike PEEK which has a single crystalline modification. Form 1 is the conventional structure similar to the structure of PEEK, while form 2 is a different structure that can only be obtained by cold crystallization (fig. 2.3) [38]. Gardner et al characterized the influence of the T/I ratio on the formation of the two crystal structures. They tested six different T/I ratios: 100/0, 90/10, 80/20, 70/30, 60/40, 50/50. All para-phenylene linkages (100/0) show the same diffraction pattern as PEEK, this diffraction pattern is indexed by a two-chain orthorhombic unit cell with $a = 0.769$ nm, $b = 0.606$ nm and $c = 1.016$ nm with the axes indicated as in fig. 2.1.

The addition of a meta-phenylene linkage in the backbone, results in the formation of a second structure during cold crystallization, indicated as form 2. The increased chain flexibility results in higher melting peaks. This is associated with a recrystallization or reorganization process in which the crystal structure rearranges to a more perfect configuration after premelting [48]. The remelting is associated with the transformation of form 2 into form 1. Both forms fold their chains along the a-axis. Increasing I ratio seems to hinder crystal growth, due to the increased asymmetry by introduction of the metaphenyle linkages. This leads to a decrease in crystallization rate but, an increase in both chain flexibility and recrystallization ability.
Isothermal data of PEKK shows double melting peaks. This double melting behavior is also reported for PEEK [49, 50]. The melting of two crystalline regions is the explanation for this phenomenon, where the higher peak corresponds to the melting of the more perfectly organized crystalline region and the lower peak is attributed to the melting of a more imperfectly organized crystalline region [51].

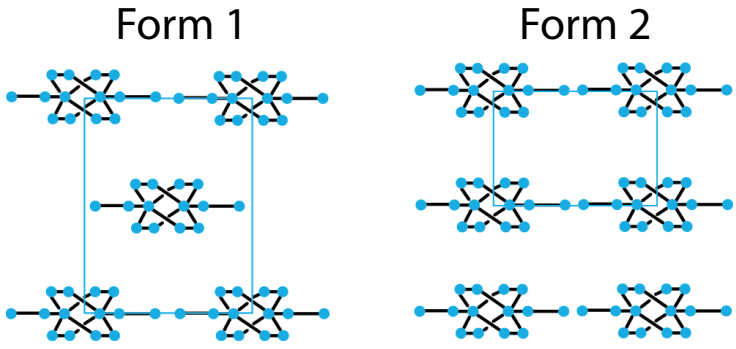

Figure 2.3: Schematic drawing of chain packing forms, form 1 and form 2 [48].

EQUILIBRIUM MELTING TEMPERATURE

The equilibrium melting temperature is the melting point for an infinite crystal. Experimentally it's found that for medium and high molecular weight the melting point only depends upon the thickness of the lamellae and not upon the molecular weight [52]. Gardner et al. [48] established a clear dependence of the equilibrium melting temperature on the isophthalate content. An increase in isophthalate content decreases the equilibrium melting temperature. Fig. 2.4 shows the linear dependence of equilibrium melting temperature as a function of the terephthalate content. The T_m^0 is an important value since it is the reference temperature from which the driving force for crystallization is determined.

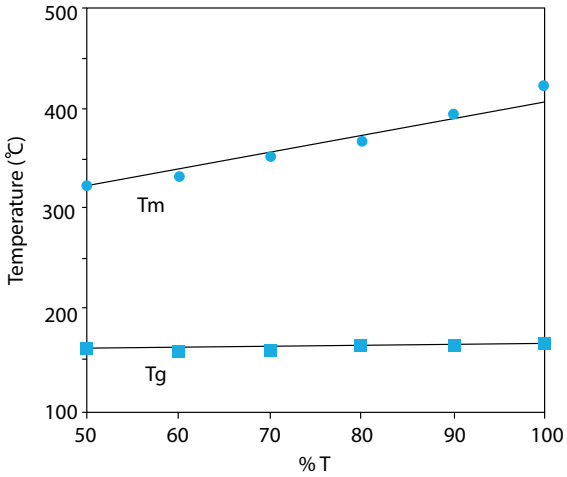

Figure 2.4: The extrapolated equilibrium melting temperature and T_g vs. terephthalate content (T) [48]

The heat of fusion needed to melt a crystal of infinite proportion is denoted as $\Delta H_{100\%}$. In Differential Scanning Calorimetry (DSC) the melting enthalpy of the theoretical 100% crystalline polymer is used to compute the fractional degree of crystallinity χ_c.

$$\chi_c = \frac{\Delta H_c}{\Delta H_{100\%}} \cdot 100 \tag{2.1}$$

Where ΔH_c is the heat of crystallization. Equation 2.1 is only valid for neat polymers, the equation must be modified to account for the use of reinforcements. To account for the reinforcement content eq (2.1) becomes:

$$\chi_c = \frac{\Delta H_c}{\Delta H_{100\%}(1 - W_f)} \cdot 100 \tag{2.2}$$

where W_f is the weight fraction of the reinforcements. The heat of fusion for a 100% crystalline PEEK was determined by Blundell and Osborn as approximately 130 J/g [53]. Chang and Hsiao found the same value for PEKK by using the density method with the theoretical density for 100% crystalline PEKK as 1.402 g/cm^3 [48] and 1.278 g/cm^3 for

Table 2.1: Overview material properties PEKK

Property	Value	Source
Density [1]	1.278 [g/cm^3]	[54]
Glass transition[2]	198 [°C]	DSC experiments
Melting peak temperature [2]	337 [°C]	DSC experiments
Processing temperature	350-380 [°C]	[54]
Dielectric constant	3.6	[54]
Dielectric loss	0.003	[54]
Volume resisitivity	$5.4 \cdot 10^{14}$ [ω]	[54]
Coefficient of thermal expansion	50.52 [μ/m/°C]	[54]
Specific heat [3]	0.72	DSC experiments

completely amorphous. They were able to extrapolate the data versus the heat of fusion to obtain the heat of fusion for a 100% crystalline PEKK. An overview of the PEKK material properties is provided in table 2.1.

2.2. CRYSTALLIZATION

The long chain nature of polymers gives rise to highly complex and diverse growth forms. This complicates the crystallization characterization. Keller [55] was one of the pioneers in crystallization theory by formulating the hypothesis that lamellae are formed by the folding of chains upon themselves in a regular fashion. Crystalline polymers in general take the form of thin lamellae, which are unrestricted in two dimensions but are bound in the third by the folds that establish the basal plane. The thickness and growth rate of the lamellae depend on temperature and supercooling, morphological aspects are generally not decided by cooling rate [56]. A common fundamental basis for crystal theory is the crystalline model (fig. 2.5). In the crystalline model a chain is folded perpendicular to the fold surface. This model offers a very simplified view of a real crystal, given that the latter involves many defects, dislocations and entanglements. Re-entry of chains is found to be the predominant process for chain depositing on the lamellae surface. Re-entry is the folding of a chain upon the surface from a chain already present on lamellae, loops or cilia are described as occasional disruptions of the re-entry process [57]. Molecular motion in the system is responsible for multiple physical and chemical processes that are directly affected by changes in temperature, an increase in temperature causes an increase in energy of molecular motion [59]. In the case of liquid evaporation the temperature is increased until the energy of the molecular motion approaches the energy of intermolecular interactions. The molecules can no longer be hold in place by the cohesive forces and the liquid transforms into a gas phase. A decrease in temperature can also stimulate a physical process such as crystallization. In this case, as the energy of the molecular motion drops, the state of the system becomes increasingly determined by the intermolecular interaction, which results in the formation of the crystalline struc-

[1] ASTM D792 at room temperature
[2] measured at cooling rate of 10 °C/min
[3] Specific heat at room temperature

ture.

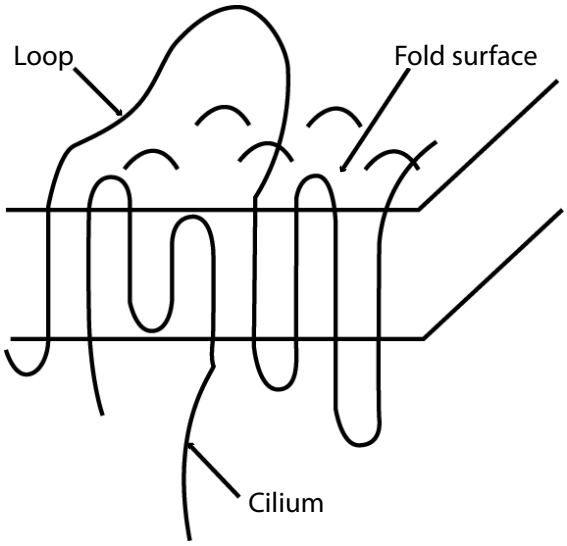

Figure 2.5: Crystalline model indicating surface fold as common re-entries, and irregularities given by cilium and loops. [58]

THERMODYNAMICS

Prior to any phase change within the material there must be a driving force. The crystallization process is generally accepted to be driven by the difference in Gibbs free energy between the lamellae of thickness l and the uncrystallized bulk polymer [60]. This driving force provides a relationship between physical parameters, such as temperature and thickness, which define a critical stable nucleus compared with the melt state. The Gibbs free energy of a crystal is usually composed of two components: 'bulk' and 'surface'. The former is the free energy of an infinite crystal without surfaces. The latter is an increase in free energy of the bulk due to the existence of the surface [61]. Gibbs concluded that the minimum thickness of a lamellae varies inversely with the supercooling ($\Delta T = T_m^0 - T_c$ where T_c is the crystallization temperature) according to,

$$l > \frac{2\sigma_e T_m^0}{\Delta[T_m^0]\Delta T} \tag{2.3}$$

where l is the thickness of the lamellae, T_m^0 is the equilibrium melting temperature, ΔH is the bulk enthalpy of melting process per unit volume, and σ_e is the surface free energy per unit area of the fold surface of a crystal. Fig. 2.6 illustrates the dependence of critical thickness of the lamellae on the temperature found from equation (2.3). T_m^0 is the condition when the two phases are in thermodynamic equilibrium. The free energy of melting becomes zero for pure polymers, when the system is under its equilibrium melting point, as given by

$$\Delta F_m = \Delta Q_m - T_m^0 \Delta S_m = 0 \tag{2.4}$$

Rewriting to find the equilibrium melting point

$$T_m^0 = \Delta Q_m / \Delta S_m \tag{2.5}$$

The equilibrium melting temperature is often described as the temperature at which an infinite crystal would melt[62].

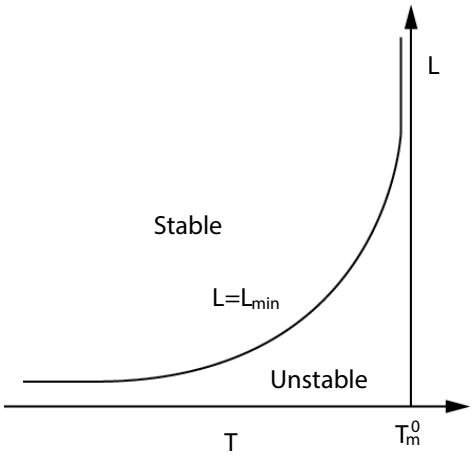

Figure 2.6: Dependences of minimal stable thickness of lamellae on amount of supercooling [58]

.

KINETIC THEORY

The final morphology of the polymer crystal is determined by the kinetic rather than equilibrium factors. In theory a polymer crystal would equilibrate given sufficient time; however, the chain nature of polymers hinders this process. The fast growing fronts will initially grow out until further growth of the crystal is bound by the slowest growing fronts. The kinetic theory assumes that the growth rate is dependent on the thickness of the lamellae and that of all possible lamellae thicknesses the preferred one is that which maximizes the growth rate.
As mentioned before, for any phase transformation there must be some driving force. This driving force is related to the supercooling. The greater the driving force the more the supercooled liquid wants to crystallize. The driving force of a crystal with specific thickness l will depend on that thickness. For $l < l_{min}$ the overall free energy increases and there is no driving force, but for $l > l_{min}$ the free energy decreases and there is a driving force. At the start the driving force increases rapidly as the bulk free energy increases compared with the effect of the surfaces. As the thickness increases the driving force flattens out due to the fact that surface energy and bulk energy start to cancel each other out. The opposing energy is the so called energy barrier that needs to be overcome by the driving force as illustrated in fig. 2.7, leading to the resultant growth rate.

NUCLEATION

The concept of entropic nucleation is based on an assumption that thermal fluctuations in an under cooled phase can overcome the nucleation barrier, induced by the surface energy of a small crystal. The probability that a nucleus of given size exists at a constant volume and energy is a function of the entropic change. This entropic change is

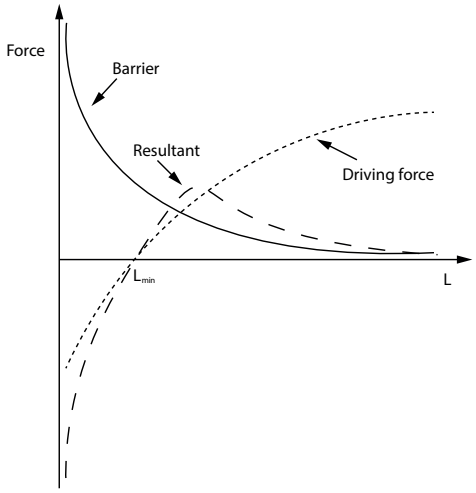

Figure 2.7: The resultant growth rate which is due to a driving force and barrier term. The overall growth rate is positive for $l > l_{min}$ but decreases to zero at large l, with maximum in between. [58]

based on the Boltzmann's law, which is proportional to $exp(\Delta S/k)$. At constant pressure and temperature, the probability that a nucleus of a given size exists is proportional to $exp(-\Delta G/(kT))$. Turnbull and Fisher [63] proposed a two opposing factor expression for the nucleation rate. The first factor is the critical free energy barrier proposed by Volmer and Weber [64]. The second is the diffusion energy barrier for molecules crossing over the liquid-solid interfaces proposed by Becker and Döring [65]. The nucleation rate is given as,

$$I = I_0 exp\left(-\frac{\Delta E + \Delta G^*}{kT}\right) \tag{2.6}$$

where ΔE is the activation energy related to the short-range diffusion of the liquid/ amorphous-solid boundary and I_0 is the prefactor. ΔG^* is the critical free energy barrier and is inversely proportional to the supercooling. At high temperatures the supercooling is low and there is a high free energy barrier, resulting in a small nucleation rate. At the opposite side of the temperature range the supercooling is high but there is a high activation barrier for polymer diffusion, resulting again in small nucleation rates. The result is a bell-shaped temperature-dependence curve between the glass transition and the melting temperature, as shown in Fig. 2.8. This behavior was first observed in the crystallization of unvulcanized rubber by Wood and Bekkedah [66] and is also observed in isothermal DSC tests for PEKK [67].
The formation of a nucleus implies the appearance of a surface, and the time that it takes the chains to configure into a surface is called the induction time, in which no crystals are present. Simultaneous experiments with wide and small angle x-ray diffraction (WAXS and SAXS), during the induction time of crystallization, indicate a ordering of parallel arrangement of chain segments as precursors for the crystallization process [68].

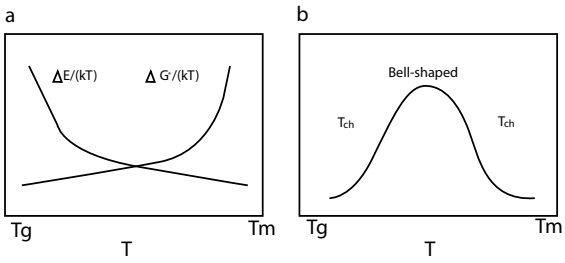

Figure 2.8: Schematic overview on the temperature dependence a) of the critical free energy and the activation barrier, and b) the typical bell-shape observed for polymer nucleation rates [58]

HOFFMAN-LAURITZEN THEORY

The crystallization process is the phase transformation of 3D random coil conformations to chain folded lamellar crystals. The challenges involved in experimentally monitoring individual chains during crystallization motivate the use of a mean field approach for the analytical theories [69], i.e. the individual trajectories are averaged. The first and widely applied analytical theory was formulated by Hoffman and Lauritzen (HL) [70]. They proposed the lateral growth rates to be controlled by surface nucleation. The crystal has an atomically smooth crystallographic surface which provides a growth front. One stem at a time the chain molecules deposit onto the surface of the crystal and start to crystallize onto the lattice. In the HL kinetic model, four parameters describe the nucleation process. 1) The surface-nucleation rate i, 2) the lateral covering rate (the growth rate parallel to the growth plane) g, 3) the width of the growth front L and 4) the growth rate perpendicular to the growth plane, G. The HL theory distinguishes three growth regimes as illustrated in fig. 2.9.

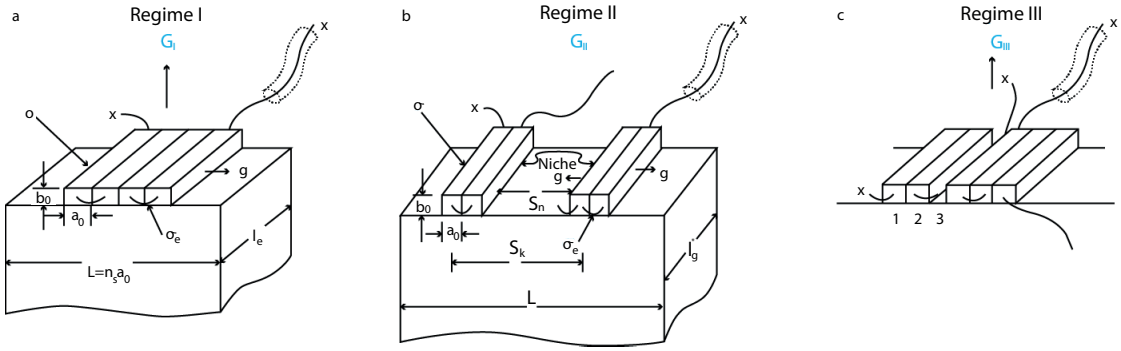

Figure 2.9: Schematic illustration of the three HL regimes on the temperature dependence a) Regime I b) Regime II c) Regime III [71]

Regime I

Regime I occurs at low super cooling, temperatures close to the melting temperature, see fig 2.9 a. The nucleus grows per layer and the growth of a single nucleus will proceed when the entire growth plane L is covered. It is possible to distinguish 3 steps within the process. The first is the nucleation on the atomically smooth growth front, followed

by a rapid addition of the stems (part of the polymer chains) up on the surface (lateral growth) to generate a new atomically smooth growth front. The final step, waiting for a thermal fluctuation to overcome the barrier and form a new nucleus (imperfection on the surface at which new stems can deposit), Which will lead to the new front. The growth rate in regime I is expressed by [72],

$$G_I = i b_0 L \tag{2.7}$$

where b_0 is the thickness of the stems crystallized on the substrate, and L is the substrate length which is covered by a layer of deposited chains on the surface under the condition that $g/L \ll iL$ [73]

Regime II
Increasing supercooling (larger difference between melting temperature and crystallization temperature) describes the physical picture of regime II growth, as in fig. 2.9b. On the growth plane of the substrate with width L there is the formation of multiple nuclei (Driving force to overcome the nucleation barrier is larger due to increased supercooling). Hence, the growth rates are now correlated with the parameters i and g. The rate determining factor for this regime is the separation between two neighboring nuclei. As the supercooling increases, the rate of nucleation increases and the separation between the nucleus continuously decreases. The analytical expression of the growth rate of regime II is independent of L [74],

$$G_{II} = (i b_0 g)^{1/2} \tag{2.8}$$

Regime III
Upon further cooling the lower crystallization temperature T_c at the end of regime II is surpassed and the crystal growth regime III starts as shown in fig 2.9c. The separation between two nuclei reaches the same order of magnitude as the stem width a_0. Hence the lateral covering rate g is not a governing factor and is no longer present in the expression for the growth rate. The expression takes the form of the expression for G_I:

$$G_{III} = i b_0 L' \tag{2.9}$$

where L' is the separation between two neighboring nucleus, which is shown to be around 1-3 stems widths [75]. The surface-nucleation rate i always yields the Turnbull and Fisher expression 2.6, while the linear growth rate G is described by an exponential relationship with the free energies of the nucleation barriers.

Hoffman and Lauritzen proposed that crystallization growth rate would be a mean-field approach, of the attachment, of one stem at a time onto the crystal growth front. Point [76] and Phillips [77] proposed two different depositing mechanisms for the stems. The former proposed a few segments (part of the stem) at a time [76], and the latter a few stems at a time [77]. The chosen approach may result in somewhat different values for the four parameters, but dependence of the growth rate G on the nucleation barrier is not altered. Of the four parameters only the linear growth rate G can be experimentally

measured. Over the years the original HL theory has undergone continuous improvements and modifications to account for new experimental findings and theoretical understandings [78–81]

2

The combination of depositing chain segments on the surface and the rate of advance of completed layers results in a growing rate as a product of a transport term with the driving force term:

$$G(M,T) = G_0(M) \cdot F_{transport}(T) \cdot F_{driving}(T) \tag{2.10}$$

where G_0 is a constant dependent on the molecular mass M, and F denotes a function that varies with T. The transport factor is the influence of the chain mobility on the formation of a chain onto the amorphous/crystal or melt/crystal interface.

$$F_{transport}(T) = \exp\left(\frac{-U^*}{R(T-T_\infty)}\right) \tag{2.11}$$

Where T_∞ is a reference temperature typically considered as 30 °C below the T_g, R is the gas constant and U^* is the apparent activation energy.
As discussed above, the decrease in surface free energy occurring by depositing a single strand onto the surface of a growing crystal acts as a driving force. The driving force is expressed as:

$$F_{driving}(l,T) = \exp\left(\frac{\Delta G(l)}{k_b T}\right) \tag{2.12}$$

where $\Delta G(l)$ is the free energy change upon addition of a strand of length l, and k_b is the Boltzmann constant. The transport factor increases as a function of the temperature, whereas the driving factor decreases with increasing temperature. Inserting the $F_{transport}$ and $F_{driving}$ into equation (2.12), one observes that for each crystallization temperature, there is a specific l which corresponds to the maximum growth rate. [82] Deviation of the l results in a sharp decrease of the growth rate and with increasing crystallization temperature to optimum l. To obtain the final version of the HL theory the ΔG is inserted in $F_{driving}$ and evaluated for l,

$$G(M,T) = G_0(M)\exp\left(\frac{-U^*}{R(T-T_\infty)}\right)\exp\left(\frac{-K_g}{R(T\Delta Tf)}\right) \tag{2.13}$$

where K_g contains the heat of fusion and the surface energy product $\sigma_e\sigma_s$ and ΔT is the undercooling. As $F_{driving}$ and $F_{transport}$ have opposed temperature dependence the typical bell shape is observed in the growth rate.

THE EFFECTS OF CARBON FIBRES ON THE CRYSTALLISATION OF PEKK

The effect of carbon fibers on the crystallization studies of PEAK polymers are mainly focused on PEEK. Lee and Porter [50] showed that increasing the fiber content resulted in a decrease in the necessary degree of undercooling. They suggested that the carbon fibers act as heterogeneous nucleation sites for PEEK crystallization, lowering the surface barrier for nucleation. However, the growth of PEEK spherulites can be hindered by

the presence of fibers, by restricting the space in which they have to grow and causing earlier impingement [83]. They found a lower degree of crystallinity for carbon fiber reinforced PEEK, compared to neat PEEK resin, due to the presence of the densely packed fibers counter acting the effect of many nucleation sites at the fiber surface. This relation between packing density of fibers and nucleating ability was further investigated by Waddon et al. [84] who varied the spacing between the fibers and there nucleation ability by sizing the fibers. They concluded that the crystal structure could be altered in terms of orientation and size of the spherulites. Desio et al. [85] investigated the effect of fiber content and fiber sizing on the crystallization kinetics. They found that sizings could enhance the chain mobility and thereby cancelling the surface effect of the fibers. Unsized fibers decrease the free surface energy for nucleation, which increases the nucleation rate.

The effect of carbon fibres on PEKK is significantly less explored. Hsiao et al. [86] investigated the isothermal crystallization kinetics of PEKK and its carbon fiber composites. They concluded that the presence of carbon fibers in the composites has little effect on the crystallization rate and the relative volume fraction. The possible reason for this is the rapid nucleating ability of PEKK. Choupin [67] et al performed the same research for neat PEKK and found an induction time three magnitude larger .

THE EFFECT OF CRYSTALLINITY ON THE PROPERTIES OF PEKK

Crystalline fractions in semi crystalline polymers restrict chain motion of the polymer chains. This restricted motion results in higher T_g and T_m of the polymers, as well as an increase in stiffness and strength. Arzak et al. [87] found a relation between PEEK's annealing time and its Young's modulus and yield stress. Both increased by annealing at higher temperature. The same effect was observed for the degree of crystallinity. The authors concluded that the increase in crystallinity resulted in an increase of the Young's modulus and yield strength.

The effect of crystallinity on PEKK is to the author's best knowledge not yet reported in the literature. Clear trends have been observed in other semi crystalline polymers poly (3-hydroxyalkanoate) PHA [88], Poly(lactic acid) PLA [89] and Polyethylene PE [90].

2.3. CRYSTALLIZATION AT THE WELD

External influences on the properties of the weld are well known[91], for example the differences of the wall thickness of the welded parts or the notches[91]. However, the influence of polymer morphology at the weld on the properties of the material are less well established. Wise [92] proposed the first theories predicting the welding strength, upon elevated temperature. The polymeric chains start to interdiffuse at the interface, and the strength is a result of macromolecular entanglement between both parts. De Gennes [93] proposed the theory of reptation that describes the motion of polymeric chains and was successful in predicting the molecular weight dependency on self-diffusion. From this starting point numerous attempts to link the process parameters to the interfacial strength in welding processes have been made. Wool's model [25] has been shown to fit the experimental data well, and it predicts the energy required to debond two welded

amorphous polymeric parts as a function of time, pressure, temperature and molecular weight. Since Wool's model comprises the basic assumptions for later models and predictions a short overview is provided next.

WOOL'S THEORY

The theory focuses on the weld strength as a result of a combination of surface rearrangement, wetting and diffusion. The basis is the reptation theory of De Gennes, which states that a chain is confined to a tube (the topological constraints imposed by its surroundings) and only the ends are free to move. The result is that the chain exhibits Brownian motion within the tube. As time passes the length of the chain $l(t)$, which moves freely without any notion of the initial tube and is called "escaped", increases. The distribution of escaped chains obeys a Gaussian distribution. This model is used to analyze the molecular motion of the chain at the interface and the emerged interdiffusion. Fig. 2.10 illustrates the interdiffusion; note that for clarity only one side of the interface is illustrated. In the beginning $l(t)$ is very small and the chains are still confined to their initial tube. As time passes the chains start to escape their initial tube and the chains at the interface start to migrate into the other polymeric side. As time continues, $l(t)$ increases as well as the interdiffusion. When approaching the relaxation time[4] the amount of interpenetration and reentanglement of chains seizes. At this state the molecular properties of the interface are the same as the bulk material in the initial state. Wool's theory predicts the number of chains intersecting the interface and the average interpenetration contour length. The model also links the fracture model of Dugdale [94] to the interdiffusion to predict the bond strength. However, similarly to other theories, Wool does not take into account the role of crystallization kinetics and the role of crystallinity on self-diffusion when predicting the interfacial strength.

COCRYSTALLIZATION

In contrast to welding of amorphous polymers, semicrystalline polymers have considerable plastic deformation which usually limits the use of linear fracture mechanics and the Dugdale model. Furthermore, abnormal diffusion behavior can arise upon melting of semicrystalline polymers [95]. The morphology of crystalline regions also differs from the one in amorphous regions, so the interdiffusion behaviour of the chains into the crystals is unlikely to be the same. Based on these considerations, Bonten and Schmachtenberg [96] proposed the "Nexus-hypothesis" for bonding of semicrystalline polymers. They proposed a joint recrystallization of the molecular chains of both components in the weld: cocrystallization. The nexus provides the link between crystalline regions such that a lower nexus leads to an earlier failure of the links, resulting in a weaker welding bond. Fig. 2.11 illustrates that a third interlamellar layer carries the most load per link and will fail first.

[4] Time at which the complete or most of chains is escaped out of the initial tube. There is no relation any more between the starting configuration and it's new shape

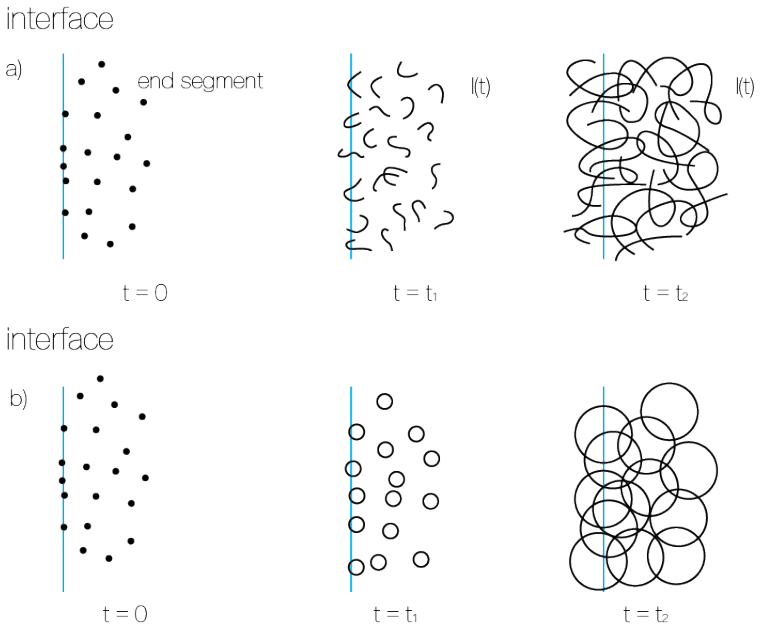

Figure 2.10: Schematic overview of the wool theory on interdiffusion of two amorphous polymeric materials at the weld (only one half and deviation off original orientation is shown). With passing of time the chain ends diffuse over larger distance from their original position. Chains located at the edge diffuse over the interface possibly entangle with chains of the adjacent part . a) illustrated as chain ends escaping their initial tube, b) illustrated as expended range of motion of chain ends. [25]

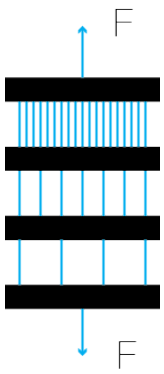

Figure 2.11: Illustration of the interlamellar links and their load transferring ability [96]

Bonten tested welded PET at different states of crystallization. They found a force transmission [97] of 80 MPa for long annealed semicrystalline PET, 60 MPa for amorphous PET and 70 MPa for the welded specimen indicating that upon welding a crystalline inter region formed at the interface as confirmed by DSC tests [96].

2.4. ANALYTICAL MODELING

More knowledge and know-how about the crystallization during induction welding can facilitate its widespread use in industrial and academic applications since this process is

environmentally-friendly, fast, reliable and does not involve contact [98].

Measuring and predicting the temperatures involved during the induction welding has significant importance: 1) checking that the temperature reached is high enough to allow self-diffusion and obtain sufficient interfacial strength; 2) locating the heat affected zone (HAZ) and the possible morphological changes of the material in this region[5]; and 3) checking if the temperature does not exceed the thermal degradation temperature. The present studies of induction welding process lack conclusive links between process parameters, crystallinity and their effect on assemblies.

AVRAMI MODEL

To model the evolution of crystal fraction, the Avrami model is frequently used [99]. The equation determining overall crystallization kinetics rate is written as:

$$\alpha = 1 - \exp(-Kt^n) \tag{2.14}$$

where n is the Avrami exponent and K is the crystallization rate constant. The Avrami exponent is claimed to give insight about the mechanism of nucleation and the dimensionality of spherulite growth [100]. Banks and Sharples [101] concluded that the Avrami exponent is not automatically conclusive about the crystallization mechanisms. One should note that the Avrami equation was developed for the crystallization of metals. Although the equation fits the data well [102], physical basis of polymers crystallization is very different due to their long, flexible and entangled chains.

Therefore, limited conclusions can be drawn from equation (2.14). Note that metals are able to crystallize completely, transforming from a completely amorphous phase ($\alpha = 0$) to a completely crystalline phase ($\alpha = 1$). Crystallized polymers do not fully crystallize (α is smaller than 1) due to the nature of the chain structure. In order to adapt to this observation, the physical meaning of $\alpha = 1$ is reinterpreted as the maximum extent of crystallinity that can be reached by the polymer. So the Avrami equation is "a convenient representation of experimental data" rather than a way of obtaining physical insight [103].

However comparing Avrami parameters for different polymers can provide insight into the crystallization kinetic difference between these polymers . For example the plot of $ln(-ln(1-\frac{X_{vc}}{X_{vc\infty}})$ as a function of $ln(t)$ should result in a linear trend; thus, deviation of these lines suggests a more complex crystallization process. Where X_{vc} is the degree of crystallinity at that moment and $X_{vc\infty}$ is maximum degree of crystallinity, which is described later as the relative extent of conversion α ($\alpha = \frac{X_{vc}}{X_{vc\infty}}$). As mentioned in section 2.1 PEKK is known to show secondary crystallization and two stage Avrami models are suggested to better model the behaviour, as explained in the next section.

TWO STAGE CRYSTALLIZATION

As mentioned, plotting the $ln(-ln(1-\alpha))$ as a function of $ln(t)$ should result in a linear plot. Deviation of this linear behaviour indicates a secondary crystallization, as found by

[5]The degree of crystallinity is related to the mechanical properties of semi crystalline polymers.

Gardner et al. [48] for PEKK. The Avrami crystallization plots for 60/40 PEKK constructed by Choupin et al. [67] shows a deviation of the linear behaviour suspected at 60% of the crystallization which correspondents to a deviation from the dashed line close to zero as seen in fig. 2.12, suggesting a second crystallization mechanism. The isothermal DSC data for PEKK imply that a suitable model should involve two nucleation and growth processes [34, 67, 86].

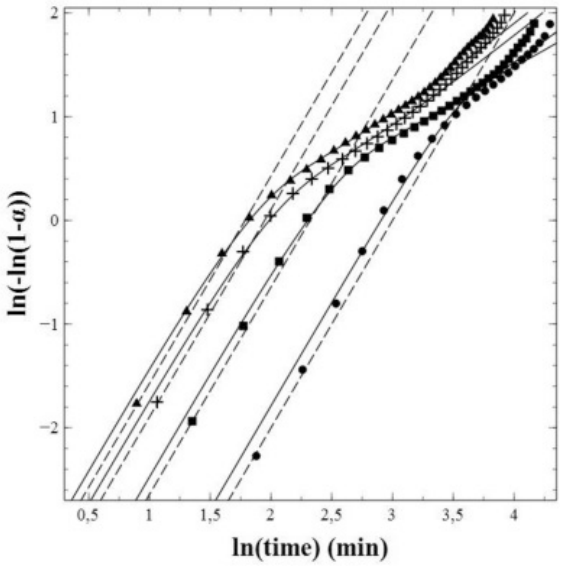

Figure 2.12: Avrami crystallization plots for the isothermal crystallization of neat PEKK at 200 °C, 210 °C, 220 °C, 230 °C isothermal crystallization from the melt [67]

Two different models to account for the secondary crystallization were proposed: Velisaris and Seferis [34] proposed a parallel crystallization process, whereas Hillier [104] assumes a primary crystallization process followed by the secondary crystallization process initiating from the primary crystals. Taking into consideration the observations by Gardner et al. [48], there is evidence pointing towards a secondary recrystallization at the end of the crystallization during DSC and SAXS. These observations are the basis for the Hillier model, and the physical basis of two crystallization process is applied in the Hillier model.

Hillier model

The Hillier model [104] is based on a two stage Avrami kinetics, where the first stage is the nucleation and growth of the spherulites from the initial time 0 until time t when the total crystallinity developed in the primary process is reached, α_{cp_∞}. The primary nucleation obeys equation:

$$\alpha_{pc}(t) = 1 - \exp(-K_{pc} t^{n_{pc}}) \tag{2.15}$$

where $\alpha_{pc}(t)$ is the relative crystallinity, K_{pc} is the primary crystallization rate constant, and n_{pc} is the primary Avrami exponent.

The secondary crystallization process starts at time θ and is expressed as:

$$\alpha_{sc}(t) = \int_0^t \alpha_{pc}(\theta) \times \frac{d}{dt}(\alpha_{sc}(t-\theta))d\theta \tag{2.16}$$

where $\alpha_{sc}(t-\theta)$ is the relative crystallinity of the secondary process at time t, K_sc and n_{sc} are the growth constant and Avrami exponent for the secondary crystallization. The volume factor for the primary and secondary crystallizations are,

$$1 = w_{pc} + w_{sc} \tag{2.17}$$

the total crystallization is expressed as,

$$\alpha(t) = w_{pc}\alpha_{pc}(t) + w_{sc}\alpha_{sc}(t) \tag{2.18}$$

and substituting equation (2.15) and (2.16) into equation (2.18) results in:

$$\begin{gathered}\alpha(t) = w_{pc}[1-\exp(-K_{pc}t^{n_{pc}}] + w_{sc}K_{sc}n_{sc} \\ \int_0^t [1-\exp(-K_{pc}\theta^{n_{pc}}) \times (t-\theta)^{n_{sc}-1}\exp[-K_{sc}(t-\theta)^{n_{sc}}]]d\theta\end{gathered} \tag{2.19}$$

When $\theta = 0$, equation (2.19) simplifies to:

$$\alpha(t) = w_{pc}[1-\exp(-K_{pc}t^{n_{pc}}] + w_{sc}[1-\exp(-K_{sc}t^{n_{sc}}] \tag{2.20}$$

This equation clearly shows that values for the weight factors provide insight into the importance of both crystallization processes.

Choupin model

Choupin et al. [67] proposed a model extending the Hillier model to predict the crystallization evolution for different processing cycles of PEKK (60/40). Conducting different isothermal experiments for melt and glass crystallization, they plotted $ln(-ln(1-\frac{X_{vc}}{X_{vc\infty}}))$ as a function of $ln(t)$ to obtain data as shown in fig. 2.12. A good fit is observed for the straight line for crystallinity below $\alpha = 0.6$ with slope given by n_{pc}. The bending in the curve seen above $\alpha = 0.6$ is associated with the secondary crystallization and the respective slope n_{sc} is found by multi linear regression fitting of the Hillier model. The K_{pc} and K_{sc} found by fitting are expressed as a function of the initial number of potential nuclei and the crystal growth rate, where the expression differs for the observed dimensional crystallization. Choupin et al. [67] observed a two dimensional growth and instantaneous nucleation for the primary crystallization, while they observed one dimensional growth and instantaneous nucleation for the secondary crystallization. The related expression:

$$K_{pc} = \pi N_{0pc} G_{pc}^2 \tag{2.21}$$

$$K_{sc} = N_{0sc} G_{sc} \tag{2.22}$$

where N is the initial number of potential nuclei and G is the growth rate. Expressing the growth rate as the HL theory given in equation (2.13), the primary crystallization rate is written as:

$$K_{pc}(T) = K_{0pc}(M)\exp\left(\frac{-2U^*}{R(T-T_\infty)}\right)\exp\left(\frac{-2K_{gpc}}{(T\Delta Tf)}\right) \tag{2.23}$$

and the secondary crystallization rate is written as:

$$K_{sc}(T) = K_{0sc}(M)\exp\left(\frac{-U^*}{R(T-T_\infty)}\right)\exp\left(\frac{-K_{gsc}}{(T\Delta Tf)}\right) \tag{2.24}$$

where U^* is the universal value and the pre-exponential factors $K_{0pc} = \pi N_{0pc} G_{0pc}^2$ and $K_{0sc} = N_{0sc} G_{0sc}$ are independent of temperature. $\Delta T = T_m^0 - T$ and $f = \frac{2T}{T+T_m^0}$ are abbreviations to increase clarity of the HL equation

Plotting the K_{pc} and K_{sc} values of the Hillier model and fitting equation (2.23) and equation (2.24) the typical bell shape of the HL theory is obtained as seen in fig. 2.13.

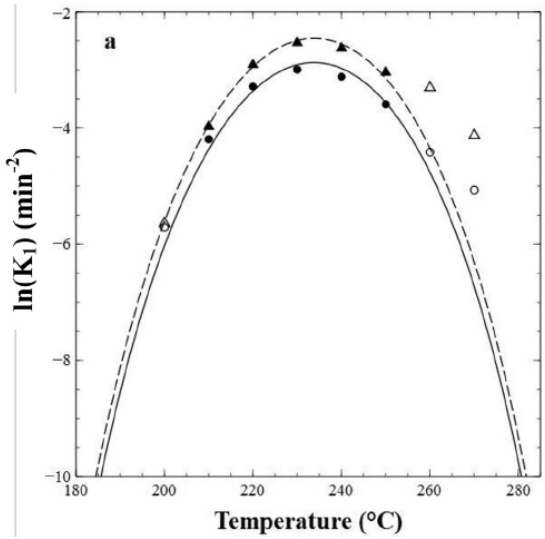

Figure 2.13: Plot of the primary crystallization rate constant versus time for melt (circles) and glass (triangles) crystallization, fitted with equation (2.23). The unfilled markers where excluded from the fitting [67].

To include the time before nucleation the induction times measured with the DSC test are plotted as time versus temperature. Figure 2.14 illustrates the results of the DSC experiment, The results match the adopted Turnbell and Fisher equation 2.6 for nucleation [63]:

$$t_i(T) = K_{t0}\exp\left(\frac{E_{t2}}{R(T-T_g)}\right)\exp\left(\frac{E_{t1}}{R(T_m^0-T)}\right) \tag{2.25}$$

where E_{t1} and E_{t2} are the activation energies for melt and glass nucleation.
Including the induction time in the Hillier model with the K_{pc} and K_{sc} found by fitting the HL equations, Hillier constructed time-temperature-transformation (TTT) diagrams to allow the prediction of any isothermal crystallization process. Figure 2.14 shows the

TTT diagram, the fastest crystallization kinetics is at 230 °C where 80% of the relative crystallization is reached within 15 minutes and where it takes up to 60 minutes to reach a 99.9% degree of conversion.

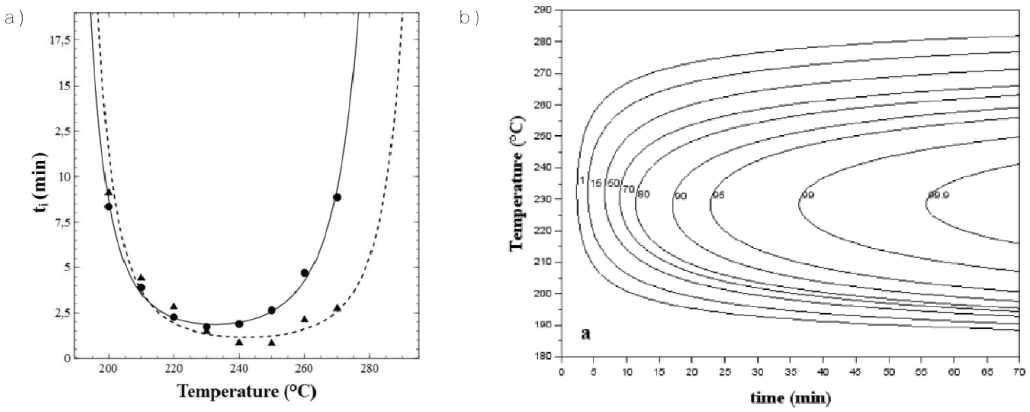

Figure 2.14: a) Plot of the induction time with equation (2.25) fitted, and b) TTT diagram of PEKK (60/40) [67].

In summary, Choupin et al. [67] found a new method to gain useful information and insight about the crystallization behaviour of PEKK for isothermal conditions. They excluded the high and low temperatures from the fitting of the HL equations because the slow crystallization rates at these temperatures gave underestimations of the enthalpy by the DSC tests. This makes their predictions in these temperature regions less reliable. To conduct a test at isothermal conditions, the specimen needs to be cooled from the equilibrium melting temperature to the isothermal temperature. At the moment the cooling changes to a constant isothermal temperature the DSC needs some time to stabilize. Within this time it is hard to establish the difference between the energy change from the specimen and the energy from the change in program, masking the onset of crystallization. For polymers with fast crystallization rate and small induction times conducting isothermal measurements with high precision can be a challenge [105]. The cooling at the weld will follow a descending rate and will differ form the isothermal behaviour modelled by these authors [67].

2.4.1. ISOCONVERSIONAL METHODOLOGY

Isoconversional methodology discusses the kinetics of thermally stimulated processes. Mapping the rate of processes, isoconversional methods aim to parametrize the process rate. Enabling prediction of the conversion rate for any combination of given variables. This methodology then obtains insight into the process mechanisms, which is useful in the gelation of a solution or the crystallization of a melt. The basis for isoconversional methodology is the equation in which the rate is parametrize as a function of T and the extent of conversion α:

$$\frac{d\alpha}{dt} = k(T)f(\alpha) \tag{2.26}$$

where t is time, $f(\alpha)$ is the reaction and $k(T)$ is the rate constant. The rate constant is

often characterized by the Arrhenius equation:

$$k(T) = A\exp\left(\frac{-E}{RT}\right) \tag{2.27}$$

where A is the preexponential factor, E and R are the activation energy and gas constant. Isoconversional kinetics are based on the principle that one is allowed to eliminate the reaction model from the kinetic rate equation (2.26). In other words, it is based on the principle that the process rate is only a function of T at constant extent of conversion α. This is derived by taking the log of equation (2.26) at constant α:

$$\left[\frac{\partial ln(d\alpha/dt)}{\partial T^{-1}}\right]_\alpha = \left[\frac{\partial ln(k(T))}{\partial T^{-1}}\right]_\alpha + \left[\frac{\partial ln(f(\alpha))}{\partial T^{-1}}\right]_\alpha \tag{2.28}$$

Subscript α indicates the constant related to the extent of conversion. If α is a constant, the second term on the right-hand side becomes zero. Substituting the Arrhenius equation (2.27) into the first term on the right hand side one derives:

$$\left[\frac{\partial ln(d\alpha/dt)}{\partial T^{-1}}\right]_\alpha = \frac{E_\alpha}{R} \tag{2.29}$$

Equation (2.29) allows the identification of the activation energy without determining the form of the reaction model, $f(\alpha)$. Although the reaction model is not identified explicitly, some form of $f(\alpha)$ is still assumed to define the conversion dependence of the process rate.

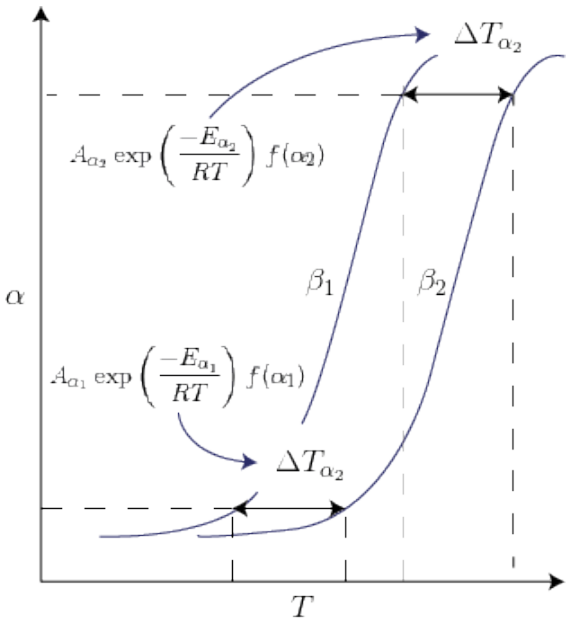

Figure 2.15: principle of the isoconversional method. [106]

By conducting several runs at different temperature programs, the temperature dependence of the isoconversional rate can be obtained. For instance conducting non isothermal runs at two different heating rates, β_1 and β_2. Using DSC data shown in figure 2.15

and selecting a certain conversion α, the temperature related to the conversion of each heating run is identified, respectively $\Delta T_{\alpha 1}$ and $\Delta T_{\alpha 2}$. The slope of the α versus T curve at T_α can be converted to the conversion rate:

$$\left(\frac{d\alpha}{dt}\right)_\alpha = \left(\frac{d\alpha}{dT}\right)_\alpha \beta. \tag{2.30}$$

Once the isoconversional rate of several temperature programs is determined, the parameters are obtainable through a combination of Arrhenius equation and equation (2.26):

$$\ln\left(\frac{d\alpha}{dt}\right)_{\alpha,i} = \ln[A_\alpha f(\alpha)] - \frac{E_\alpha}{RT_{a,i}} \tag{2.31}$$

where i indicates the temperature program. A plot of the left-hand side versus the reciprocal temperature obtains a straight line, from which the slope gives the activation energy E_α, without identifying or assuming any reaction model. The preexponent and reaction model, A_α and $f(\alpha)$ can be deduced from the intercept. The techniques to encrypt the A_α and $f(\alpha)$ are discussed in section 2.4.1. To find the activation energy of each α equation (2.31) is evaluated. The basis for predicting kinetic behavior by isoconversional methods is the assumption that for any given α, $g(\alpha)$ remains the same when changing the temperature program, for example the heating rate. Where $g(\alpha)$ function describing the form of conversion. The integral expression that gives $g(\alpha)$ is written as [107].

$$g(\alpha) \equiv \int_0^\alpha \frac{d\alpha}{f(\alpha)} = A\exp\left(\frac{-E}{RT}\right)t \tag{2.32}$$

The statement that all $g(a)$ are the same for different thermal heating rates allows to write the following equality:

$$\begin{aligned} g(\alpha) = \frac{A_\alpha}{\beta_1}\exp\left(\frac{-E_\alpha}{RT_{\alpha,1}}\right)t = \\ \frac{A_\alpha}{\beta_2}\exp\left(\frac{-E_\alpha}{RT_{\alpha,2}}\right)t = \ldots \\ = \frac{A_\alpha}{\beta_n}\exp\left(\frac{-E_\alpha}{RT_{\alpha,n}}\right)t \end{aligned} \tag{2.33}$$

When T_α is measured without any error and the equality holds strictly, equation (2.33) becomes:

$$\sum_{i=1}^{n}\sum_{j\neq i}^{n}\frac{\beta_j \exp\left(\frac{-E_\alpha}{RT_{\alpha,i}}\right)t}{\beta_i \exp\left(\frac{-E_\alpha}{RT_{\alpha,j}}\right)t} = n(n-1) \tag{2.34}$$

Measuring T_α without any error is challenging, so an approximation of the equality expressed in equation (2.34) is reached by minimizing the difference between the left- and right-hand sides. This minimum corresponds to the minimization of the left-hand side only, and the activation energy is then given by minimizing the following equation:

$$\Phi(E_\alpha) = \sum_{i=1}^{n}\sum_{j\neq i}^{n}\frac{\beta_j \exp\left(\frac{-E_\alpha}{RT_{\alpha,i}}\right)t}{\beta_i \exp\left(\frac{-E_\alpha}{RT_{\alpha,j}}\right)t} \tag{2.35}$$

The minimization procedure is repeated for each extent of conversion to produce the dependence of E_α on α.

ISOCONVERSIONAL METHODOLOGY FOR CRYSTALLIZATION OF POLYMERS

Measuring the enthalpy change by DSC is the first step in the isoconversional method, with the goal of parameterizing the kinetic behavior of crystallization of polymers. The relative crystallization is found by:

$$\alpha = \frac{\Delta H(t)}{\Delta H_\infty} \tag{2.36}$$

where $H(t)$ is the heat of fusion, measured as the area between the peak and the baseline at time t and ΔH_∞ is the total area between the peak and the baseline . The kinetics of the conversion is commonly described in terms of the Avrami equation [99]:

$$\alpha = 1 - \exp[-kt^n] \tag{2.37}$$

where t is the time, n is the Avrami exponent and k is the growth rate.
Isoconversional methods for crystallization use the widely accepted kinetic theory of HL and equation (2.13) for growth rate, where typically U^* is the universal value of 6.3 kJ mol^{-1} [108]. By converting equation (2.13) to,

$$\ln G + \frac{U^*}{R(T - T_\infty)} = \ln G_0 - \frac{K_g}{T\Delta T f} \tag{2.38}$$

where $f = (2 \cdot T)/(T + T_m)$ is the chain diffusion energy, K_g is determined from the linear expression on the left hand side versus $(T\Delta T f)^{-1}$, this relates the conversion rate to one single variable. Hoffman [108] showed that equation (2.13) with the constant values of U^* and K_g provides a good fit between a range of supercooling as wide as 40-100 °C.
Hoffman et al. [108] rely on equation (2.13) on the spherulite growth rate measured by polarized light microscopy. For composites containing medium to high volume fractions carbon fibers this is proven to be difficult because the fibers are black and mask the growth. However the DSC is capable of measuring the overall growth rate of crystallization. The heat flow measured by the DSC is linked to the growth rate by,

$$\Phi = \Delta h S G \tag{2.39}$$

where Φ is the overall growth rate, Δh is the volumetric heat of crystallization and S is the total area of the growth surface. Because it is not possible to determine the S in the DSC, Toda et al. [109] established that S can be excluded when determining the logarithmic derivative of the heat flow:

$$\frac{d\ln\Phi}{dT^{-1}} = \frac{d\ln G}{dT^{-1}} \tag{2.40}$$

Toda et al. confirmed their findings by using DSC and microscopy experiments to measure the left- and right-hand side of equation (2.40). Multiplying both sides by $-R$, equation (2.40) becomes:

$$-R\frac{d\ln\Phi}{dT^{-1}} = -R\frac{d\ln G}{dT^{-1}} \tag{2.41}$$

If the derivative of Φ is expressed at a constant extent of conversion, it would yield an isoconversional value of E_a:

$$E_a = -R\frac{d\ln G}{dT^{-1}} \tag{2.42}$$

Vyazovkin et al. [110] substituted G from equation (2.13) into equation (2.42) and took the derivative to obtain the equation:

$$E_\alpha = U^*\frac{T^2}{(T-T_\infty)} + K_g R\frac{T_m^2 - T^2 - T_m T}{(T_m - T)^2 T} \tag{2.43}$$

This equation relates the effective activation energy derived by the model-free approach [111] on basis of DSC experiments to the theoretical dependence of the U^* and K_g parameter of the HL theory. U^* and K_g can be related to the experimental data obtained by DSC. The overall dependence of the temperature on the right-hand side of equation (2.43) suggests that the second term becomes negative between $0.618T_m$ and T_m. Approaching melting temperature the term quickly increases, resulting in large negative values for the activation energy of melt crystallization at small supercooling. This equation also implies low conversion rates at small supercooling temperatures. If the temperature is decreased from T_m, the effective energy should increase towards zero. Note that the first term is always positive and increases as the temperature approaches equilibrium melting temperature. Increasing the temperature from limited chain motion (T_∞), the effective activation energy should decrease towards zero. This implies that the energy barriers for nucleation and diffusion are large close the T_m and T_g resulting in small growth rates. At the T_{max} the two activation energies combined are the lowest resulting in the largest growth rate. Figure 2.16 illustrates the overall temperature dependence of the effective activation energy.

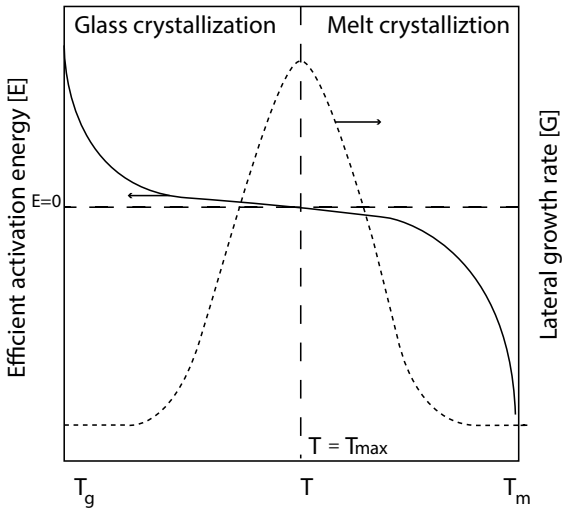

Figure 2.16: Overall temperature dependence on the effective activation energy [110]

ISOCONVERSION METHOD WITH DEPENDENCE ON TEMPERATURE

Selecting an appropriate isoconversional method to determine the activation energy for the analysis of the polymer crystallization data is crucial. The preferred methods are the

differential method by Friedman [112] or the flexible integral method as proposed by Vyazovkin [106]. An other interesting method is the method developed by Ortega [113] which is popular due to its simplicity. Ortega and Vyazovkin methods are applicable for both cooling and heating programs [114]. With these methods the DSC data for several heating programs can be analysed to obtain the dependence of the activation energy on the extent of conversion. Since the relative extent of crystallinity is measured at different rates, increasing α represents increasing temperatures for glass crystallization and decreasing temperatures for melt crystallization, in agreement with Fig. 2.16. For example the dependency of crystallization of Poly(ethylene 2,5-furandicarboxylate) (PEF) [115] seen in Fig. 2.17 is in good agreement with the earlier discussed activation energies for melt- and glass crystallization, shown in Fig. 2.16. The activation energy for the glass crystallization is positive and negative for melt crystallization and both tend to zero as the extent of crystallization gets to $\alpha = 1$.

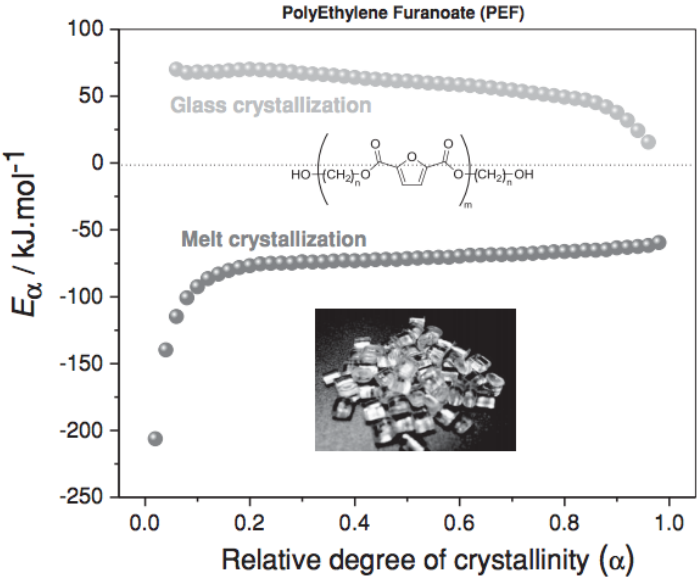

Figure 2.17: The activation energy for melt- and glass crystallization for PEF [115]

One needs to convert the obtained activation energy from the dependence on α to a dependence on temperature, to parametrize the isoconversional activation energies in terms of the HL theory. Considering that different heating (or cooling) rates reach a given value α at different temperatures, the set of temperatures that lead to a certain value of α is replaced with a single mean temperature. Replacing all the α with the representative mean temperature, one obtains a dependence of E_α on T. For melt crystallization the E_α are expected to be negative at temperatures above T_{max}. For example the T_{max} of PET is experimentally found to be in the region 443-475 K [116]. Fig. 2.18 illustrates the expected behaviour of the E_α versus temperature dependence, and demonstrates a remarkable breaking point at 475K, which is associated with a change in crystallization mechanism. This change in crystallization mechanism may be the change of HL regime as described in section 2.2. The breakpoint indicates the change of regime I into regime II, and the theory predicts a theoretical ratio of 2 or more for regime II compared to

regime I [75]. Vyazovkin and Sbirrazzuoli [116] found an increase of 1.7 for the change in regime I to regime II for PET. The fitting of K_g can be done by setting U^* to the universal value, but Hoffman et al. [108] fitted both the K_g and U^* values for a range of different polymers and found best fits for values of U^* varying between 4 and 17 kJ mol^{-1}. As the value for U^* increases, the resulting value for K_g increases. Therefore it is advised to fit both K_g and U^* to obtain more reliable estimates of these values. Bosq et al. [117] parametrized the crystallization of polytetrafluoroethylene over a wide range of heating and cooling rates and found that it is possible to fit both melt and glass crystallization kinetics with one set of K_g and U^* values. As cold crystallization is happening in the region closer to the T_∞ it is associated with the diffusion of chains K_g. Incorporating cold crystallization in the parametrization should increase the accuracy of both nucleation barriers U^* and K_g, because cold crystallization contains mostly information chain diffusion and melt crystallization contains mostly information about nucleation. The ability to fit both glass and melt crystallization with one single set of HL parameters is also found in other experiments [115, 117].

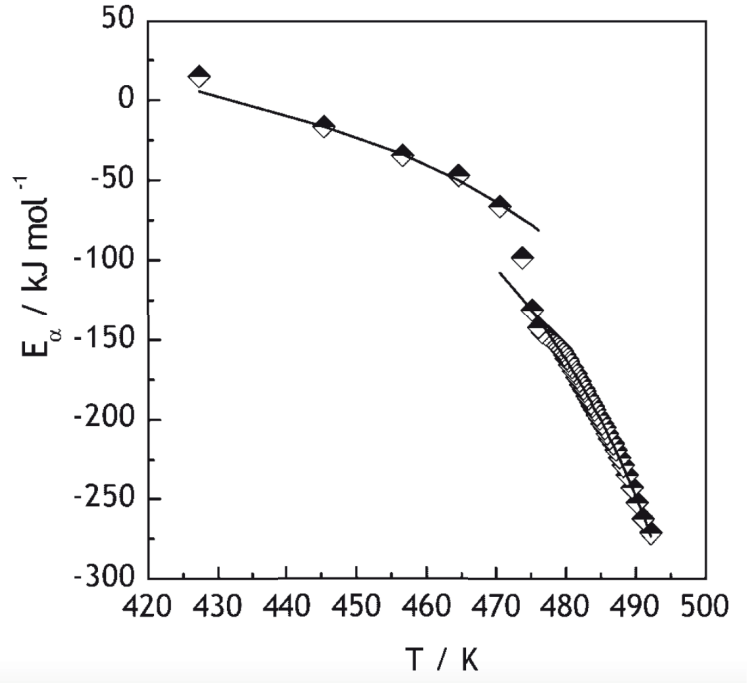

Figure 2.18: The activation energy for melt crystallization for PET [116]

ISOCONVERSION METHOD WITH DEPENDENCE ON EXTEND OF CONVERSION

Farjas et al. [118] argue that the proposed method by Vyazovkin and Sbirrazzuoli [116] assumes that the kinetic constants (U^* and K_g) are independent of α, as they convert to a mean temperature to obtain a temperature dependence. Therefore, the ability to give a full description of non-ideal processes is lost and predictions of the crystallization behaviour are not possible. In order to circumvent this, they proposed a method that includes a dependence on α but without requiring an Arrhenian dependence on the temperature for the reaction rate as illustrated in fig. 2.16.

The referred authors fully describe the crystallization kinetics with the parameters U^*, K_g and $k_0 g(\alpha)$, where all the parameter vary with the extent of conversion. The basic equation for isoconversion (2.26) is written as:

$$\frac{d\alpha}{dt}(t,T) = k(T) f(\alpha(t,T)) \tag{2.44}$$

to account for temperature trajectories.
For different heating and cooling rates, β_i, a specific value of α is reached for a different temperature and time. Every thermal history $\frac{d\alpha}{dt}(t_i, T_i)$ obeys the HL theory, as in equation (2.13), is now converted to account for the dependence of α.

$$\frac{d\alpha}{dt}(t_i, T_i) = k_{0\alpha} g(\alpha) \exp\left(\frac{-U^*_\alpha}{R * (T_i - T_\infty)}\right) \exp\left(\frac{-Kg_\alpha}{T_i \Delta T_i f_i}\right) \tag{2.45}$$

The result is a system of non-linear equations on U^*_α, Kg_α and $k_{0\alpha} g(\alpha)$, because of the dependence between U^*_α and Kg_α described by equation (2.43). The unknowns can be derived after a sequence of linear fittings described hereafter.

As discussed previously, in the low temperature region close to T_∞ corresponding to the glass crystallization the α_i is mainly governed by Kg_α. For the case of melt crystallization, i.e. for temperatures close to T^0_m, the process is governed by U^*_α as illustrated in fig. 2.16. The iteration procedure starts with guessing a realistic value for U^*_α, the universal value of 6,3 kJ is a good starting point. Linearizing the equation (2.45) with the guessed value of U^*_α:

$$\ln\left(\frac{d\alpha}{dt}(t_i, T_i)\right) + \frac{U^*}{T_i - T_\infty} = \ln[k_{0\alpha} g(\alpha)] - \frac{Kg_\alpha}{T_i \Delta T_i f_i} \tag{2.46}$$

The slope of the line between the point, determined by $Y_i = ln(-\dot{\alpha_i}) + \frac{U^*_\alpha}{T_i - T_\infty}$ versus $X_i = \frac{1}{T_\Delta T_i f_i}$ (U-plot) determines Kg_α and $k_{0\alpha} g(\alpha)$ is the intersect. Since U^*_α often deviates from the guessed value of U^*_α, the experimental points will not be well aligned and a secondary plot is constructed with the points $Y_i = ln(-\dot{\alpha_i}) + \frac{Kg_\alpha}{T_i - T_\infty}$ versus $X_i = \frac{1}{T_i - T_\infty}$ (Kg-plot). The slope of these points is the new U^*_α. Repeating this procedure and with updated U^*_α and Kg_α improves the general fit and increases precision of U^*_α and Kg_α. Figure 6.2 illustrates the procedure to find the kinetic parameters.

This alternative fitting assumes a similar "weight" of the glass and melt crystallization in the final U^*_α and Kg_α values. Experiments need to cover the temperature ranges where either U^*_α and Kg_α dominate. Farjas et al. [118] tested the method for the crystallization of PET, that shows a similar secondary crystallization as PEKK [119]. The predictions converted to the same peak temperature as those measured by DSC experiments, and the deviation for the experiments is claimed to mainly arise from experimental limitations (Changing the heating of cooling rate in experiments, results in noise in the DSC peaks. The method is able to predict complex crystallization behavior with different thermal trajectories).

2.4.2. CONCLUSION LITERATURE STUDY

PEKK is a slowly crystallizing material compared to other polymers, the added flexibility in the backbone of the polymer chain reduces the crystallization rate. The degree of crystallinity in a semi crystalline polymer is determine only by it's thermal history. However there are multiple process parameters which influence the cooling behaviour of laminates during the induction welding process. Determining the optimal process window to reach an efficient degree of crystallinity is a novel way to determine processing conditions. A cost-effective manner to predict the process window based on the process conditions is the use of finite element analyses (FEA). As detailed in chapter 5,where FEA is used to predict the heat generation in induction welding of UD tapes.

2.5. RESEARCH QUESTION AND OBJECTIVES

Based on the conclusions of the literature review and wishes of the company, knowledge gaps were identified in the influence of crystallinity on the quality of the weld and on the understanding of the effect of processing on the final crystallinity of the material. this way the objective of the research is to fill the knowledge gap of the effect of process parameters on the crystallinity in the case of UD CF/PEKK induction welded composites. This is done by characterizing the crystallization kinetics of CF/PEKK, analytically modelling the developed crystallinity and link the crystallinity to the cooling trajectory predicted by the computational model. This is summarized on the following research question.

"Can we predict crystallinity based on the process parameters?"

To answer the main research question, we divide it into two sub-topics and sub-research questions.

1. Can the crystallization of CF/PEKK be predicted?
    - What is the crystallization kinetic response of the material when subjected to changing thermal trajectories.
    - What are the parameters influencing crystallization?
    - How can the crystallization kinetics be parameterised?
2. Is it possible to find the effect of processing parameters on the crystallinity by computational simulations?
    - What are the different process parameters with effect on the crystallinity and what are the input parameters?
    - Is it possible to accurately model the cooling rate for different combinations of process parameters?
    - Can the model predict crystallinity at the weld interface?
    - Can the computational model be validated?

2.5.1. METHODOLOGY

To answer the main research question,chapter 3 presents the crystallization experiments performed on the CF/PEKK composites with different heating trajectories. The crystallization response of the CF/PEKK to different thermal trajectories is recorded with the help of differential scanning calorimetry. The results should clarify how the material responds to different heating and cooling trajectories,and are expected to show the rate of crystallization based on cooling and heating rate. in addition the electrical and thermal properties of the CF/PEKK will be measured in the three principal directions to account for the highly anisotropic properties of UD CF/PEKK. Since they dictate the paths available for the currents and heat flow in the material.

A computational model is also developed in chapter 5that can model the different thermal behaviour for different processing parameters in induction welding. Validation is obtained by analysing crystallisation experiments and comparing them to the results produced by the computational model. The goal is to be able to predict crystallinity with the model, so that the induction welding process, can be subsequently optimized.

2.5.2. READERS GUIDE

The report will provide a clear outline of all the experimental set-ups and production procedure of the laminates used in chapter 3.The first sub-research question will be addressed in Chapter 4, where we will parametrize the crystallization kinetics. Chapter 5 describes the computational model in Ansys and characterizes the influence of the processing parameters on the thermal history of the samples. An Analytical model is developed in chapter 6, To predict the crystallinity from the temperature inputs derived from the computational model. Validation of the model will be described in chapter 6. Finally, chapter 8 is also provide the conclusion of this research and supply recommendations for future research.

3

EXPERIMENTAL SET-UP

In this chapter, two classes of experiments necessary for our investigation are discussed. First, the experiments to obtain the desired material properties as input for the Finite Element Model are presented. These are followed by experiments to investigate the crystallization kinetics of PEKK .

3.1. MATERIAL PROPERTIES

The UD tapes of PEKK under investigation were supplied by Cytec. The properties independent of temperature are specified by the supplier and listed in table. The computational model also includes several heatsinks manufactured and patented by KVE. The different heatsinks tested are proprietary, therefore they are referred her as the KVE3 and KVE4 Heatsinks currently in use by Kok and van Engelen.
The glass transition and melting temperatures were respectively measured about 351 °C and 161 °C by DSC with a heating rate of 10 Ks^{-1}. The material properties needed in order to model the induction heating physics are: the specific heat: thermal conductivity and the electrical resistivity. In the following sections the temperature dependent material properties are discussed. The electrical resistivity was already determined by KVE in advance of the thesis.

3.1.1. SPECIFIC HEAT

The specific heat is the energy added to a material to increase the temperature by one degree. It is determined by using Differential Scanning Calorimetry (DSC). The tests were conducted on the CF/PEKK composites and two different heatsinks. The procedure followed is based on heating the specimen in a controlled rate and comparing it to a reference material with known specific heat. The standard reference material is Sapphire which has well defined specific heat. The specimens were placed in an aluminium cup. Measurement with empty cups where included, because the cups absorb heat and influence the heat flow. The specimens produced were with a diameter of approximately 5 mm and a mass varying between 7 and 10 mg. To compute the specific heat of the

materials the following equation is used:

$$Cp_i = \frac{60E \cdot D_i}{W_i \cdot b} \tag{3.1}$$

Where subscript i indicates the material and D, which is the vertical difference between the curves of the sample and the empty cup. W and b are the weight of the sample and the heating rate respectively. E is the calorimetric sensitivity as shown by equation (3.2).

$$E = \frac{b(W_s \cdot Cp_s)}{60 \cdot D_s} \tag{3.2}$$

Where b, W_s, Cp_s and D_s are the heating rate $[K/min]$, the mass of the reference sapphire $[mg]$, the specific heat of the sample $[J/(g*k)]$ and the vertical difference between the reference Sapphire and the empty specimen cup. Figure 3.1 shows the specific heat of the CF-PEKK specimen and reference materials sapphire and CF-PEEK [120].

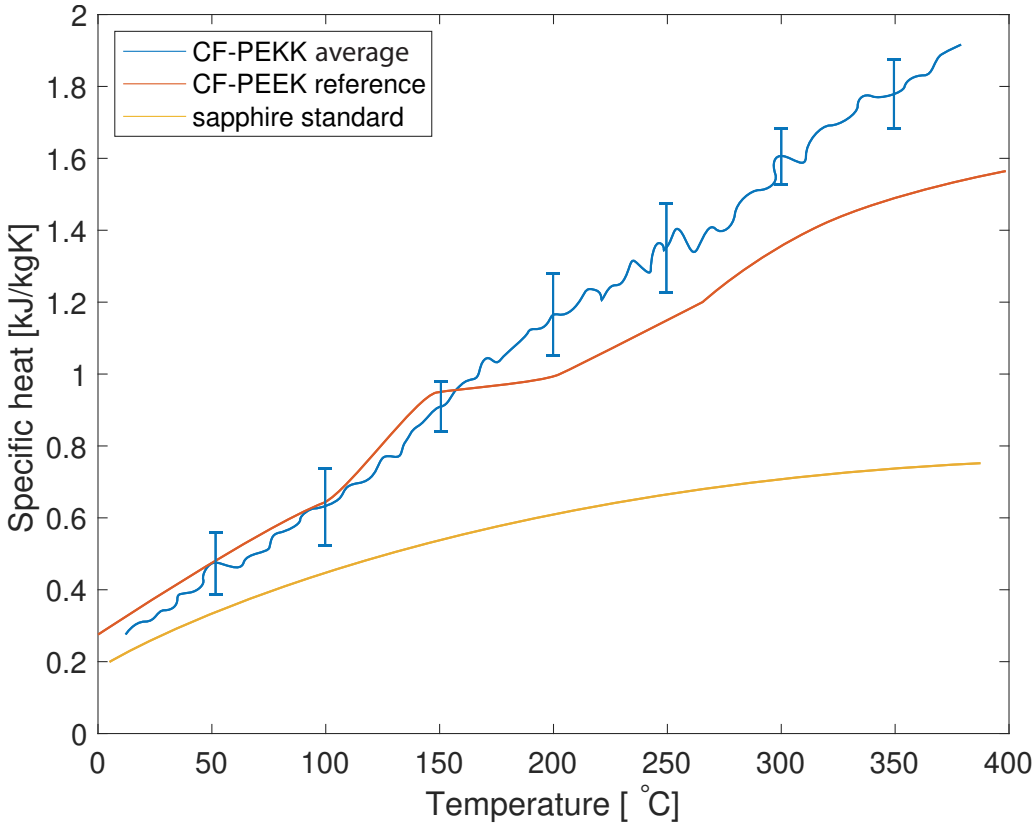

Figure 3.1: Computed specific heat of UD CF-PEKK

3.1.2. THERMAL CONDUCTIVITY

Coupon manufacturing

Laminates of 16 plies with a length and width of 70 mm were produced for the determination of the thermal conductivity. All the fibres in the plies are oriented in the same direction. The bonding areas of the laminates were sanded with P180 sanding paper, cleaned with acetone and air pressure to remove any particles from the sanding. The

laminates are stacked on top of each other until a height of 20 mm or larger was reached, paying attention to aligning the fibres of the different plies in the same direction. The laminates were bonded together using scotch-weld DP-760 and applying an evenly distributed pressure. The scoth weld between the laminates is cured at 80 °C for a period of 1 hour. As illustrated in figure A.1 the coupons are milled to the desired length and width of 20 mm with a CNC cutting machine ensuring proper surface contact when measuring.

Measurement

The thermal conductivity was found by using a C-therm Thermal Conductivity Analyser (TCi) [121]. The test is based on applying a known current to the sensor's spiral heating element, providing a small portion of heat. The result of the applied current is an increase in temperature at the interface between the coupon and the sensor. This increase in temperature produces a change in the voltage drop of the sensor element. A guarding ring shielding the primary sensor from the surrounding is included to ensure heat transfer into one dimension. The thermal properties of the sample are determined by the rate of increase in the sensor voltage. The voltage is a function of the temperature and the rate of increase of the temperature at the interface between the sensor and the coupon is inversely proportional to the thermal conductivity. The voltage is used as a procurator for temperature and will show curves with a small slope for higher thermal conductive materials (e.g metals) and more rising slopes for lower thermal conductive materials. The TCi is able to measure thermal conductivity up to 200 degree by placing the measuring device in a temperature controlled environment. Test are conducted at room temperature in the 3 different dimensions; the x direction is parallel to the fibers; the y direction is transverse to the fibers and z is the trough the thickness measurements. The test where conducted at room temperature and the average of 8 different runs is shown in table for the different orientations

As can been seen from table is the conductivity in the x directions a couple of factors higher. This is due to the fact that fibers dominate the thermal conductivity in this direction, whereas the y and z direction are dominated by the matrix material.

3.2. CRYSTALLIZATION KINETICS

As in the case of the previous measurements, the crystallization kinetics of CF/PEKK depend on temperature. As seen in the previous chapter, the supercooling is the driving force for crystallization. DSC quantifies the change in enthalpy of material that happens as a result of a phase transitions. The part of the heat flow curve where no transition occurs is called the baseline. As latent heat occurs, a peak appears in the curve, whereas the curve deviates from the baseline. The baseline is extended beneath the crystallization peak and called the interpolated baseline. This line would be a curve if all recorded heat would happen without any transition [122]. In the ideal case this would be a straight line with the same slope as the area between the glass transition peak and the melting peak [123]. If the on set point and the end of transition do not align, a tangential line should be considered for semi crystalline polymers with a significant C_p temperature function. This is the case for PEKK as can been seen in section 3.1.1. The area between the baseline and the curve represent the total energy needed for the phase change, from onset to the

last trace of crystallinity. This total energy is defined as the heat of fusion, ΔH_f and the degree of crystallization which can been found as described in section 2.1. There are two methods to measure the crystallinity in DSC experiments. Isothermal studies (constant temperature) and non isothermal studies (constant rate) experiments. Choosing the correct baseline is crucial for the evaluation of the phase transition [124]. The baseline were constructed using the Origin pro 8 software.

CALCULATION OF DEGREE OF CRYSTALLINITY

As the baseline is formulated for all the isothermal and non-isothermal experiments the total degree of crystallization is calculated with the area between the heat flow peak and the baseline. The amount of conversion from a amorphous state to semi crystalline state is given by the area, from the onset of crystallization until a certain time.

$$\Delta H(t) \int_{t_o}^{t} \frac{dH}{dt} dt \tag{3.3}$$

Were $\frac{dH}{dt}$ is the heat flow rate, t_o is the onset time and t is the time proceeded. Inserting the $H(t)$ heat of crystallization in equation (2.2) the degree of crystallinity is calculated. To determine the crystallinity induced within the material during processing, samples at the area of interest are cut with a water cutting machine. Water cutting is used to limit heat introduced during the cutting. The value of fusion enthalpy of melting is the energy needed for all of the crystallinity within the polymer to melt. The crystallinity obtained during processing is the fusion enthalpy of the glass crystallization (ΔH_{cc}) which is subtracted from the fusion enthalpy of melting. The crystallinity at the weld surface was calculated according to the following equation:

$$X_{weldsurface} = \frac{\Delta H_m - \Delta H_c}{\Delta H_m^0 \times (1 - W_f)} \tag{3.4}$$

where ΔH_m is the DSC measured value for the heat of fusion of melting and ΔH_c is the glass crystallization enthalpy.

HOFFMAN-WEEKS PLOT

The Hoffman and Weeks method is applied to find the equilibrium melting point [125]. Conducting runs at different isothermal temperatures the crystal develops different thickness of lamellae. Thicker lamellae melt at higher heats. Plotting the melting temperature of the crystals, formed by the isothermal run against the crystallization temperature of the isothermal runs, results in a line which is described by:

$$T_m = T_m^0 (1 - \frac{1}{2\beta}) + \frac{T_c}{2\beta} \tag{3.5}$$

Where σ is the lateral surface free energy and $\beta = \frac{\sigma l}{\sigma l_e}$ in which l is the lamellae thickness and the subscripts e refers to the lamellae thickness at equilibrium conditions. If the polymers are crystallized under equilibrium conditions β becomes equal to 1 and the slope converges to 0.5 in equation (3.5) The equilibrium melting temperature is derived

from the intersect of equation (3.5) and the line $T_m = T_c$ when $\beta = 1$. The testing procedure for CF/PEKK specimens starts with initial heating stage at 380 °C to remove any prior crystallinity within the PEKK, followed by cooling to the isothermal temperature at which the sample is tested. The CF/PEKK is kept at this temperature for 75 minutes to ensure complete crystallization of the PEKK has occurred. Thereafter the specimen was heated at a rate of 10 K/min and the end of the melting was found from the DSC data. The Hoffman-Weeks plots for the cytec material is shown in figure 3.2

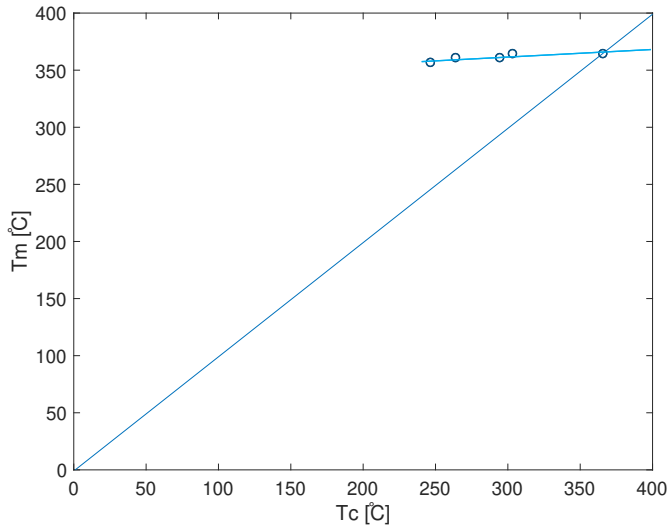

Figure 3.2: Hoffman-weeks plot for CF/PEKK form Cytec, with a T_m^0 of 354,5 °C.

The intersection of the two lines is at 354,5 °C. This T_m^0 would indicate a (T/I) ratio of 70/30 as derived from figure 2.4.

3.3. PRODUCTION LAMINATE

The CF-PEKK UD laminates used in this research. Have a lay-up of $[90/45/\text{-}45/0/]_S2$ and consisting of 16 plies. The total dimensions of the laminate produced are 700mm by 1800mm. From this plate multiple weld samples could be produced. The plates were manufactured with the help of the autoclave cycle shown in figure 3.3 and the bagging instructions of figure 3.4. During the autoclave run the part was heated from RT, 24°C, to 377 °C ± 5.5 °C at any available rate. As soon as the laminate is equilibrated at process temperature (377 °C) a pressure of 6.89 bar ± 0.34 bar is applied. Hold pressure and temperature at 377 °C for 20 +10/-5 minutes. As the laminate is consolidated the part is cooled at a rate of 10 °C maintaining the pressure until a temperature of 120 °C is reached.

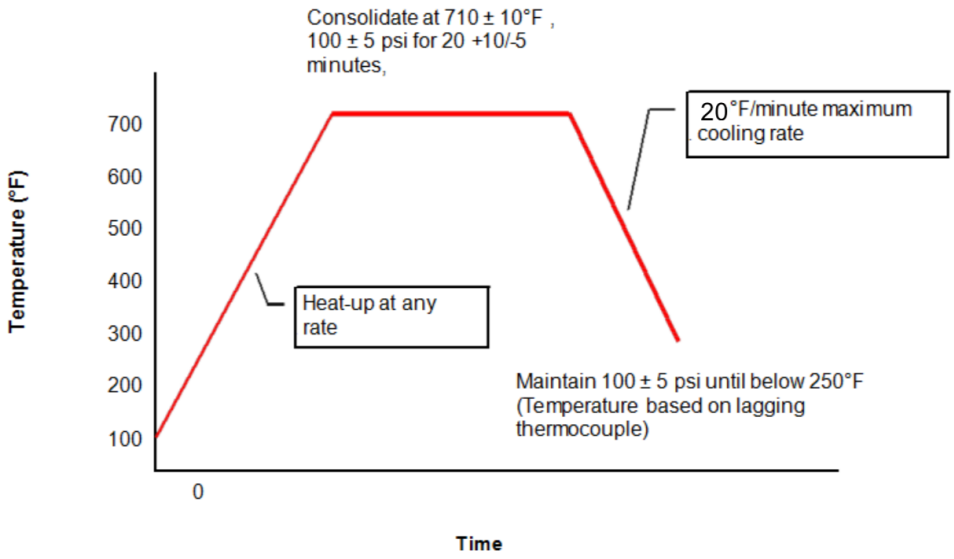

Figure 3.3: Autoclave instustructions supplied by solvay [54]

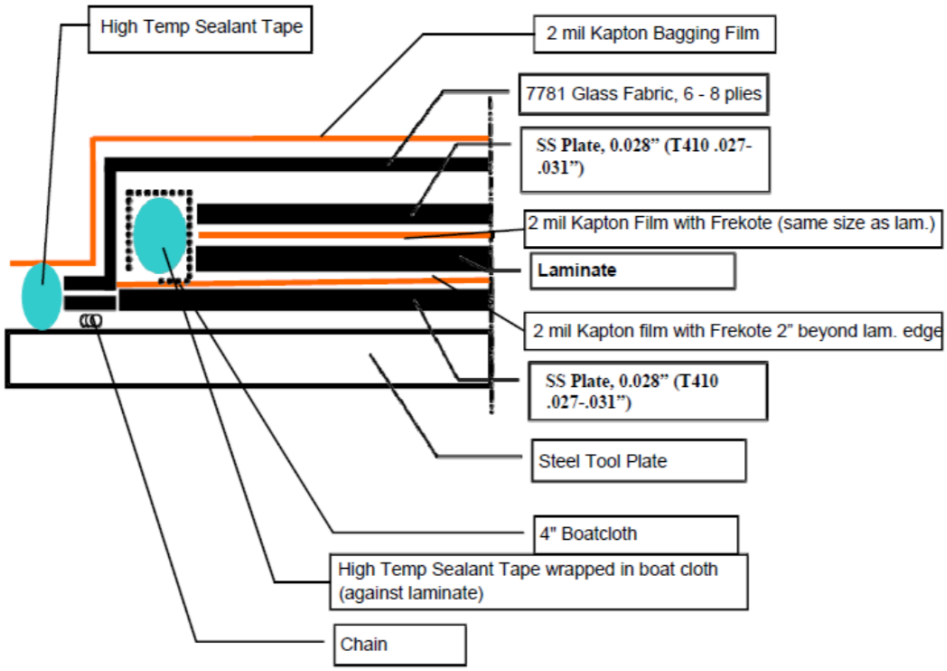

Figure 3.4: bagging instustructions supplied by solvay [54]

From the large consolidated plate, 12 plates of 610mm by 101mm where milled. The laminates were milled to the correct size of the single lap shear as indicated by the ASTM D3163 standard.

4

COMPUTATIONAL MODEL

The computational model will be used to determine the effect of process parameters on the cooling rate of UD CF/PEKK. This chapter addresses the question concerning the influence of processing parameters on the crystallinity developed. The modelling is done with a commercial FEM software: Ansys. There are two types of experiments conducted, Static induction welding experiments with the coil kept steady on one spot and the dynamic experiments with the coil moving form the start to the end of the overlap.

4.1. MODEL SET-UP

In practice, the focus is usually on reaching a desired temperature while neglecting the effect of cooling rate on the quality of the weld. Therefore FEM will determine the effect of the parameters on the cooling trajectory, since during induction welding the laminate may experience arbitrary thermal histories. The current models aim at predicting Differential Scanning Calorimetry (DSC) like conditions (constant temperature or constant rate). Hence most of the kinetic models have little practical application. A differential form of the crystallization kinetics model, including the induction time for the onset crystallization is desired. To run the electromagnetic and sub-sequential thermal analyses several process parameters and material properties are needed. A summary of the desired parameters is given in table 4.1

Table 4.1: Desired parameters computational model

Parameter	Unit	Description
Process parameters		
w,l,t	[mm]	Geometry (width, length and thickness)
I	[A]	Excitation current
f	[Hz]	Frequency current
T_i	[T]	Ambient temperature
eszp	[m]	Target element size plate
t_{heat}	[s]	Induction heating time
t_{end}	[s]	Time to continue thermal analysis after heating
t_{step}	[s]	Step size transient analysis
Thermal material properties		
κ(x,y,z,T)	[W/(m · K)]	Thermal conductivity as function of temperature[6]
c	[J/(kg · K)]	Specific heat capacity material [6]
D	[kg/m^3]	Density material [6]
h	[W/(m^2 · K)	Heat convection laminate boundaries
e	[-]	Emissivity material [6]
K_g	[K^2]	Activation energy diffusion of chains
U^*	[J/mol]	Activation energy nucleation
Electrical material properties		
ρ(x,y,z,T)	[Ω· m]	Electric resistivity as function of temperature[6]
ϵ'	[-]	Relative permittivity constant laminate [7]
ϵ''_{eff}	[-]	Relative permittivity loss factor laminate [7]
μ_r	[-]	Relative permeability scalar[6]

The computational model is based on the flowchart illustrated in figure 4.1

[6] For coil, air, water, laminate and heatsink
[7] Only non ferromatic materials are use so is presumed to be equal to one

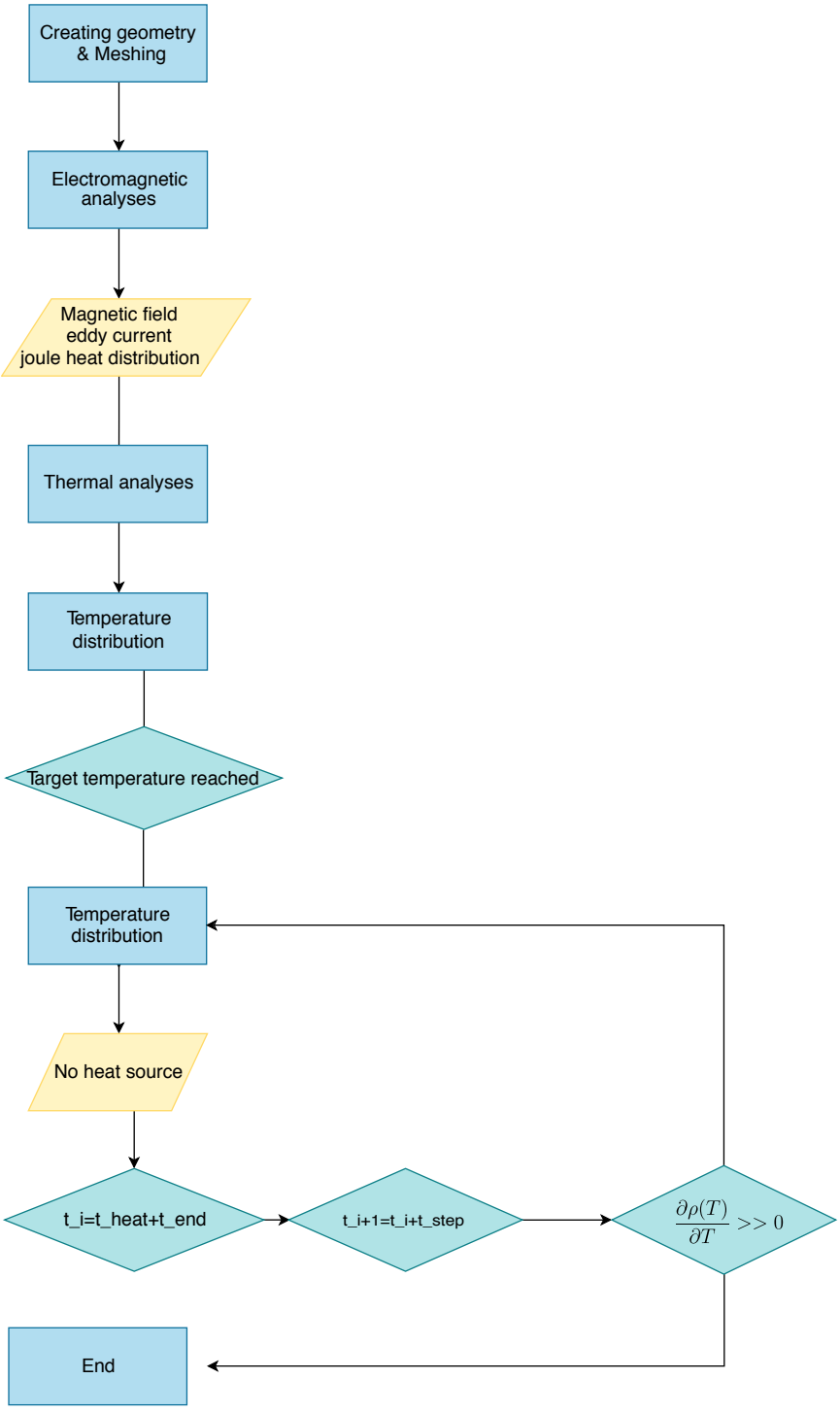

Figure 4.1: Flow chart FEM

The model starts by defining the geometry and meshing it. The input parameters, material properties, applied boundary condition and element types are assigned to the nodes and elements generated by the meshing. The applied current is an initial guess value. From there on the harmonic Electromagnetic (EM) analysis is started. The results of the EM analysis are the eddy current distribution and the amount of joule heat generation. Followed by a thermal analysis where the heat generation from the previous analysis is

assigned as a body load in the thermal analysis. The thermal analysis predicts the heat as a result of the joule heat generated during the EM analysis. This process is repeated until the time is reached that the induction coil is turned off. If the desired temperature 380 ± 10 °C at the weld line is reached, the analysis with no heat source proceeds. In the case that the desired temperature is not reached, the input value for current is changed in order to recompute the desired temperature. If the desired temperature is still not reached, a third applied current is determined by a power law relationship between the first two results. This result in reaching the desired temperature. The analysis proceeds and calculates the temperature distribution until the final time is reached.

4.1.1. GEOMETRY

The main geometry modelled has the geometry of a single lap shear specimen. The two plates are double symmetric $[90/45/\text{-}45/0]_{S2}$ and have 16 plies each. The overlap between the plates is 3/4 of an inch and the width of the plates is kept constant at 100 mm. Each ply was modelled separately and stacked to form the laminate. Between each layer a small separation layer was modelled. This is done because Ansys does not provide the option to include a surface resistivity between the layers. By including a small separation layer, the surface resistivity can be replaced by the resistivity of the small separation layer. The small separate layer of 1/1000 mm is equivalent to a resin rich layer of the UD tape. The manufacturing method of UD tapes results in a small resin rich layer on top of the carbon fibres. This layer will prevent direct contact between CF and will influence the heating of the composites. The angle between adjacent plies is of influence on the surface resistivity, within the lay up angles of 90°, 45°and 0°, which are encountered between adjacent plies. The 90 and 0 degree plies have resistivities in the order of 600 ω/m, whereas the resistivity of the 45 degree orientation tends to 0. The coil used is the patented induction coil by KVE composites and due to the confidentiality statement it is not been shown or discussed in detail. The heatsinks used are the patented KVE3 and KVE4 heatsink differing in their thermal properties. KVE3 has a factor five higher thermal conductivity compared to KVE4, which has anisotropic properties. The width of the KVE4 heatsink is twice as large than the KVE3 heatsink. The large body compensates for the lesser thermal conductivity of the heatsink.

The complete single leg shear and coil geometry is surrounded by air. The air is included to model the alternating magnetic fields. The dimensions of the air are taken such that it's large enough so that any edge effects on the magnetic field are reduced, but also small enough that unnecessary extra computational time is reduced. Due to the large aspect ratio of the laminates and separate plies (relative width and length are much larger than thickness), meshing becomes problematic. The small edges in contrast to the overall size of the model cause a problem. To overcome this, the air is divided into domains in the vicinity of the small edges. Figure 4.2 illustrates a schematic of the FEM model. The blue plates illustrate the plies, the red plate illustrates the heatsink and the coil is shown grey.

4.1.2. CONSTRAINTS

There are two types of constraints that impact the simulations; magnetic constraints and heat transfer constraints. For the electro-magnetic analysis the initial magnetic vector

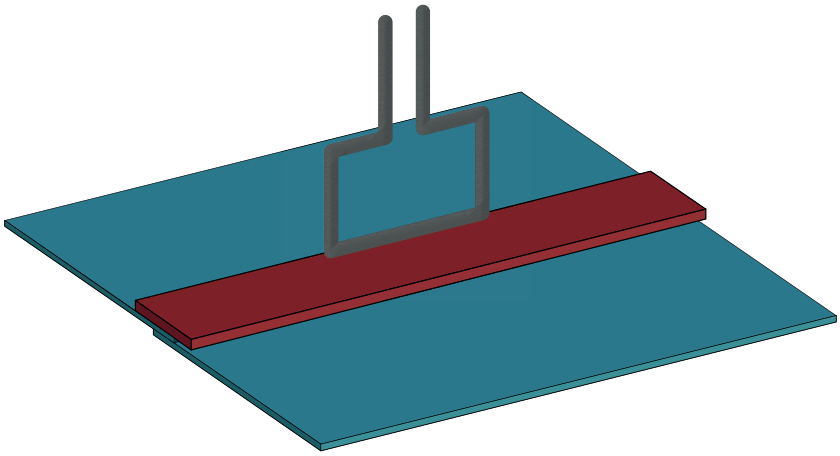

Figure 4.2

and the initial electric potential are set to zero for all the domains. The external faces of the air (the outer surfaces of the model) are simulated as magnetically insulating. The flow of current through the coil was indicated by specifying the start and end point of the coil.

A preliminary model to this thesis only accounted for heat conduction constraints. In the heating phase. The magnetic field results in increasing temperatures at the weld area, transferring heat is transferred to the surrounding material.In this phase, due to the high conductivity of the carbon fibers the heat conduction is dominant over heat convection and the latter is therefore neglected [126]. However, for this research special attention is paid to slower heating rates and the cooling trajectory. Cooling will occurs over a larger time period than in the heating stage, which makes the effect of convection more pronounced. The importance of different parameters during cooling differs when compared to the heating stage.

SYMMETRY CONDITIONS

The main geometry exhibits a mirror symmetry across the center of the laminate in the length direction. The first simulations of the full model showed a clear symmetry of the magnetic field produced and the heat pattern, indicating that computational time could be reduced by applying symmetry within the model. Since there is a clear mirror symmetry plane, the magnetic insulation boundary condition represents a magnetic mirror plane. This means the magnetic field will exactly be mirrored as the mirror plane is crossed. The condition also implies the magnetic field is zero in the normal direction to the boundary. This dictates that the symmetry can only be implied if the plane cuts perpendicular to the complete microscopic current density $\boldsymbol{J}$ and is parallel to the magnetic field $\boldsymbol{B}$ [127]. To apply this boundary condition in Ansys the faces of the laminate at the mirror plane should be assigned a zero volt condition and all external faces and all faces at the mirror plane should be assigned Flux-parallel magnetic boundary condition.

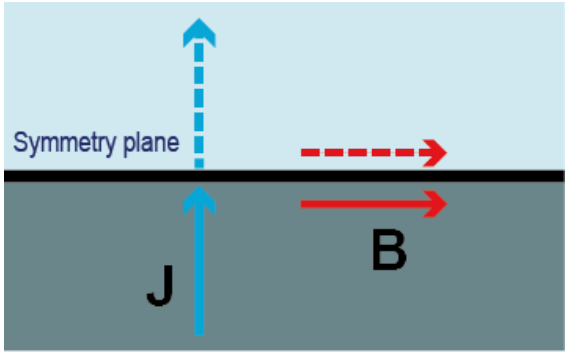

Figure 4.3: The Magnetic Insulation boundary condition: mirror perpendicular to $\boldsymbol{J}$ and parallel to $\boldsymbol{B}$

4.1.3. MATERIAL DEFINITION

The material properties dependent on the temperature, Determined in Chapter 3 were imported into ANSYS. The plies are assigned the anisotropic material properties according to a local coordinate system aligned with the fibre angles. The ply properties are taken as a constant and the local coordinate system differentiates between anisotropy of the plies. A small separation layer is modelled between all the plies to model the surface resistivity. The material properties of air are adjusted from the library included by ANSYS. The electric conductivity is decreased to be 1000 time smaller than the smallest conductivity found within the laminate, preventing current to leak from the laminate into the air domain. The material properties of the copper coil were considered as relative permeability of 1 and a resistivity of $1.7 \cdot 10^{-8}$.

4.2. SIMULATION RESULTS

Simulations provide the possibility to examine what is happening within the composite. The following section discusses the effect of welding time on the through the thickness temperature distribution, the weld pool area, cooling trajectory and cooling rate for both heatsinks. An overview of the relation between current and welding time to the maximum temperature will be provided. For the KVE4 heatsink the effect of different stack-

ing sequences will be analysed. The current was adjusted to reach the desired welding temperature for different welding times. The different welding times where generated by the Sobol sequence spanning the design space. The Sobol sequence is a quasi-random sequence, which is designed to generate samples of multiple dimensions as uniformly as possible for multiple parameters [128]. New sample point are chosen under consideration of previously sample points, this avoids to formation of clusters and prevents gaps within the sample distribution. Often the first five point generate by the Sobol sequence will be discussed to illustrate effects. First, the highly thermal conductive KVE3 heatsink will be discussed, followed by the lesser conductive anisotropic KVE4 heatsink.

4.2.1. KVE 3

THROUGH THE THICKNESS

First the through the thickness heat pattern is evaluated. To prevent degradation of the PEKK matrix it is important to prevent temperature exceeding 400 °C. In the optimum situation the maximum temperature will be located at the weld interface. KVE3 has an exceptional good thermal conductivity, preventing thermal degradation even at fast welding times and high current. The high currents generate a lot of energy within the plates at a short time period, so fast cooling is needed to prevent overheating. Figure 4.4 illustrates the through the thickness temperature distribution of 4 different welding times. What is interesting about the distributions in this figure is that longer welding times result in a more even temperature distribution around the weld interface located at the 0 at the z axis. Turning now to the temperature difference between the interface at the heatsink and the weld interface, the results show a large difference between both interfaces.

WELD POOL AREA

The weld pool area is the area where temperature exceeds the T_m of 350 °C. PEKK exceeding this temperature will be in the molten state and is capable to diffuse across the weld interface and entangle with the polymer chains of the opposite plate. These chains are of interest because they could cocrystallize as described in section 2.3. Figure 4.5 and Figure 4.6 present a contour plot of the temperature distribution at the weld interface. The line in the middle indicates the position of the coil. The overlap in the single lap shear configuration has two sides in close vicinity of the air. The top plate of the bottom plate will lose more heat than the bottom side of the top side due to convection. As a consequence the heat pattern shifts to the side of the top plate. The gradient observed is an indication of the cooling rates. Higher temperature gradients will result in larger cooling rates. A comparison for weld pool area at different welding times shows an increase in weld area when increasing the welding time.

From the graphs above we can see that the weld pool area increases as the welding time increases. Figure 4.7 illustrates this relationship even more, the area at the weld interface exceeding 350 °C is plotted against the welding time. The orange dots illustrate the areas with the maximum temperature between 378 and 382 °C. Increasing the maximum temperature results in an increase of the total weld pool area, whereas lower maximum temperatures results in smaller areas. What is interesting about the data in this figure is

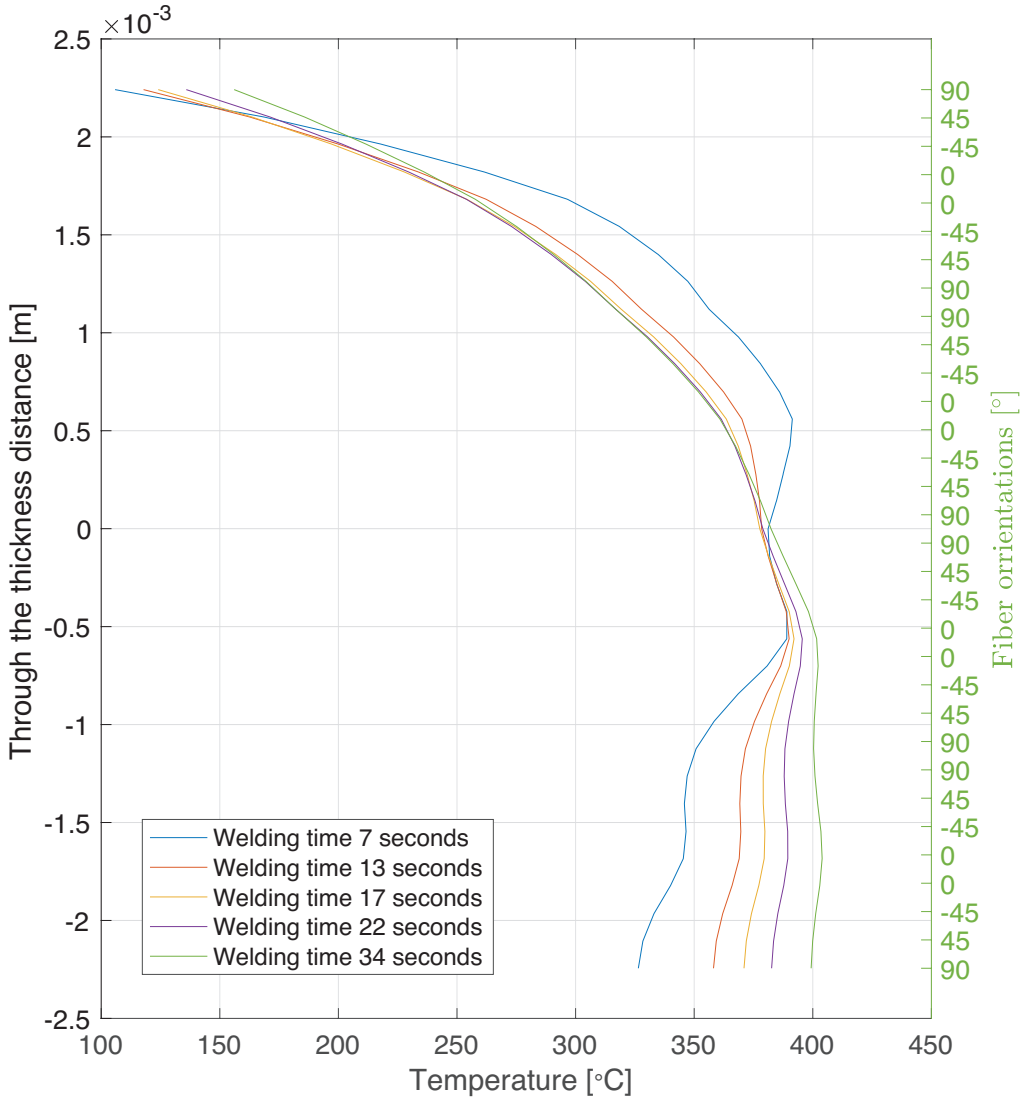

Figure 4.4: Through the thickness temperature distribution when cooling with the KVE3 heatsink. The weld interface is located at 0. The rigth axis illustrates the different ply orientations

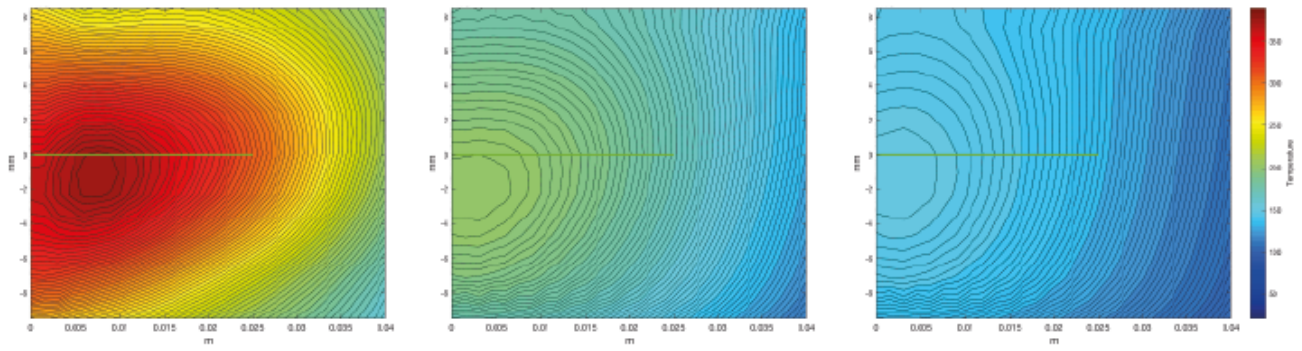

Figure 4.5: Cooling pattern 7 seconds after induction welding and after coolin for 27 and 47 seconds with KVE3 heatsink and 380 degree maximum temperature

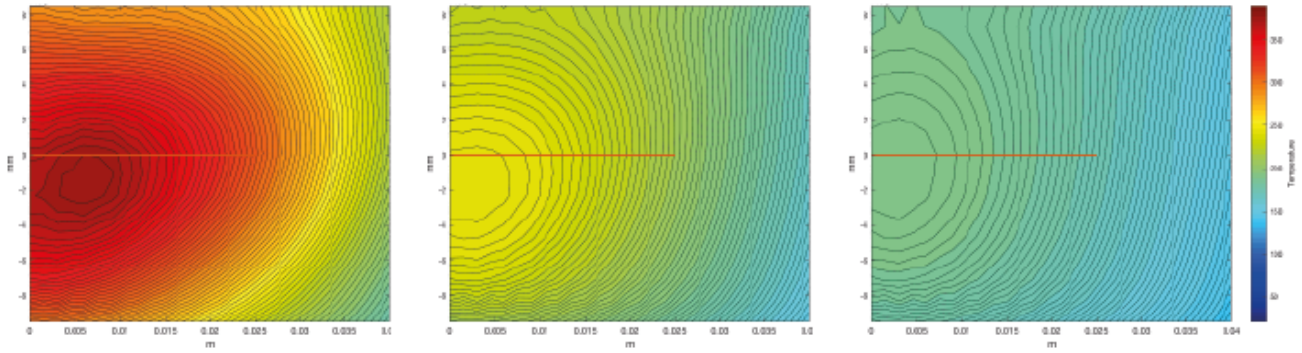

Figure 4.6: Cooling pattern 36 seconds after induction welding and after cooling for 56 and 76 seconds with KVE3 heatsink and 380 degree maximum temperature

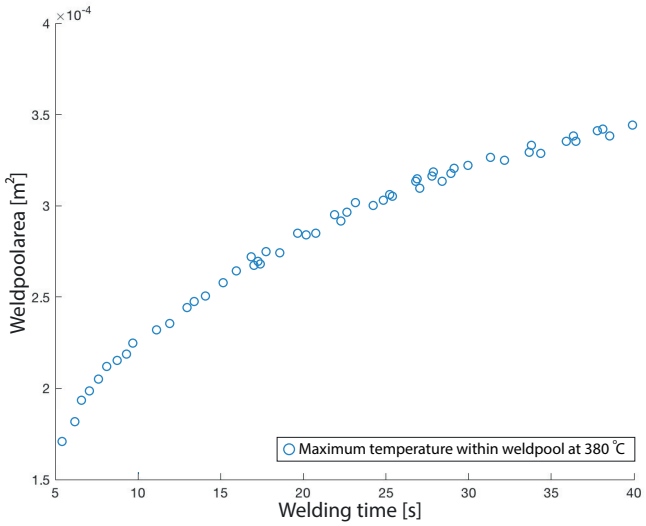

Figure 4.7: Weld pool area versus welding time cooled with KVE3 heatsink

that the weld pool area almost doubles as the welding time increases by a factor of five.

COOLING TRAJECTORY & COOLING RATE

The cooling trajectories of five different welding times are shown in figure 4.8. The figure shows the influence of welding times on the cooling rate; longer welding times result in slower cooling rates. All cooling trajectories follow the same shape, the first part is almost the same, at longer times the paths start to deviate. As crystallization happens between the temperatures of 300 °C and 200 °C, the cooling rate at this region is of interest. Figure 4.10 illustrates the cooling rate of the above five cooling trajectories between the region of interest. As described in section 5.3.1 lower heating rates results in a higher degree of crystallinity, whereas the maximum crystallization rate of non isothermal crystallization is reached at 270 °C, as can be seen in figure 2.14. Higher cooling rates lower the temperature nucleation time as mentioned in chapter 3. Cooling with 140 °C/min is able to suppress crystallization and will produce an amorphous structure. As can be seen from the figure cooling rates are above 140 °C/min, which is a strong indication that the weld surface will be in an amorphous state. The KVE3 heatsink is optimal to reduce the welding time, but for PEKK with the single lap shear set up of 16 plies, the KVE3 heatsink will produce high cooling rates, which will limit the crystallization at the weld surface. Although the longest welding time could result in some crystalline regions at the interface. The overall influence of welding time on the cooling rate is illustrated in figure 4.9. From the figure the trend is clear, the continual decline of cooling rate with increasing welding times.

THE EFFECT OF COIL CURRENT AND WELDING TIME

It can be seen from the data in figure 4.11 that there is a clear relation between welding time and current. The blue lines within the figure illustrate the region between 350 °C and 400 °C. Increasing the amount of sampling points for the simulation would result in more continuous lines without abrupt direction switches.

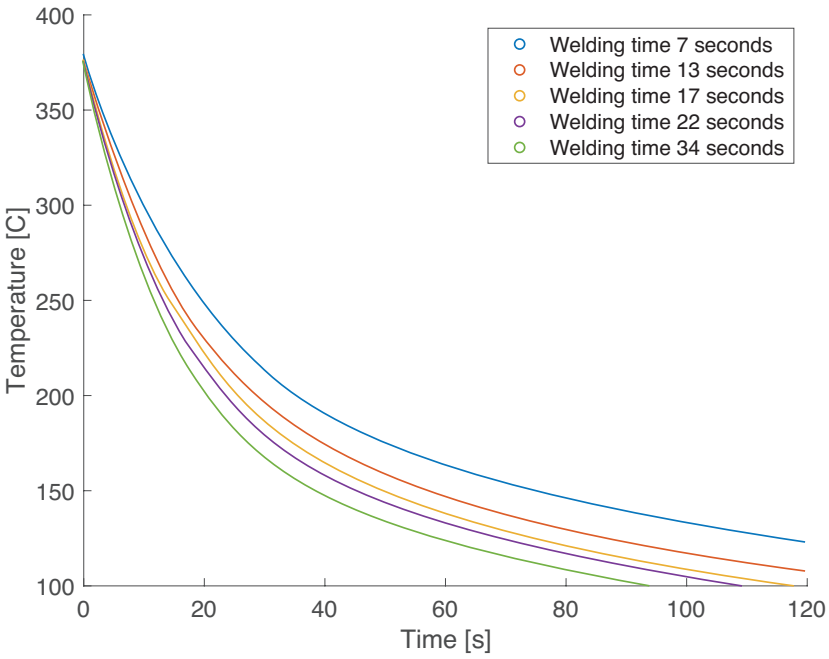

Figure 4.8: Cooling trajectories of 5 different cooling times after welding with the KVE3 heatsink.

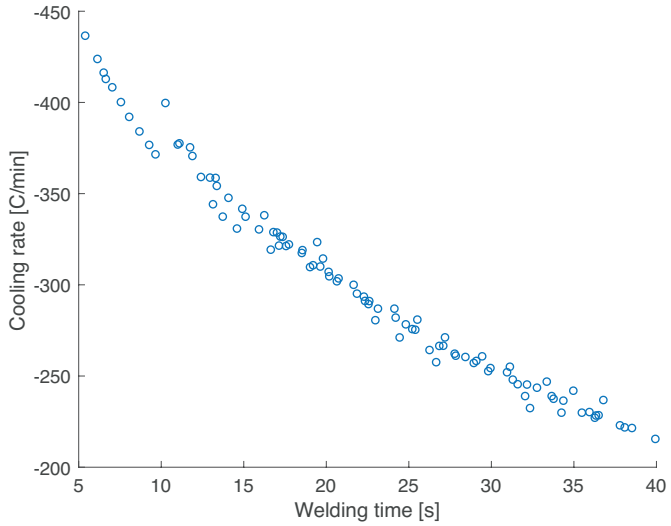

Figure 4.9: Cooling rate versus welding time cooled with KVE3 heatsink

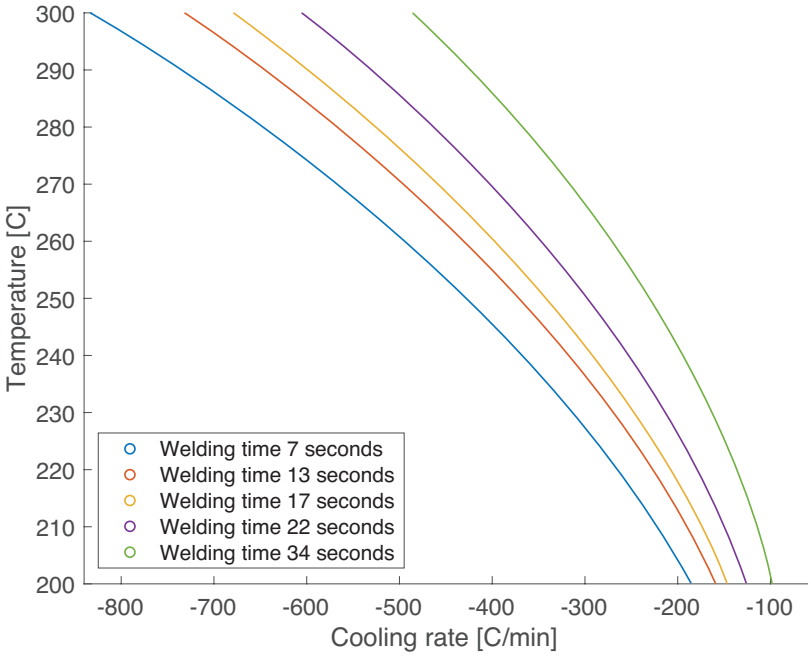

Figure 4.10: Cooling rate between 300 °C and 200 °C

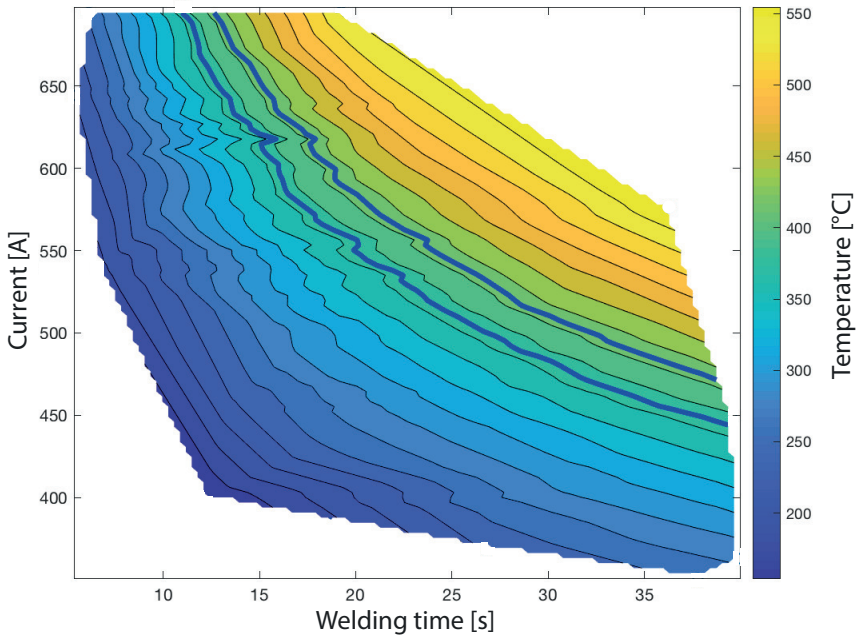

Figure 4.11: Effect of current and welding time on the temperature when welded with KVE3 heatsink

4.2.2. KVE4

KVE4 has a factor 5 lower thermal conductivity. The KVE4 heatsink differs from KVE3 in that it is anisotropic compared with the isotropic KVE3. The thermal conductivity of the longitudinal direction is a factor 15 larger than its transverse direction.

THROUGH THE THICKNESS

The through the thickness temperature distribution shows the same trends as the KVE3 heatsink; longer heating times results in a more even temperature distribution. The fastest welding that occurs during 7 seconds results in temperatures exceeding the degradation temperature. The KVE4 heatsink is not capable of removing sufficient heat from the plates. The temperatures at the interface of the heatsink and the top plate are higher than those of the KVE3 heatsink. As can be seen from figure 4.12 varying the weld time results in different temperature distribution; longer weld times results in slower heating rates, but the location of the maximum temperature moves to the second plate. This indicates that the heatsink removes more heat than needed. Consequently, the cooling rates are higher than for the optimum configuration. This points out that for different welding configurations specific heatsinks could be designed to optimize the temperature distribution and lower the resulting cooling rates. An implication of this is the possibility that heatsinks are designed to maximize the crystallinity at the weld interface. The numbers on the right side of the graph indicate the fibre orientation of the ply at the discrete z location.
The most surprising aspect of the graph is in the drop in temperature between the 90 °and 45 °ply orientation at the top plate (also observed in the bottom plate for the fastest welding time), indicating that the main heat sources are the surface resistivity between orientation of 90°an 0 °, whereas 45 °has only little contribution for heat generation.

THE EFFECT OF COIL CURRENT AND WELDING TIME

The effect of coil current and welding time on the temperature at the welding interface between the two CF/PEKK laminates are summarized in figure 4.13, where the processing window for CF/PEKK welding between melting and degradation of the polymer matrix, can be drawn. The blue lines in figure 4.13 limit the parameters value leading to the acceptable temperature range at the welding interface. The lowest blue line equals 350 °C and the upper blue line equals 400 °C. There is a clear relationship between current en welding time. Comparing the figure with figure 4.11 of the KVE3 heatsink, KVE4 differs in the ways that amount of current to be supplied by the coil to reach the desired temperatures. The KVE3 extracts more energy from the plates. To reach the same temperature for a welding time of 32.5 seconds, the input current has to be 400 ampere for the KVE4 heatsink in comparison to 475 for the KVE3 heatsink. The difference is more pronounced for longer welding times.

WELD POOL AREA

The heat patterns of the weld pool area differ from the KVE3 heatsink. The anisotropic properties result in a heat pattern that is stretched within the thermally high conductive direction. Changing the orientation of the thermally conductive direction, changes the stretching of the heat pattern in opposite direction. This result is somewhat counter-intuitive, since the longer welding times result in smaller weld areas as observed for the

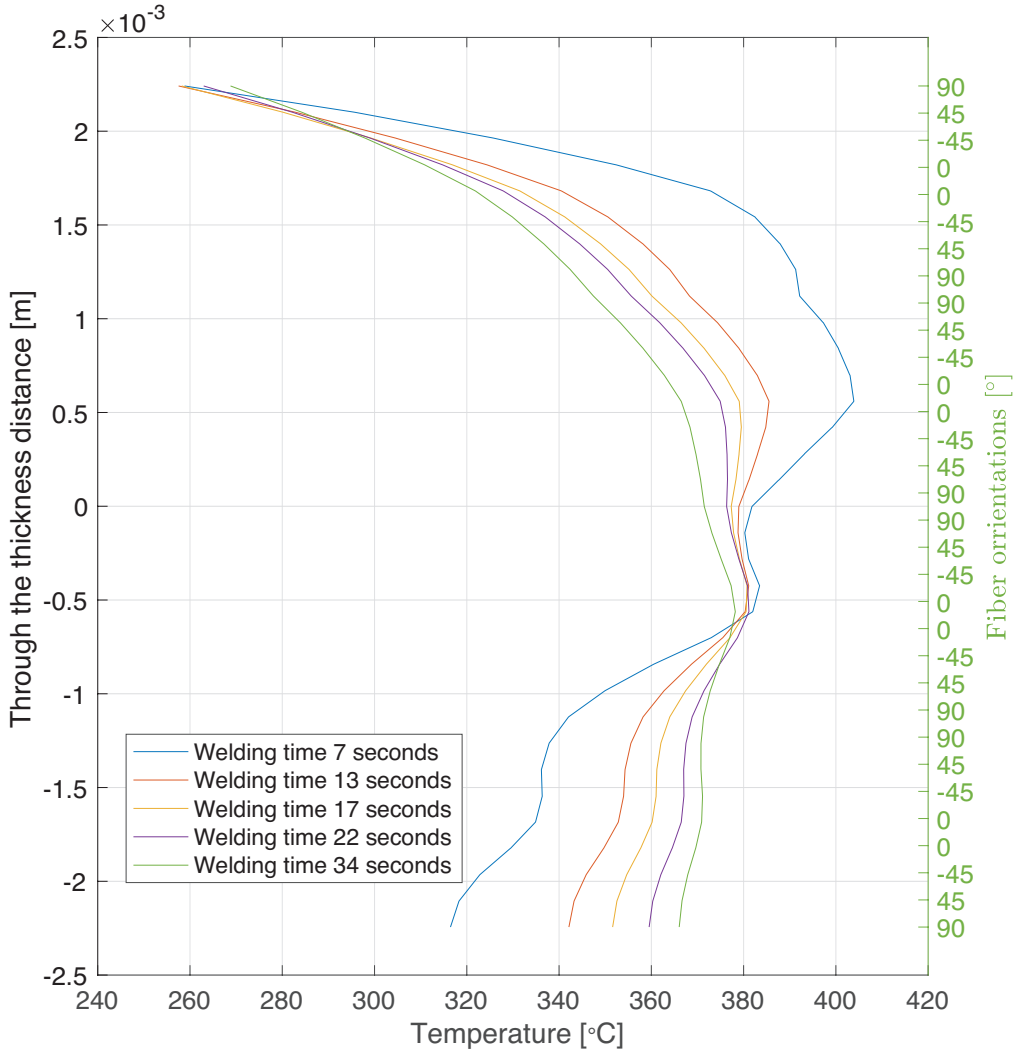

Figure 4.12: Through the thickness temperature distribution when cooling with the KVE4 heatsink.

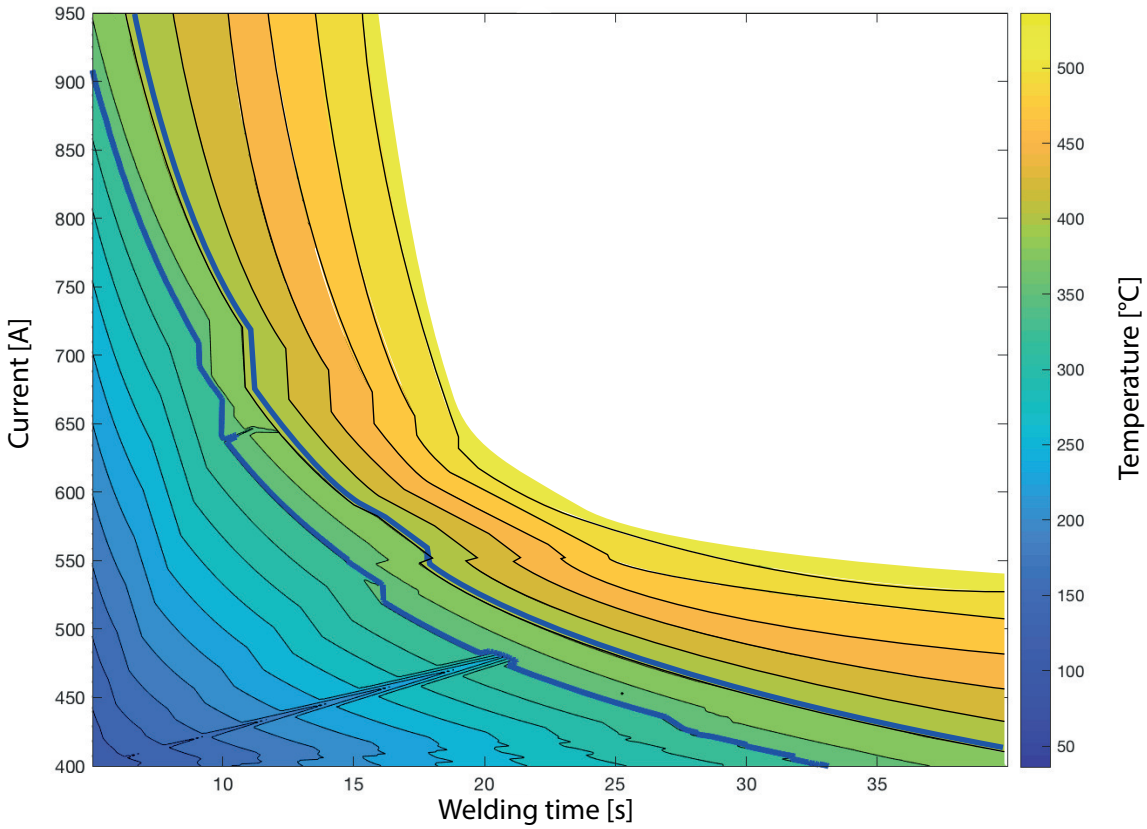

Figure 4.13: Effect of coil current and Welding time on the temperature at the welding interface between two CF/PEKK laminates

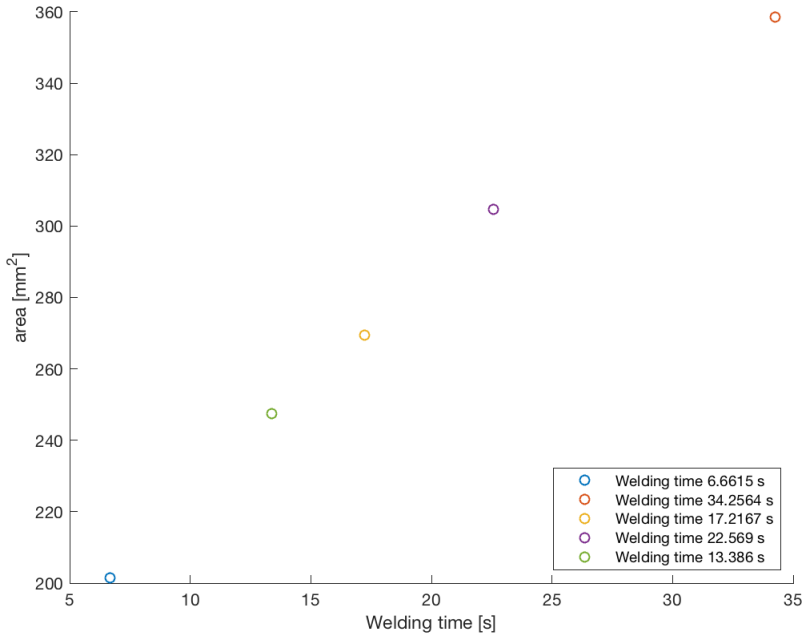

Figure 4.14: Through the thickness temperature distribution when cooling with the KVE4 heatsink.

KVE3 heatsink. This can be explained by a larger magnetic field required to reach the same amount of the temperature for the KVE3 heatsink compared to the KVE4 heatsink. The lower energy input results in a smaller affected weld pool area. A large bond area should increase the strength of the bond, indicating the specimens welded with the KVE3 heatsink should produce a higher bond strength. Although crystallization is an other important factor contributing to the final bond strength.

COOLING TRAJECTORY & COOLING RATES

The cooling trajectories have the same shape as predicted by Newton is cooling law, equation (4.1)

$$\frac{dQ}{dt} = h \cdot A \cdot (T(t) - T_f) \tag{4.1}$$

where Q is the thermal energy, h and A are the heat transfer coefficient and surface area respectively. $T(t)$ and T_f are the temperature of the object and the temperature of the environment. As the temperature difference between the environment and the weld interface is large (a large temperate gradient) much energy is removed from the weld interface and the cooling is fast. This can be seen at the start of the cooling trajectories. As time proceeds and the temperature gradient decreases, the cooling rate decreases. This explains why a more even temperature distribution within the laminates is desirable when aiming to maximize crystallinity. Figure 4.15 and 4.16 illustrate the cooling trajectories and cooling rates of five different welding times, cooled with the KVE4 heatsink respectively. There is a large difference in observed cooling rates for the KVE3 and KVE4 heatsink. There is a much larger region in which KVE4 are capable to crystal-

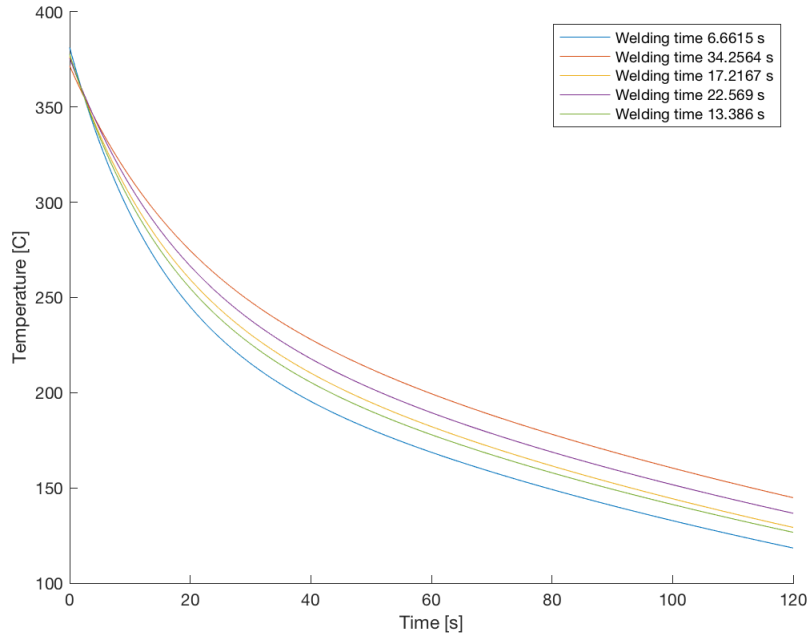

Figure 4.15: Cooling trajectories of 5 different welding times after welding with the KVE3 heatsink.

lize. The onset temperature is reached at higher temperature and the overall cooling rate is lower, which provides time for the polymer chains to crystallize. On bases of comparison between both cooling rates, one would suspect to find a sufficiently higher degree of crystallization for the KVE4 heatsink in comparison to the KVE3 heatsink. Figure 4.17 illustrates the relation between time and average cooling rate. The correlation between time and cooling rate is clear; longer welding times result in slower cooling rates. The sampling point are clustered into 5 different curves. This is due to power curve method used to reach the desired temperature.

The cooling patterns observed for the KVE4 heatsink differ from the KVE3 heatsinks. There is a lower temperature gradient and the heat is more evenly distributed within the weld surface. Due to the lesser conductivity of the heatsink the heat is removed slower from the weld spot and lower cooling rates are obtained. The trajectories and cooling rates for different welding times for the KVE4 heatsink are also closer together; the lesser conductivity causes the heatsink to have a lower overall influence on the cooling.

The KVE4 heatsink is also special due to its anisotropy, directing the conductive direction parallel or transverse to the induction coil result in different cooling patterns. The direction of highly thermal conductive direction of the heatsink dominates the shape of the cooling pattern, as can be seen from the difference between figure 4.20 and 4.21 where the KVE4 with the conductive direction parallel to the coil results in a more ellipse shape in the parallel direction. As the conductive direction is rotated, the ellipse shape of the cooling pattern shifts in the same direction. The initial shape shows little differ-

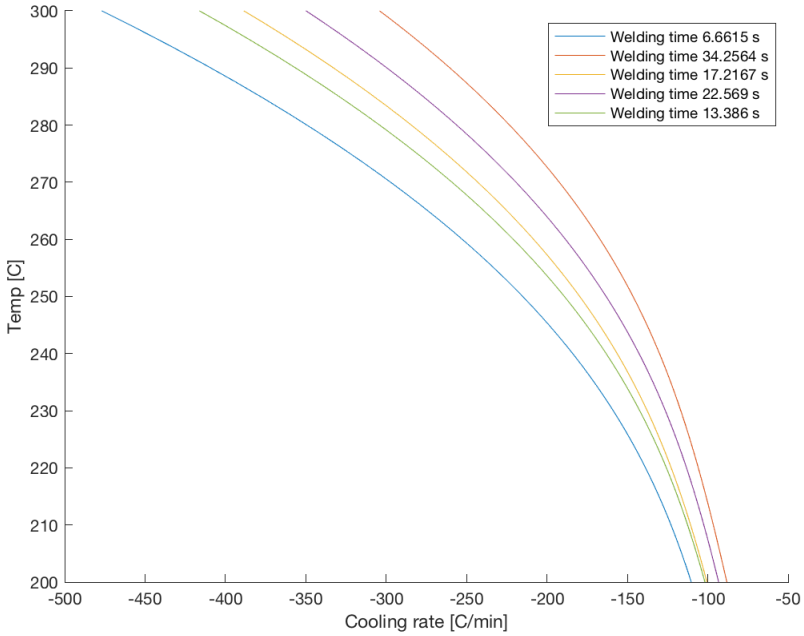

Figure 4.16: Cooling rate of 5 different welding times between the crystallization region with the KVE4 heatsink.

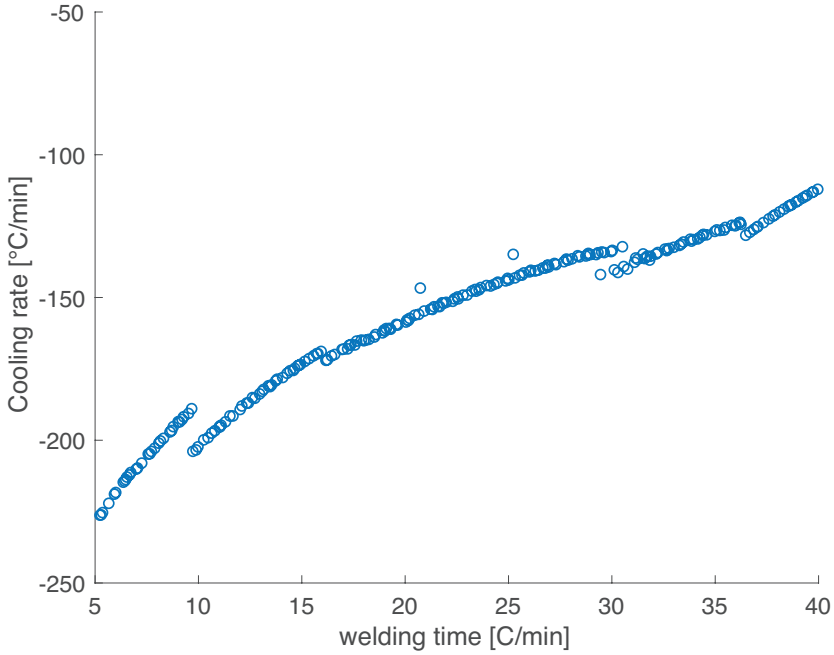

Figure 4.17: Relation between welding time and cooling rate

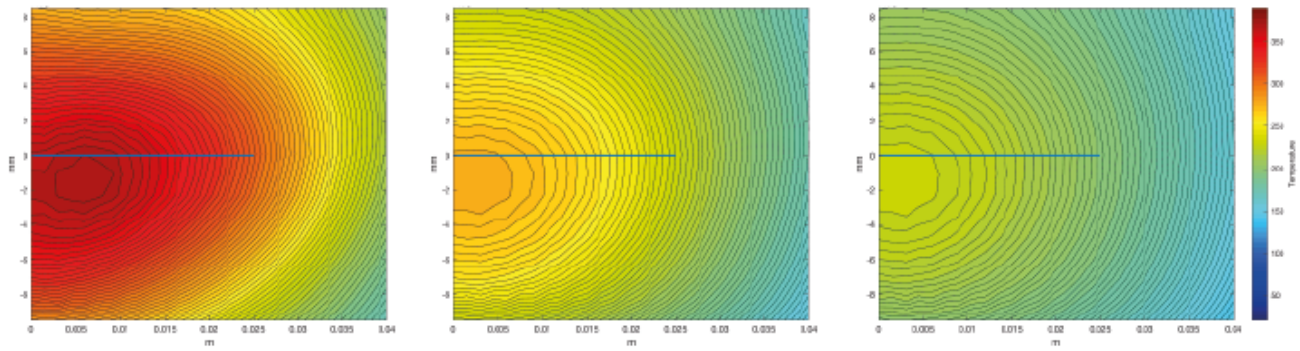

Figure 4.18: Cooling pattern after induction welding 36 seconds and after 56 and 76 seconds with KVE4 heatsink and 380 degree maximum temperature

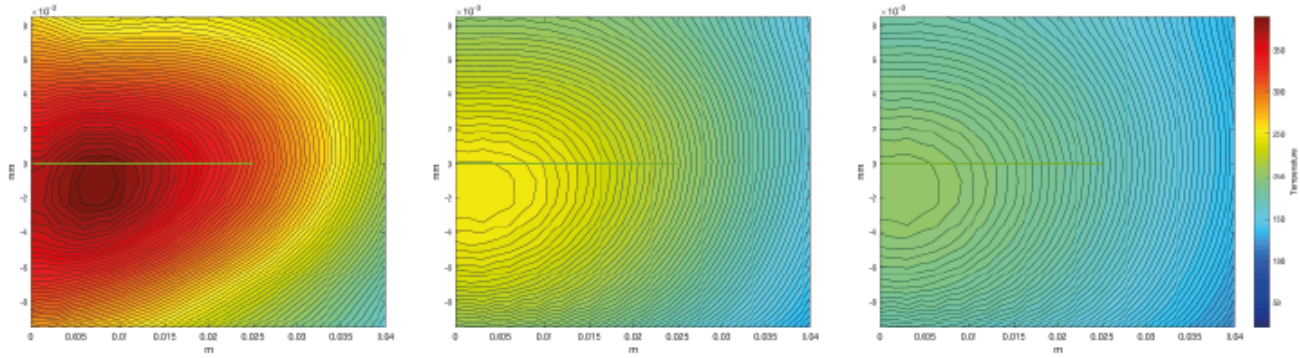

Figure 4.19: Cooling pattern after induction welding 7 seconds and after 27 and 47 seconds with KVE4 heatsink and 390 degree maximum temperature

ence, but as time proceeds and the heat is transferred by the heatsink the patterns start to differentiate from each other.

The simulations of the KVE4 heatsink with a maximum temperature of 380 °C will be the benchmark simulation within this research. Alterations to reduce the cooling rate and the resulting crystallinity will be compared to the benchmark KVE4 simulation.

4.2.3. CONCLUSION

The simulations show the effect of the heatsinks for different welding times. For both heatsinks one can concluded that increasing the welding time results in a more even temperature distribution within the composite. Longer welding times increases the weld pool area. Which will most likely result in higher bond strength. The longer welding will result in in lower cooling rates which will be beneficial for the degree of crystallinity. Comparing the through the thickness temperature for both heatsink, one can conclude that the lower conductive heatsink will result in more even temperature distribution while preventing degradation this indicates that an even lower conductive heatsink could still prevent degradation, while resulting in even lower cooling rates.

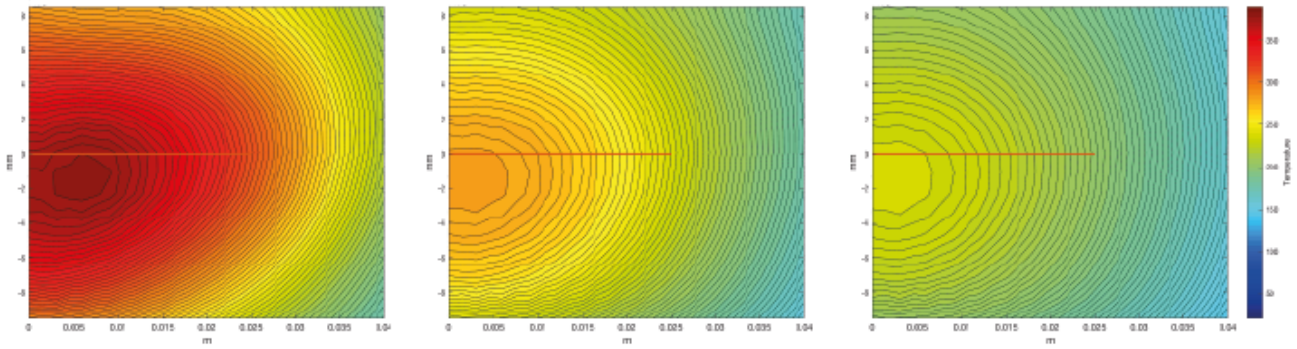

Figure 4.20: Cooling pattern after induction welding 36 seconds and after 56 and 76 seconds with KVE4 heatsink and 390 degree maximum temperature

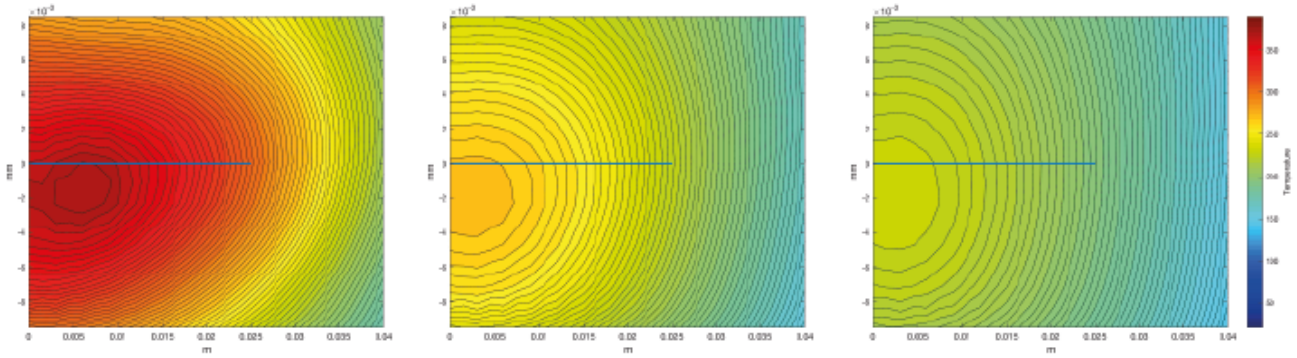

Figure 4.21: Cooling pattern after induction welding 36 seconds and after 56 and 76 seconds with KVE4 heatsink with the most conducting direction traverse to the coil and 390 degree maximum temperature

4.3. WELDING EXPERIMENTS

To validate the model induction welding experiments with two different heatsinks and different welding time have been conducted. The main focus of the experiments is aimed towards the cooling of the plates. First the KVE3 heatsink is discussed, fast cooling rates are suspected based on the computational data. The next set of experiments is conducted with the KVE4 heatsink and should result in lower cooling rates. For all experiments the 7 thermocouples were place at different locations to monitor the temperature. The location of the thermocouples are shown by the red dots in figure 4.22. The figures illustrates two plates and their overlap. The picture also provides an insight into the temperature distribution through out the plate. One can clearly see the cooling quality of the heatsink at location TC3. Table 4.2 lists the location of the different thermocouples and their abbreviation. The aim of the experiments was to reach 380 degree at the weld interfaced, to predict the desired ampere three experiments where conducted at different temperature, one at a temperature below the glass transition temperatures and two below the melting temperature. With the data of these experiments and a power curve the desired ampere was calculated. It is important to bear in mind that the thermocouple place between the plates will slightly change the lower plate distance to the coil and as described in section 1.1.4 this will influence the power. Secondly the reader should keep in mind there is error associated with the thermocouple temperature, which is enhanced by the magnetic field. This can be seen clearly in figure 4.35, the moment the magnetic field in on, there is a drop in the signal of all thermocouples (at 80 seconds). This will influence the precision of the results.

Table 4.2: Abbreviation thermocouple and location

Abbreviation	Location thermocouple
Tc1	Thermocouple at weldinterface
Tc2	Thermocouple at silicone
Tc3	Thermocouple at heatsink
Tc4	Thermocouple next to heatsink
Tc5	Thermocouple next to overlap'
Tc6	Thermocouple at edge high
Tc7	Thermocouple at edge low

4.3.1. KVE3 HEATSINK

Three experiments with different welding times of 17, 22 and 34 seconds have been tested. First the maximum temperature of seven thermocouples are compared between the simulation and experiments. Then the focus will be on the cooling tarjectory of the thermocouple at the weld line and the corresponding cooling rate. A overview of the temperature logged by the different thermocouple is provided in figure 4.23. Thermocouple at the lower edge malfunctioned as can be seen in the graph.

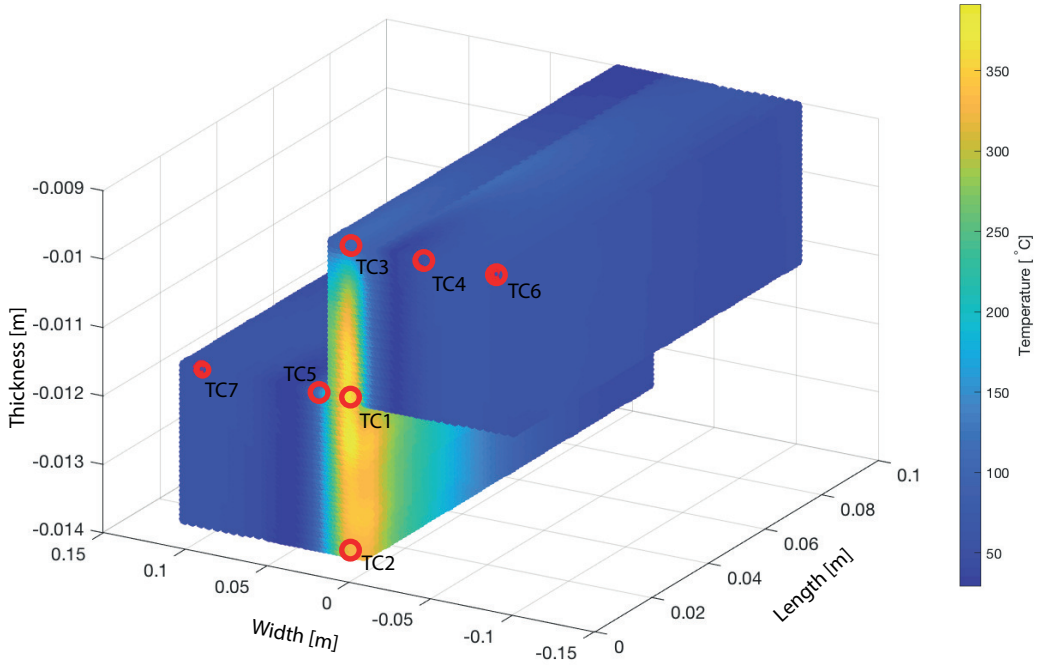

Figure 4.22: Location of thermocouples at the plates indicated by red circles

MAXIMUM TEMPERATURE

Table 4.3 list the temperature reached during the welding experiments and the temperatures predicted by the FEM model. Comparing the maximum temperature form the experiments with the temperature predicted by the simulations for the different welding times. Although the prediction of the maximum temperatures is at the weld interface are within a 10 % bound, the other prediction start to deviate form the experiments. For the thermocouples 4 and higher, not located under the coil, the temperatures of the experiments are higher compared to the simulations. This indicates that there is a different temperature gradient between the simulations and the experiments which would result in a different cooling trajectory and cooling rates. As the heat flows from the highest points towards the lower points and the difference will determine the cooling rate. The difference between TC2, TC3 and the other thermocouples could indicate that the thermal conductivity within the ply is to low which will result in a over prediction of the temperature at the centre of the coil. The heat flows to slow to the edges which will result in an under predicting the thermocouples located at the edges.

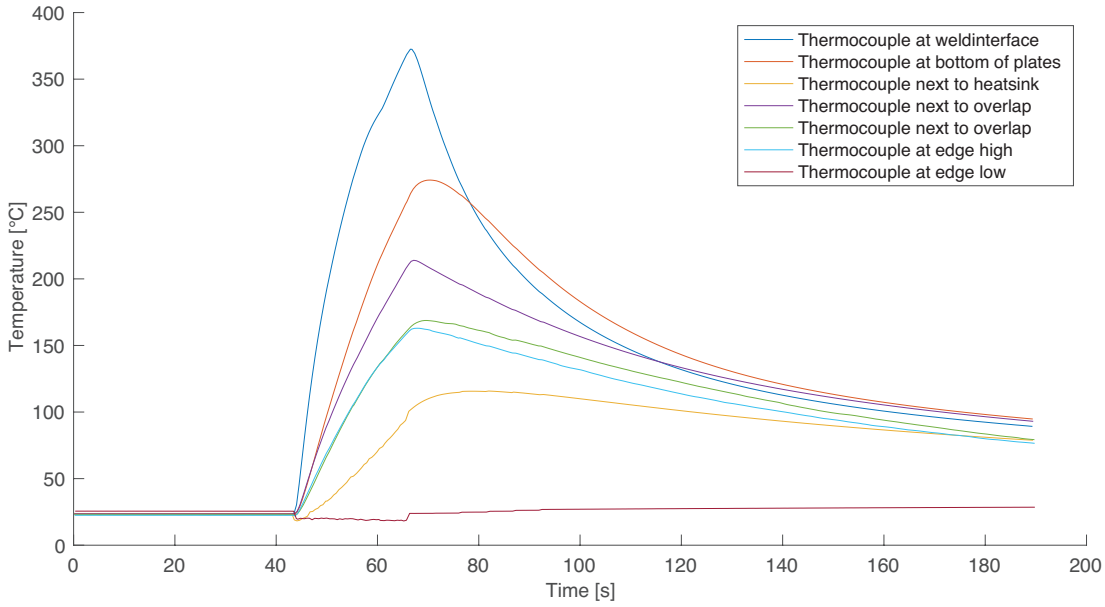

Figure 4.23: The cooling trajectory of the different thermocouples when welding 22 seconds

COOLING TRAJECTORY AND COOLING RATE

Since the objective of this research is to predict the crystallinity at the weld interface we will now focus on the thermocouple at the weld interface. Figure 4.24 illustrates the two different cooling trajectories of the three different welding times. The blue lines illustrate the computationally determined cooling trajectory and the orange line the experimental cooling trajectory. Figure 4.24b captures the difference the best, the same maximum temperature is reached but the trajectories start to deviate. This already happens before the region in which crystallinity forms.

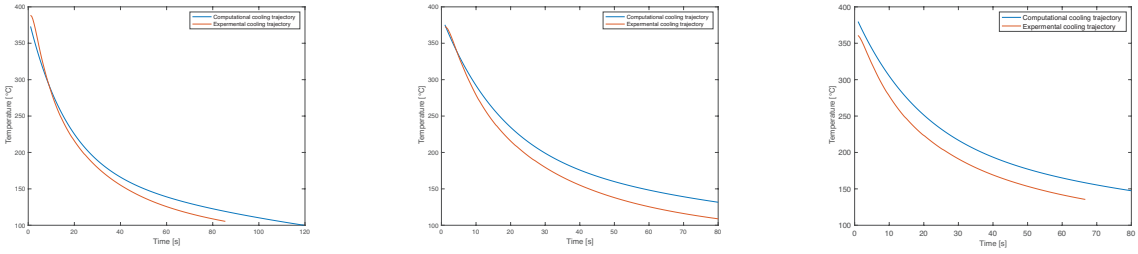

(a) Cooling trajectory after welding 17 seconds

(b) Cooling trajectory after welding 22 seconds

(c) Cooling trajectory after welding 34 seconds

Figure 4.24: Cooling trajectory for different welding times

[5]Thermocouple died during experiment
[6]Thermocouple not present in heatsink
[7]Thermocouple moved under the weld overlap during welding

If the cooling trajectory for welding of 22 seconds is translated to a cooling rate at each temperature the difference becomes more clear. This is illustrated in figure 4.25a. There is a little bit of noise produced by the thermocouple, which can be ignored by the reader. More interesting is the much faster cooling rates than predicted. The KVE3 heatsink already produced high cooling rates which where often above the threshold cooling rate of 140 °C/min as mentioned in section 2.1. The simulations predict that welding for 34 seconds with KVE3 heatsink will result in cooling rates below the threshold of 140 °C/min. Figure 4.24c shows a slightly lower maximum temperature for the experiments which will results in a faster cooling during the crystallization region. This and the faster cooling compared to the simulations will result in cooling rates above the threshold value as can been seen in figure 4.25b. The ripple in the line are introduce by the magnetic field creating noise at the thermocouples.

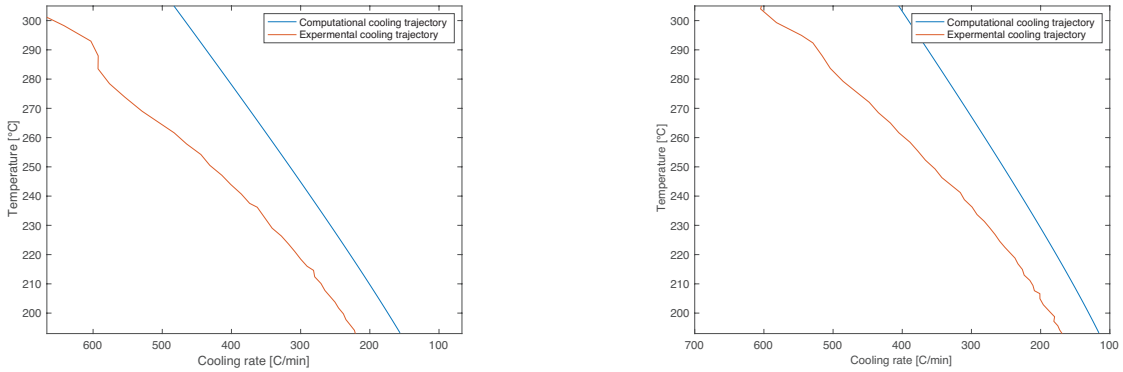

(a) The cooling trajectory of the different thermocouples when welding 22 seconds

(b) The cooling trajectory of the different thermocouples when welding 34 seconds

Figure 4.25: Cooling rates for different welding times

As suspected from the simulations, the excellent thermal properties of the KVE3 heatsink will result in high cooling rates at the weld interface. These high cooling rates will hinder the formation of crystalline regions at the weld interface.

4.3.2. KVE4 HEATSINK

The prediction of the simulations showed more promising results for the KVE4 heatsink in terms of the cooling rates. For this reason the number different welding times tested was increased to five different welding times: 17, 22, 27, 30 and 34 seconds. The locations of the Thermocouples are kept the same except the thermocouple located next to the heatsink (Tc4), which is moved towards the edge by 1 cm, due to the large width of the KVE4 heatsink. The KVE4 heatsink can be damaged as result of overheating, so extra care is taken to prevent damaging the heatsink.

MAXIMUM TEMPERATURE

Table 4.4 lists the temperature reached during the welding experiments and the temperatures predicted by the FEM model. Comparing the maximum temperature form the

experiments with the temperature predicted by the simulations for the different welding times. Just as observed with the KVE3 heatsink the temperatures at the weld interface are within a 10 % bound. Whereas the thermocouples located further from the overlap have larger deviations between the simulations and experiments. If we compare thermocouple TC2 for both heatsinks we see a higher temperature for the KVE3 heatsink which indicates that maximum through the thickness temperature is located in the bottom plate as seen in section 4.2.1. Whereas the maximum through the thickness temperature for the KVE4 heatsink is located at the top plate. This illustrates the cooling capability of both heatsinks.

COOLING TRAJECTORY AND COOLING RATE

All cooling trajectories and cooling rates can be found in appendix A.2. In this section the welding times 17 seconds, 27 and 34 seconds are highlighted. Figure 4.26 illustrates the cooling of the three different welding times. Comparing the deviation between the experiments and simulation for the welding with KVE3 heatsink (figure 4.24) and the KVE4 heatsink (4.26), we find a larger deviation for the KVE4 heatsink.

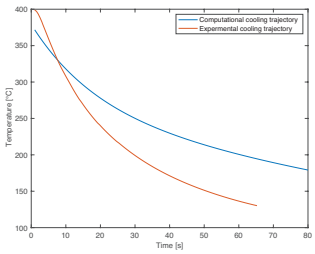

(a) Cooling trajectory after welding 17 seconds

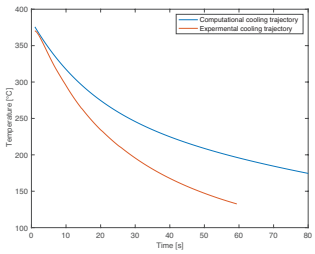

(b) Cooling trajectory after welding 22 seconds

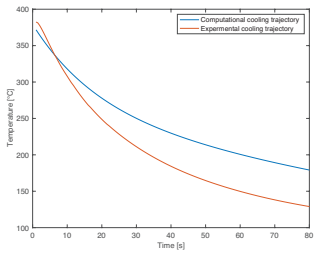

(c) Cooling trajectory after welding 34 seconds

Figure 4.26: Cooling trajectory for different welding times

Translating the cooling trajectory to the cooling rate, the deviation should become clear. This can be observed in figure 4.27. Welding for 34 seconds should result in the slowest cooling rates, which is verified but the weld interface still cools at rates above the threshold of 140 °C/min. An overview of the effect of welding time on the cooling rate is shown in figure 4.28. The trend is the same as observed in the simulations, but even longer welding times are desired to at least reach the threshold value.

The observation that the experiments do not reach the threshold value forces to extend the research, to ensure the cooling rate is reduced during dynamic welding. The moving coil will result in a more even heat distribution and more energy is add to the workpiece a coil moving reducing the cooling rate of the weld interface. Not reaching the threshold value also prevents validation of the analytical model.

4.4. DYNAMIC EXPERIMENTS

During dynamic welding the total amount of energy introduced to the plates it higher and the moving coil causes a heat source which influence the cooling of a specific point

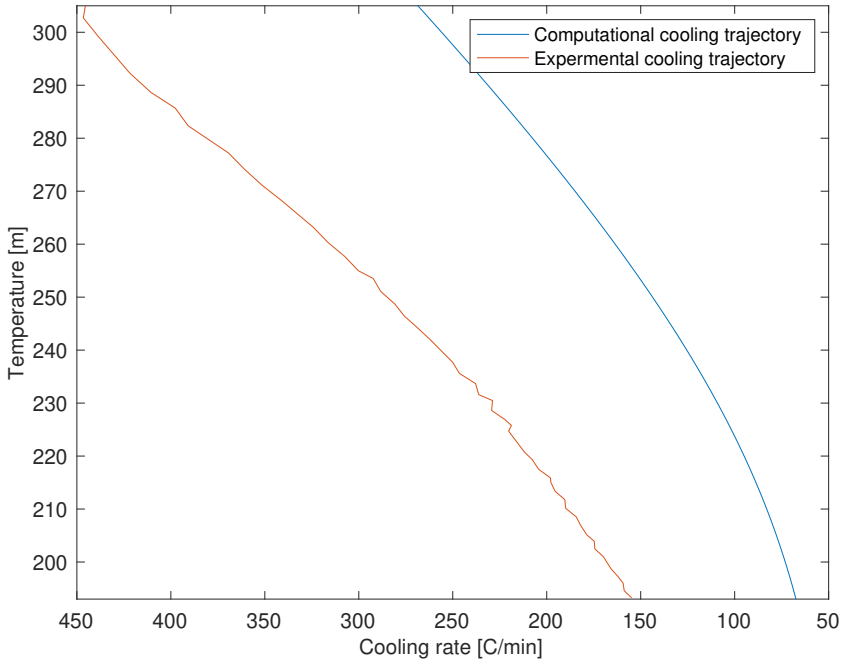

Figure 4.27: Cooling rates for welding 34 seconds with KVE4 heatsink

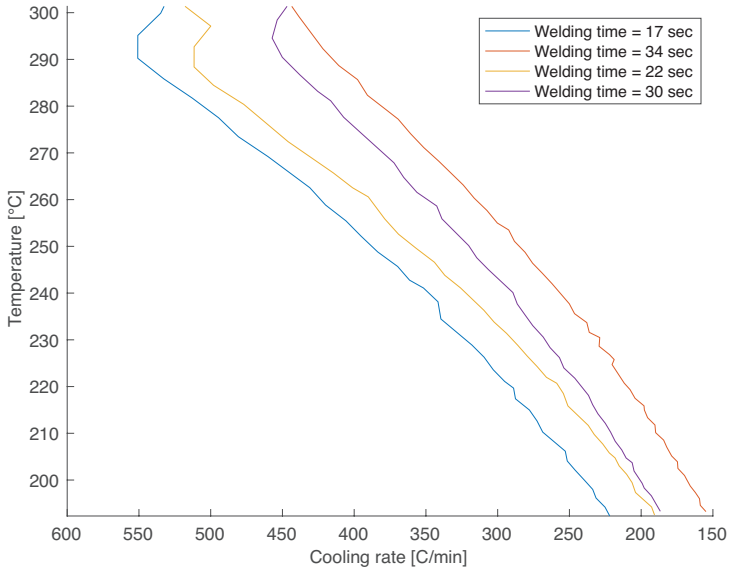

Figure 4.28: Cooling rates for welding 34 seconds with KVE4 heatsink

after is passed this point. These phenomena will most likely decrease the cooling rate at the weld interface. The dynamic experiments are conducted with both heatsinks. The current was adjusted to try to reach a maximum temperature of ± 380 °C. For the KVE4 heatsink two different coil speeds have been used, a slow coil speed of 7.62 cm/min[1] and a fast coil speed of 20 cm/min. For the KVE3 heatsink only the slower coil speed is

[1]Robot is only able to process integer input or inch/min input. 7.62 cm/min is consistent with 3 inch/min.

tested 7.62 cm/min. The reason for only conducting the slower coil speed for the KVE3 heatsink, is that this configuration is most likely to show crystallinity and this would result in the highest degree of crystallinity. The dwell time (the time the coil is on but not moving: the program starts and ends with a dwell) is kept constant at 5 seconds. To reach the desired welding temperature 3 experiments at lower current have been conducted to construct a power curve and calculate the desired current for a weld at ± 380 °C. The locations of the thermocouples at the plates can be found in appendix **??**. The thermocouples located at the weld line are number 1 until 6 and the coil will move from 1 towards 6.

4.4.1. KVE 3 HEATSINK

7.62 CM/MIN

To compensate for excellent thermal properties of the KVE3 heatsink a slow coil speed is advised to maximize the crystallinity at the weld interface. An overview of the temperature of all thermocouples is provided in figure 4.29 the maximum temperature is lower than the aimed 380 °C. The power curve to determine the required current resulted in a 354 °C. This data point was added to the curve and a fourth experiment was conducted. At 354 °C the interface is in molten state and the two parts will bond. This will influence the heating behaviour in the next experiments. The physics change, as the parts have become one and the pressure applied will result in a displacement of the carbon fibre which can result in direct contact altering the heating mechanism. As a result the fourth experiment also did not reach the desired temperature. A fifth experiment resulted in displacement of the thermocouples at the weld interface, as a consequences this experiment had to be discarded. The data of the fourth experiment will be analysed in the next section.

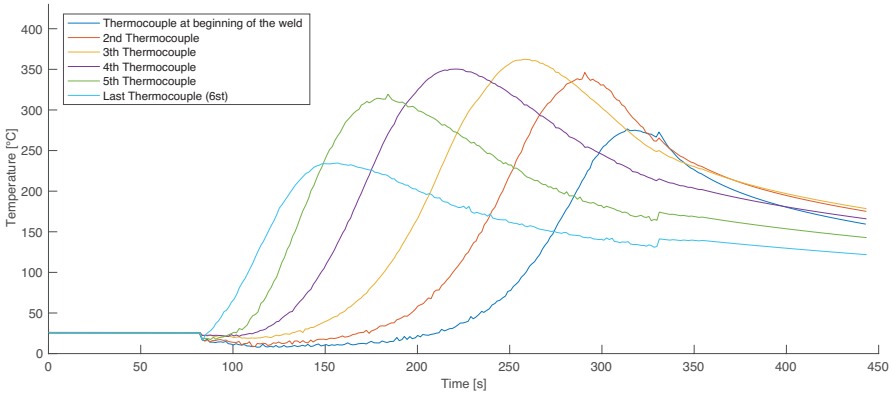

Figure 4.29

Two thermocouple have reached the temperature of 350 °C, thermocouple 3 at 363 °C and thermocouple 4 at 351 °C. If we investigated the cooling rate shown in figure 4.30, the figures show cooling rates which are much lower than suspected on basis of the static welding configuration and the simulations. The KVE 3 heatsink is compiled out of segments of 50x50x4 mm which can be added together to match the length of the plates,

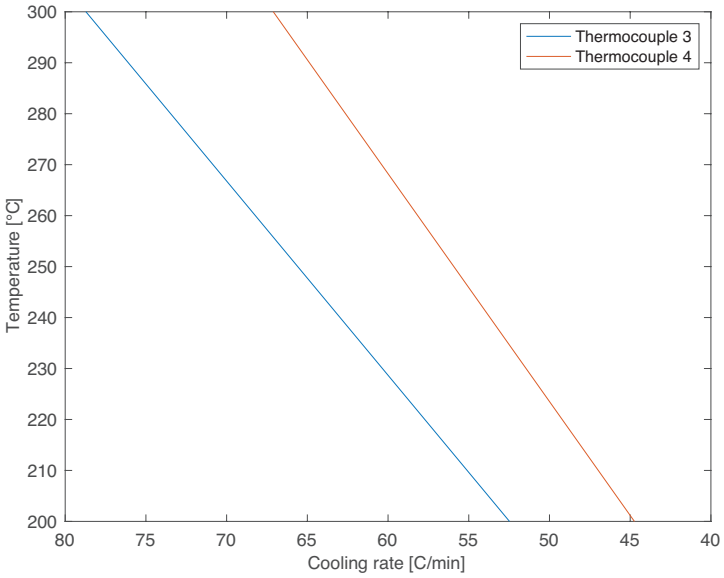

Figure 4.30: Cooling rate of the thermocouples at the weld interface

300x50x4 mm. During welding the heatsink could fill up with heat losing some of it's cooling capability. Another reason is the lower maximum temperature which will result in slower cooling rates. An effect of a lower maximum temperature will be a lesser degree of diffusion between both plates, as the time spent in molten state and the motion of the chains will be less, resulting less diffusion across the weld interface. An other interesting part of the figure is the drop in the temperature around 75 seconds, this is is due to the magnetic field which is produced by turning on the coil. As the coil passes the last thermocouple around 345 seconds there is a rise in the signal, this is when the coil is turned off, the the magnetic field is removed. This clearly indicates that the magnetic field will interfere with E-type thermocouple used. The E-type will measure mV and the magnetic field is capable to produce a couple of mV noise. This can affect the results, but the extent of the effect is not well known. Comparing the measurement from the thermocouple to physical properties of the material (Glass transitions temperature and Melting temperature), the results where in reasonable agreement.

4.4.2. KVE 4 HEATSINK

Now we move on to the welding with KVE4 heatsink. Again special attention is given to preventing overheating the heatsink.

20 CM/MIN

Looking at the overview of heating results for all thermocouples (figure 4.31) one can see the moment the coil is on, marked by the drop around 70 seconds. The magnetic field produced by the coil will introduce noise on your thermocouple data. The dynamic weld is not optimized yet which can be seen from the difference between the thermocouple maximum peaks. This difference can be reduced by longer dwell times and varying the coil speed at the first regions. Thermocouple 3 and 4 reach 350 °C and at this temperature

all prior crystallinity will be melted leading to a is completely amorphous polymer. Since the prior thermal history of the composites is unknown, removing all prior crystallinity is required to make predictions about the degree of crystallinity within the model. For this reason the focus will be on the Thermocouples reaching this temperature.

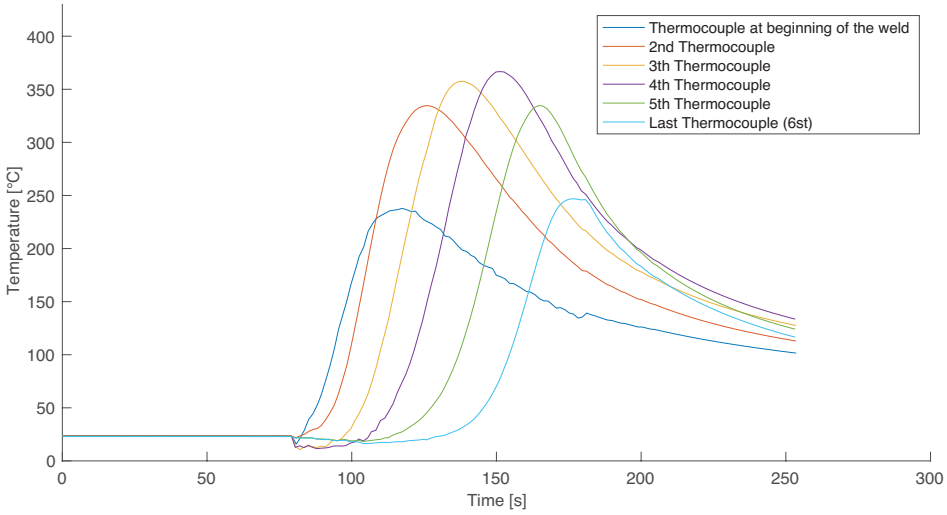

Figure 4.31: Overview of thermocouples located at the weld

Translating the temperature to the cooling rate at each temperature for the thermocouples of interest is shown in figure 4.32. The most interesting aspect of this graph is the lower right corner as only this region is cooled sufficiently slow, indicating low amounts of crystallinity at the weld interface.

7.62 CM/MIN

Figure 4.33 provides summary of all thermocouples at the weld interface. If we compare the 20 cm/min and 7.62 cm/min plots there are two main difference between them. The first is the difference between the peak temperatures, which becomes less as the coil distance is reduced resulting in a more consistent weld quality. The second and most important difference is the width of the peaks. The width clearly increases with slower coil speed, the larger width of the peaks is a first indication that the cooling rates is reduced. This can also be seen in figure 4.34 which illustrates the cooling rates from the active thermocouples. The figure clearly shows the effect of slower welding on the cooling rate. The cooling rate is greatly decreased for thermocouple 4 compared with thermocouple 4 of 20 cm/min coil speed.

The slower coil speed results in cooling rates and crystallinity which are of sufficient level that the crystallinity can be measured by DSC experiments. This is required to validate the analytic crystallinity model.

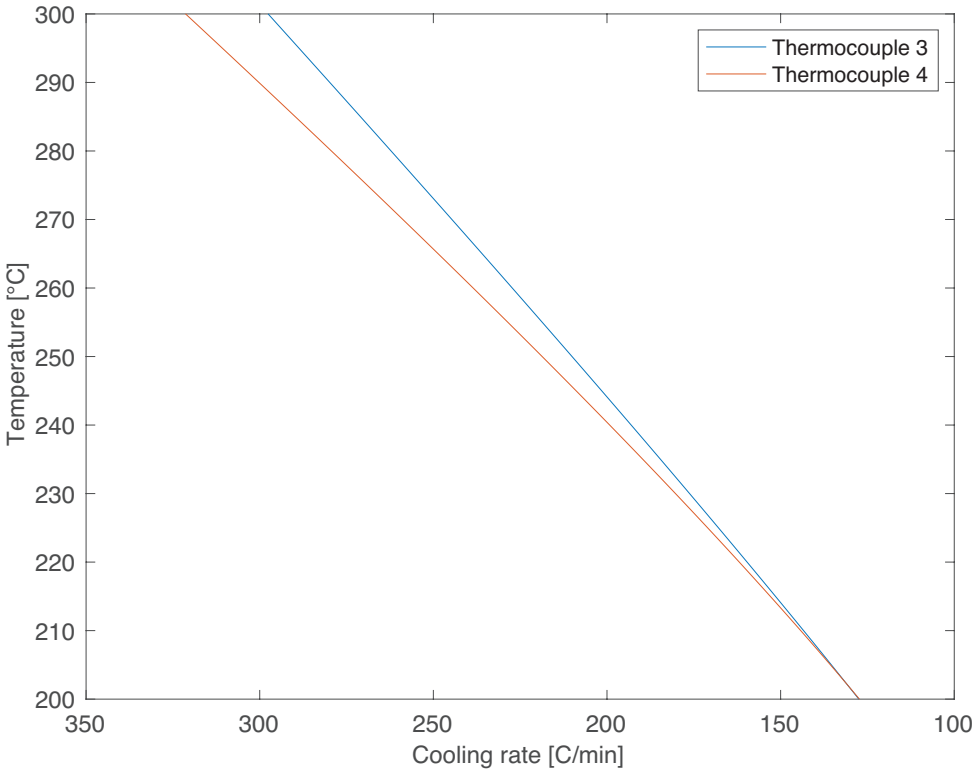

Figure 4.32: Overview of thermocouples located at the weld

4.5. QUASI-DYNAMIC SIMULATIONS

Although static simulations are crucial for understanding the influence of parameters on the induction welding process, the effect of the parameters on the cooling trajectory are straightforward for the static welding configuration. The only parameters influencing the cooling are the heatsink and the welding time. Simulating quasi-dynamic welding configurations extends the complexity of the process, especially when interested in the cooling trajectory. In comparison to the static simulations, in quasi-dynamic simulations there will be an added influence of the magnetic field of the coil moving away and the heat from weld spot influencing the cooling. The speed of the coil will be an extra parameter influencing the welding process. For the quasi-dynamic simulations the design is composed of two variables: the current supplied to the coil and the moving speed of the coil. The current of the coil will range from 300 to 650 A, where 650 ampere is close to the limitations of the coil. The coil speed will vary from 5 mm/min used for welding composites equipped with lighting strike protection and 30 mm/min as it is the fasted welding speed used by KVE. The simulations will be Executed with 2 different heatsinks, KVE3 and KVE4 heatsinks.

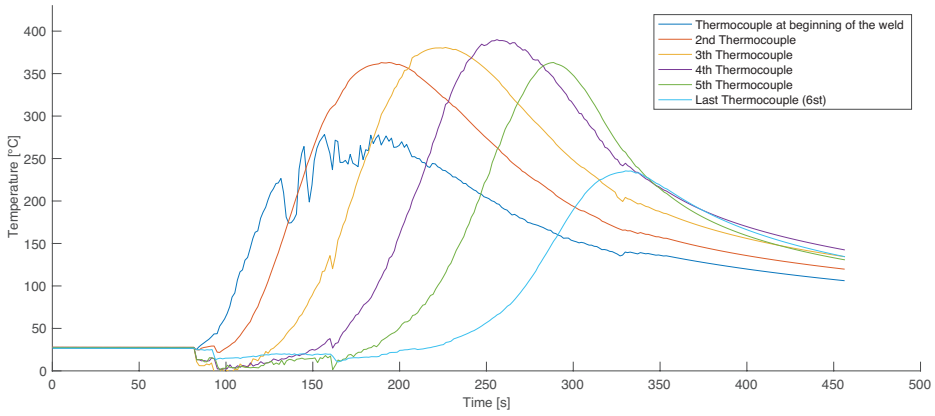

Figure 4.33: Overview of thermocouples located at the weld

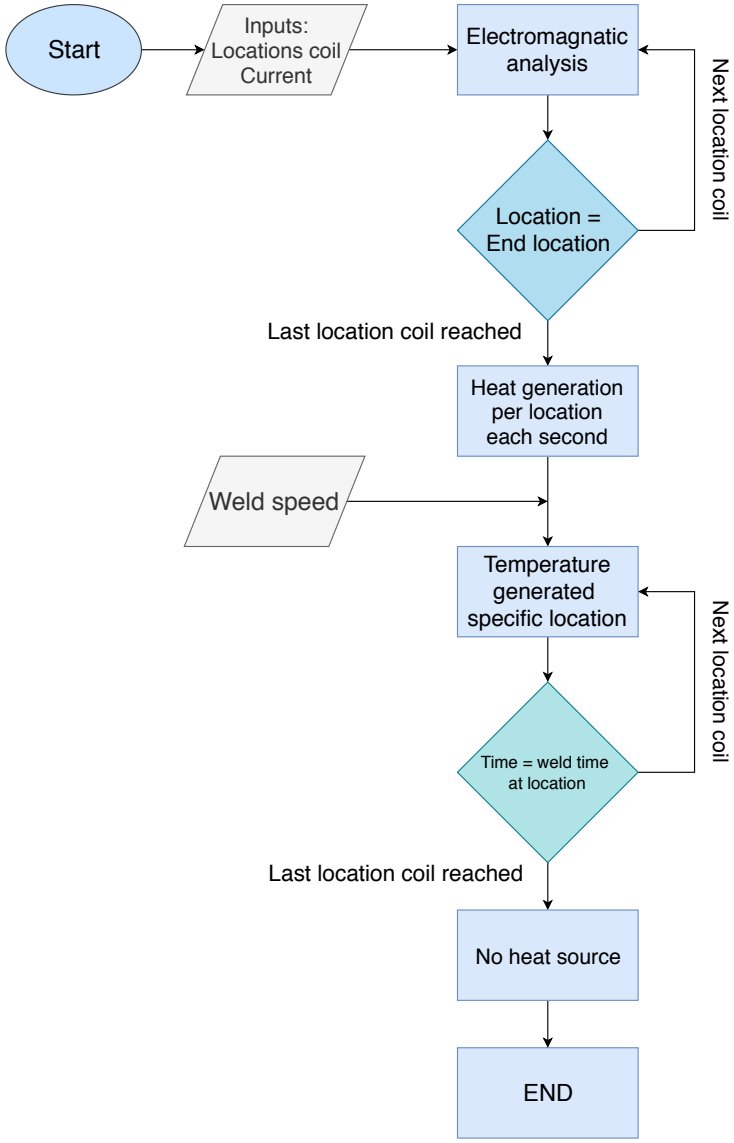

Figure 4.35: Flowchart of dynamic induction welding

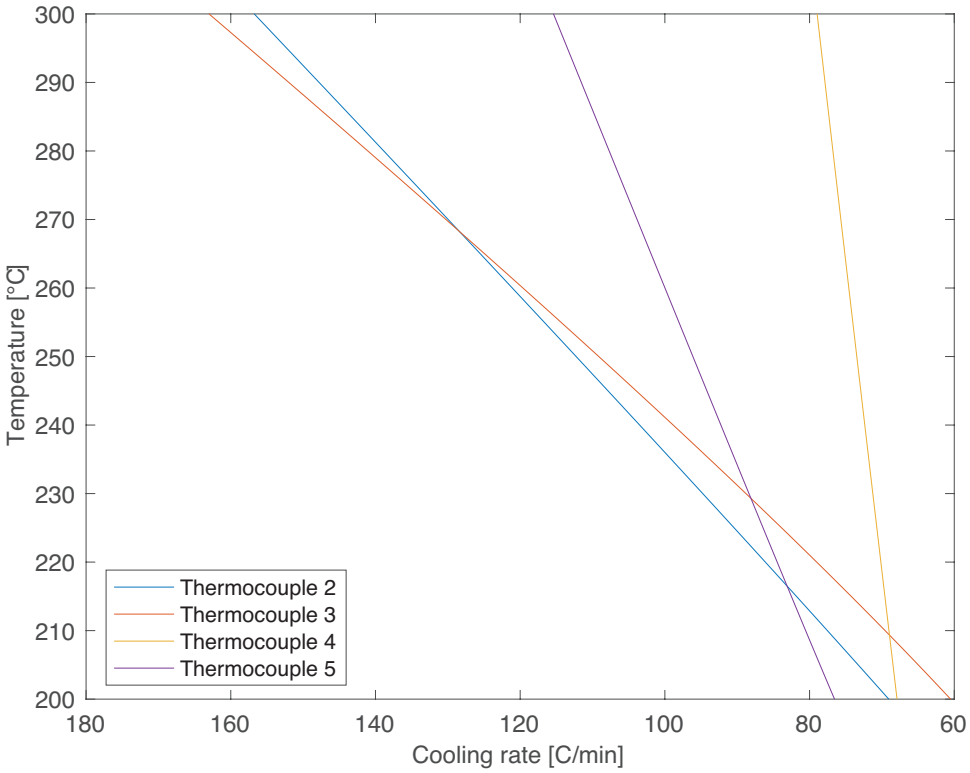

Figure 4.34: Overview of thermocouples located at the weld

4.6. QUASI-DYNAMIC SET UP

The quasi-dynamic computational model is based on the flowchart illustrated in figure 4.35. The model starts by defining the geometry and meshing the geometry with the coil at different locations. The input parameters, material properties, applied boundary condition and element types are assigned to the data points generated by the meshing. The applied current is generated by the Sobol sequence [129] . From there on the harmonic Electromagnetic (EM) analysis is started looping over all the different positions of the coil. This will result in an assigned heat generation for each node and for each location of the coil. The Electromagnetic analysis is time independent, and the heat generation from one magnetic simulation could be used for multiple thermal simulations with different coil speeds. So the input weld speed will determine the temperature developed from the EM. As the time at one location is reached, the next thermal analysis will start until the last location is reached. If the last location is reached, ANSYS will proceed to monitor the temperature development for 90 seconds. A disadvantage of the dynamic model is the additional computational time compared to the static simulations, because symmetry is lost and multiple magnetic steps are computed. For the static simulations the desired weld interface temperature was reached by computing two simulations with arbitrary currents, the relation between both is used to find the matching current for the desired temperature. The computational cost for the dynamic simulations are a lot higher and this method is not economic. To find the relation between current and weld-

ing speed a design space is constructed by the sobol sequence for all two heatsinks. The model is labelled as a quasi-dynamic model due to the discreet locations of the coil, which can be compared to the frames composing a film. A limited number of frames will result in a lagging film, increasing the number of frames will result in a more smooth film which is a closer approximation of real life motion. The same is true for the number of coil locations, increasing the number of locations will result in a closer approximation of a moving coil. However this will drastically increase the computational time of the model. The goal of this quasi-dynamic simulations is to show the capability of the analytical model to translate the simulations to a prediction of the crystallinity at the weld interface. The reader should keep in mind that the cooling rate is over predicted by the static model and this is bound to happen for the quasi-dynamic model. But this would be the first step in extending the model to a quasi-dynamic model and including the analytic crystallinity model. The simulation are computational intensive and take between 3 or 4 and a half day to complete depending on the coil speed. This does not guarantee the desired temperature of 380 degree, to reach this temperature multiple simulations are required. The next step of the quasi-dynamic model would be optimizing the coil speed across the the weld line to ensure a constant temperature at the weld interface. This will cost considerable computational time and is left outside the scope of this research. For future research the optimization is recommanded, as is will enhance the knowledge about evolution of crystallinity across the weld interface. The simulation will be use to illustrate the capabilities and the advantages of dynamic simulations for understanding the process. The second major advantages is the capability to observe the temperature trends through out the complete workpiece. This helps evaluating the data gathered during the experiments.

4.6.1. KVE3 HEATSINK

The static simulations of KVE3 heatsink showed the capability of the heatsink to prevent thermal degradation, but this resulted in high cooling rates which could result in an amorphous structure at the interface. Within the quasi-dynamic simulations, the relation between coil speed (weld speed) and crystallinity is explored. With the goal to identify the effect of welding speed on the crystallinity at the weld. Figure 4.36 displays the relation between current and coil speed to reach a maximum temperature at the weld interface. There is a linear relation between coil speed and current. This relations is also reported by [130].

QUASI-DYNAMIC SIMULATIONS WITH KVE3 HEATSINK

The design of experiments is applied to find experiments with its temperature within the processing range of 350 °C and 400 °C for the two coil speeds introduced in section 4.4.1, 7.62 cm/min and 20 cm/min. These experiments will be discussed in the following section. Figure 4.37 illustrates the locations of thermocouples used during the experiments and the volume of the specimens obtained by waterjet cutting.

20 cm/min

Figure 4.38 illustrates the temperature of the nodes illustrated in figure 4.37 for the KVE3

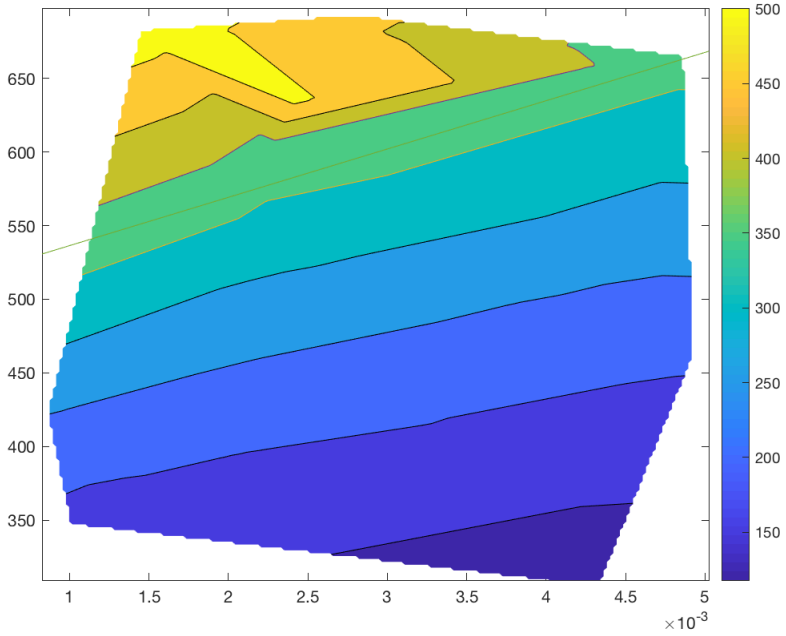

Figure 4.36: Design of Experiments for the KVE3 heatsink

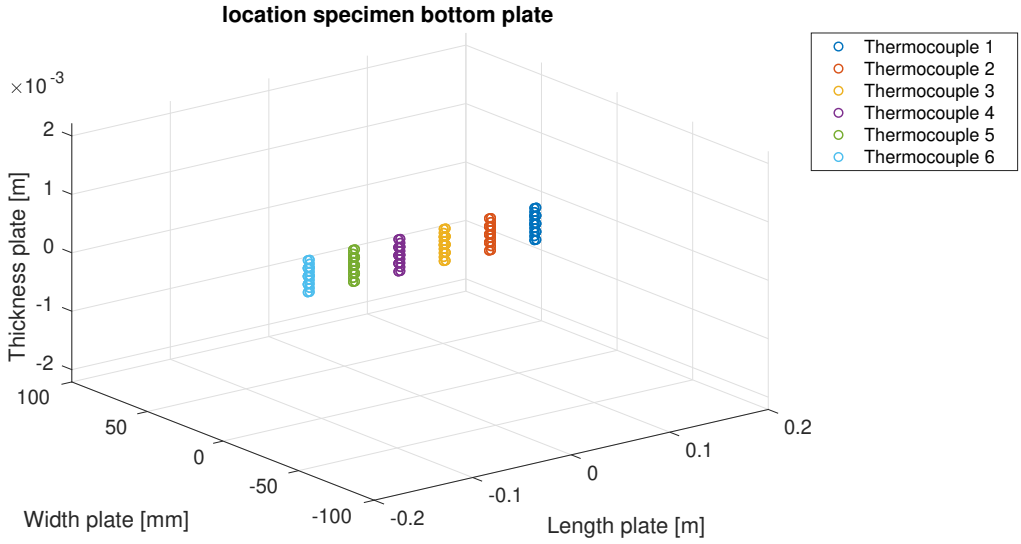

Figure 4.37: Locations of the nodes related to the thermocouples used during the experiments in section 4.4.1

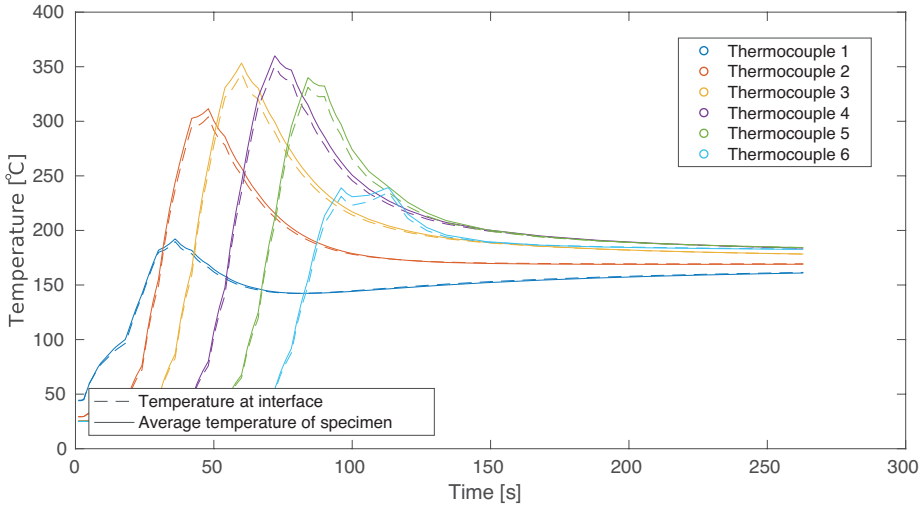

Figure 4.38: Temperature of the thermocouples and the average temperature of the DSC specimen for a coil speed of 20 cm/min applying the KVE3 heatsink

heatsink with a coil speed of 20 cm/min. One directly distinguishes the frame like nature of the quasi-dynamic simulations in the sharp transitions in the temperature. Because there where no experiments conducted for the slower coil speed, only the computational results will be discussed. In contrast to the other simulations which will directly be compared to the experiments. An interesting observation form the figure is that the first thermocouple will start to heat up again after it has started cooling. This is observation is not found during any of the experiment and this is consisted with the sluggish cooling observed during the comparison between the static simulations and experiments in section 4.3.2. An other observation is that average temperature of the specimen is large than the temperature at the interface. As heat within the material flows from its highest point to its lowest point, the cooling rates of specimen located further away form the interface will cool faster at the same moment. But will reach a lower cooling rate at a higher temperature resulting more crystallinity formed. The last observation, concerns the end of the cooling trajectory which becomes almost constant. the surrounding air is modelled to be room temperature and one should suspect an overal cooling of all the thermocouple. The absence of this cooling indicates that the influence of air on the model is underestimated.

7.62 cm/min

The quasi dynamic experiments will directly be compared to the experiments conducted in section 4.4.1. An interesting finding of these experiments was the finding of a lower cooling rates for the KVE3 heatsink in comparison to the KVE4 heatsink. This is noteworthy due to the fact that the KVE4 heatsink has an order 5 lower thermal conductivity compared to the KVE3 heatsink and that during the static experiments the KVE3 heatsink resulted in faster cooling rates. However the KVE4 heatsink has a larger body and the effect of this larger body becomes more pronounced during dynamic welding.

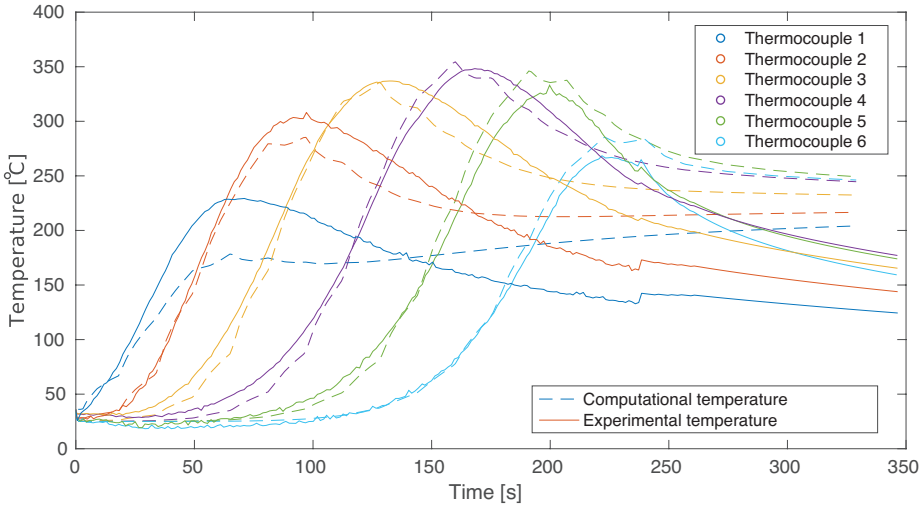

Figure 4.39: Temperature of the thermocouples and the average temperature of the DSC specimen for a coil speed of 7.62 cm/min applying the KVE3 heatsink

The heatsink can absorb more heat within its larger body, making it capable to cool more efficient for a longer period while the KVE4 heatsink will fill up with heat more rapidly reducing the cooling efficiency of the heatsink. Figure 4.39 illustrates the comparison between the simulations and experiments. The peaks in the figure are located at the same time period but first two peak underestimate the temperature while the last two peak overestimate the temperature. This is again due to the cooling of the composites heat stays located at the overlap region requiring less energy to heat the last section of the weld. This is in direct relationship with the ends of the cooling trajectories. The ends of experiments converge towards each other while there is a consistent cooling trend, for the simulations the first 3 thermocouples will start heating again after a cooling stage and the temperature will converge towards the last thermocouple while becoming almost constant.

4.6.2. QUASI-DYNAMIC SIMULATIONS WITH KVE4 HEATSINK

The static simulations of KVE4 heatsink showed the capability of the heatsink to prevent thermal degradation, but this resulted in high cooling rates which could result in an limited degree of crystallinity at the interface. Within the dynamic simulations, the relation between coil speed and crystallinity is explored. With the goal to identify the effect of welding speed on the crystallinity at the weld. The design of experiment for the KVE4 heatsink is shown in figure 4.40, and used to find the desired current to reach a temperature within the processing range.

20 cm/min

Figure 4.41 illustrates a comparison between the simulations and experiments for the coil speed 20 cm/min with the KVE4 heatsink. In general the same trends are observed as in section 4.6.1. An observation which is more distinguished for the KVE4 heatsink is the conversion temperatures towards each other. The experiments clearly converge faster

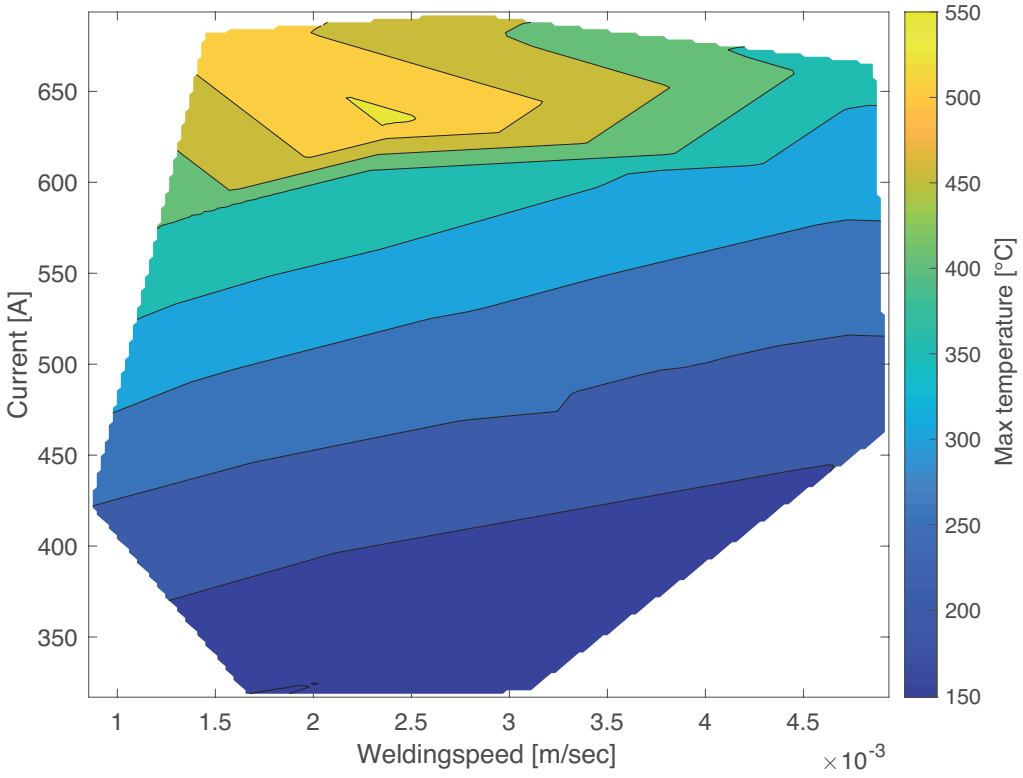

Figure 4.40: Design of Experiments

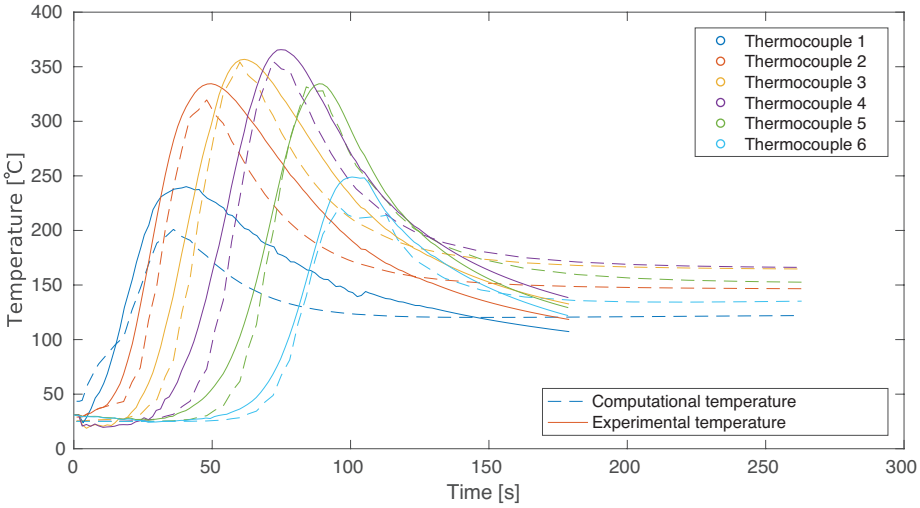

Figure 4.41: Temperature of the thermocouples and the average temperature of the DSC specimen for a coil speed of 20 cm/min applying the KVE3 heatsink

towards each other equalizing the temperature gradient over the weld interface. While the temperature of the thermocouples during the simulations become almost constant and not converge towards each other. This suggests that the thermal conductivity of the composite used during the simulations is to low. Increasing the thermal conductivity of the composite will also result in faster cooling of the composite. Which is one of the problems observed during the simulations. For the faster coil speed all thermocouples eventually cool below the temperature of 190 °C preventing any motion of the polymer chains and stopping crystallization.

7.62 cm/min

When we reduce the coil speed, as illustrated in figure 4.42 the indication for a incorrect thermal conductivity of the composites becomes more clear. There is a larger temperature difference between the themocouples and the temperature are monitored over a longer period of time. A larger temperature difference should result in a faster flow of heat of the two extremes towards each other resulting in temperature which converge as shown in the experiments. Longer time period allows the temperature gradient to blend more gradually. However this is not observed during the computations, the last couple of thermocouples do not even cool below the crystallization region. This will imply that the crystallization will continue for a much longer period compared to the experiments.

4.6.3. THROUGH THE THICKNESS TEMPERATURE

To see the effect of the heatsink and different coil speed on the temperature through the thickness of the plates at the centre of the overlap, the four different temperature gradients are compared in figure 4.43. At this moment the coil is located at thermocouple 4. The figure illustrates that the maximum temperature is within the lower plate and is lowered when the coil speed is reduced. The most interesting aspect of these contour plots concerns the temperature at the heatsink interface, which is located at the top of the fig-

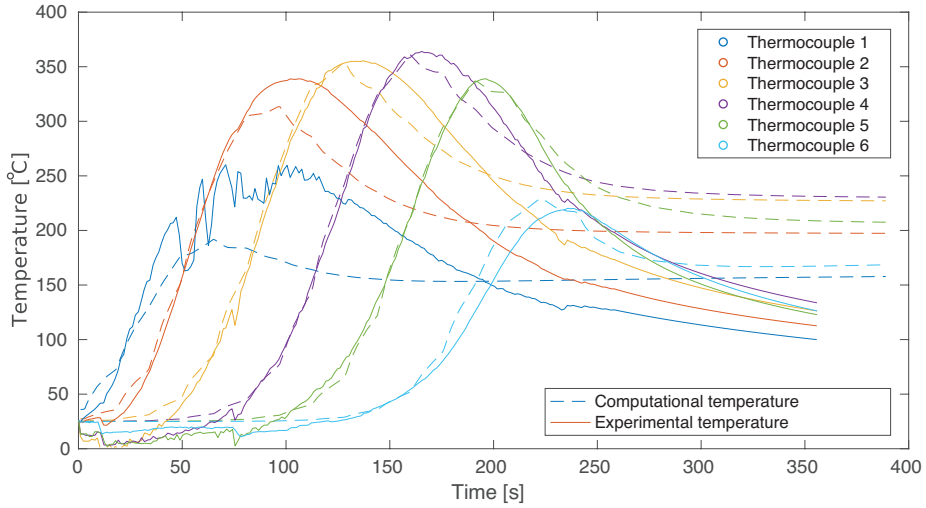

Figure 4.42: Temperature of the thermocouples and the average temperature of the DSC specimen for a coil speed of 7.62 cm/min applying the KVE4 heatsink

ure. The KVE3 heatsinks will result in a lower temperature at the region directly above the weld pool created by the coil. But the temperature at the heatsink interface further away from the weld pool the contrary is true and higher temperature are observed for the KVE3 heatsink. This would indicate that the small body of the KVE3 heatsink is sufficient to prevent degradation and melting of the top surface but will spread the heat across the overlap lowering the cooling rates within the composites by creating a more even temperature gradient within the material. The KVE3 heatsink with a coil speed of 7 cm/min reveals more indications that the KVE3 heatsink will distribute the heat across the heatsink interface. Looking at the two top corners we seen the contour lines bending towards the sides this means there is a higher temperature found at the interface compared to within the material. This is not observed for the KVE4 heatsink and indicates that heat must be applied from the top, so from the heatsink on top. It would be interesting to see how the temperature develops within the heatsink during the welding simulations. Further research should be undertaken to investigate the effect of the size of the heatsink and how the heatsinks interacts with the composites as it heats up.

4.7. CONCLUSION AND RECOMMENDATIONS

Different welding configuration, static and dynamic were investigated in order to find the effect of processing parameters on the temperature and the cooling rates of the UD CF-PEKK material. The experiment showed the importance of monitoring the cooling rate and showed deviating results for both the experiments ant he multi physic simulations. Based on these findings, the analytical model of the following section predict the crystallinity. The static experiment showed sufficiently high cooling rates which will suppress formation of crystalline regions. For this reason dynamic welding experiments were included, which experiments showed slower cooling rates. Validation showed the computational model, capable to predict the right relationships. The difference between

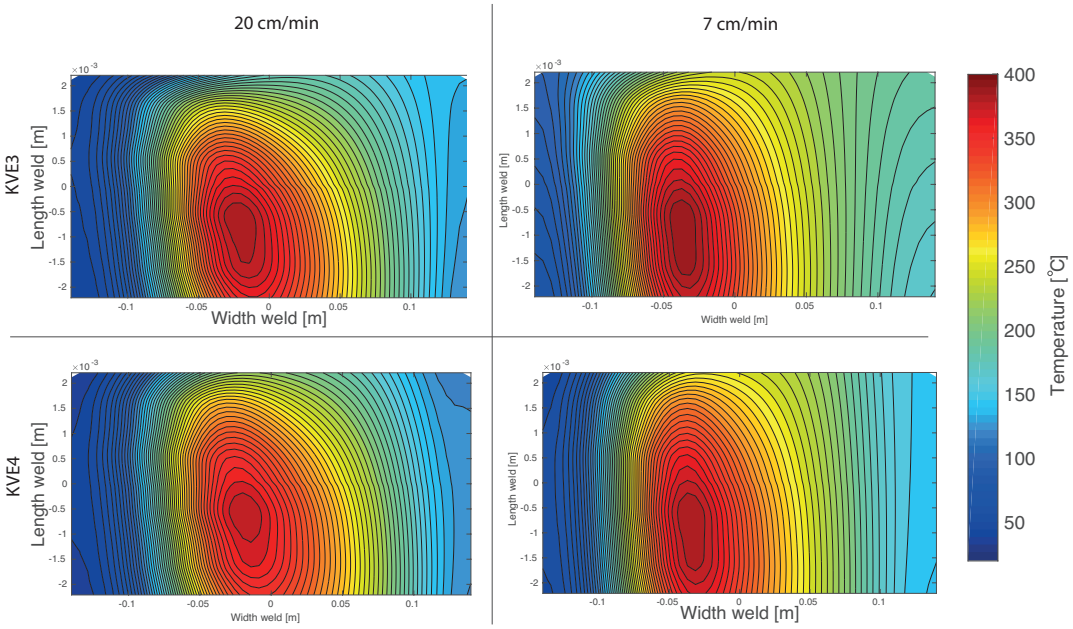

Figure 4.43: Four temperature gradients for the different welding configurations simulated with the coil located at thermocouple 4

thermocouple temperature showed that there is still room for improvement. One of the main points of attention is the cooling of the material. Next to that evaluating the results considering the cooling, the thermal properties could be improved and boundary conditions could be applied to increase the quality of the cooling predictions. Additional research focussed on the cooling of the material should be preformed. All in all , one is able to model the heating and cooling behaviour of UD-CF PEKK laminates. This will allow investigations of the crystallinity within the material, which is time and money consuming to do. However in order to have accurate temperature prediction upon cooling, a lot of work still remains.

Table 4.3: Maximum temperatures of experiments and computational simulation compared

Welding time 17 sec			
names	Computational temperature [°C]	experimental temperature [°C]	difference [%]
Tc1	365,87	388,43	-5,81
Tc2	364,85	270,09	35,08
Tc3	125,15	158,81	-21,19
Tc4	56,6	-	- [5]
Tc5	98,311	346,31	-71,61
Tc6	67,36	170,93	-60,59
Tc7	65,196	143,79	-54,66
Welding time 22 sec			
names	Computational temperature [°C]	experimental temperature [°C]	difference [%]
Tc1	369,48	372,50	-0,81
Tc2	378,1	274,20	37,89
Tc3	137,19	28,54 [6]	380,77
Tc4	60,492	115,78	-47,75
Tc5	110,36	213,95	-48,42
Tc6	71,893	168,76	-57,40
Tc7	69,525	162,93	-57,33
Welding time 34 sec			
names	Computational temperature [°C]	experimental temperature [°C]	difference [%]
Tc1	376,26	360,80	4,28
Tc2	397,28	281,14	41,31
Tc3	157,62	-[6]	-
Tc4	67,831	138,02	-50,85
Tc5	132,89	262,87 [7]	-49,45
Tc6	79,869	199,79	-60,02
Tc7	77,139	163,65	-52,86

Table 4.4: Maximum temperatures of experiments and computational simulation compared

Welding time 17 sec			
names	Computational temperature [°C]	experimental temperature [°C]	difference [%]
Tc1	367,22	398,84	-7,93
Tc2	346,45	269,77	28,42
Tc3	256,36	228,79	12,05
Tc4	52,248	113,84	-54,10
Tc5	88,955	248,16	-64,15
Tc6	61,85	150,75	-58,97
Tc7	59,917	140,87	-57,47
Welding time 22 sec			
names	Computational temperature [°C]	experimental temperature [°C]	difference [%]
Tc1	368,71	364,18	1,25
Tc2	356,02	248,42	43,32
Tc3	262,2	191,78	36,72
Tc4	54,643	100,73	-45,75
Tc5	97,917	230,32	-57,49
Tc6	64,571	158,94	-59,37
Tc7	62,51	138,97	-55,02
Welding time 27 sec			
names	Computational temperature [°C]	experimental temperature [°C]	difference [%]
Tc1	369,95	370,51	-0,15
Tc2	361,49	247,25	46,21
Tc3	266,5	178,57	49,25
Tc4	56,504	119,93	-52,88
Tc5	104,72	230,95	-54,66
Tc6	66,445	180,14	-63,12
Tc7	64,301	141,52	-54,56
Welding time 30 sec			
names	Computational temperature [°C]	experimental temperature [°C]	difference [%]
Tc1	362,42	363,99	-0,43
Tc2	357,81	259,17	38,06
Tc3	262,86	224,00	17,35
Tc4	56,29	110,81	-49,20
Tc5	106,51	236,49	-54,96
Tc6	66,137	164,57	-59,81
Tc7	63,989	131,43	-51,31
Welding time 34 sec			
names	Computational temperature [°C]	experimental temperature [°C]	difference [%]
Tc1	367,39	382,47	-3,94
Tc2	364,99	263,58	38,48
Tc3	269,45	218,41	23,37
Tc4	58,494	123,18	-52,52
Tc5	113,32	-	-
Tc6	68,461	180,15	-62,00
Tc7	66,213	150,76	-56,08

5

CRYSTALLIZATION KINETICS

Characterize the crystallization behaviour of CF/PEKK at a variety of different cooling rates, is the first step into finding out what the influence is of the cooling rate on the degree of crystallinity of the weld. By varying the cooling rate, one can get a clear view of the influence of cooling rate on the onset temperature, the rate of conversion and the degree of crystallinity. The experiments were kept under 400 °C to prevent thermal degradation of the PEKK. Tests where conducted on one specimen to guarantee a constant volume fiber fraction.

5.1. INDUCTION TIME

Prior the crystallization there is an induction period or induction time. For modelling of crystallization it is crucial to model the induction time. This induction time indicates when the crystallization model should become active. Godovsky [131] proposed an empirical model to predict the induction time in isothermal crystallization:

$$t_i = t_m (T_m^0 - T)^{-c} \tag{5.1}$$

Where t_i is the isothermal induction time and t_m and c are the parameters fitted to the experiments. DSC runs at 250, 255, 260, 265, 270 and 280 isothermal temperatures were conducted to find the induction times. The program will first cool at a high cooling rate to prevent prior crystallization to the desired isothermal temperature. Due to the change from high cooling rate to an isothermal run there will be a heat flow overshot in the measurements. In this region the DSC has to calibrate for the isothermal run. Due to the fast nucleation of PEKK part of the crystallization occurs during this calibration region. This phenomenon hides the precise nucleation point. To find the induction time the method applied by Choupin et al [67] is used.

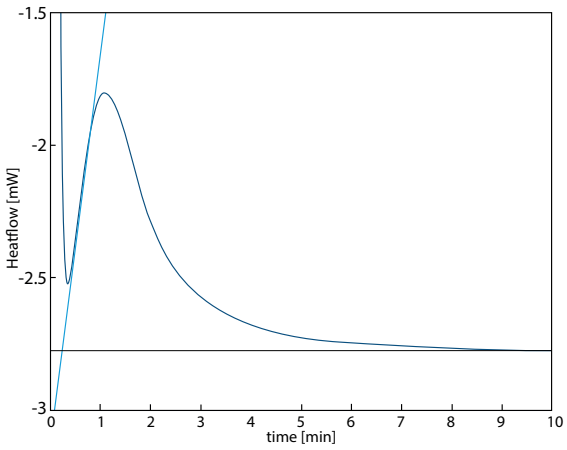

Figure 5.1: Method of determining the induction time

A tangent is drawn at the ramp of the crystallization peak. The intersect of the tangent with the baseline is indicated as the induction point, as illustrated in figure 5.1.

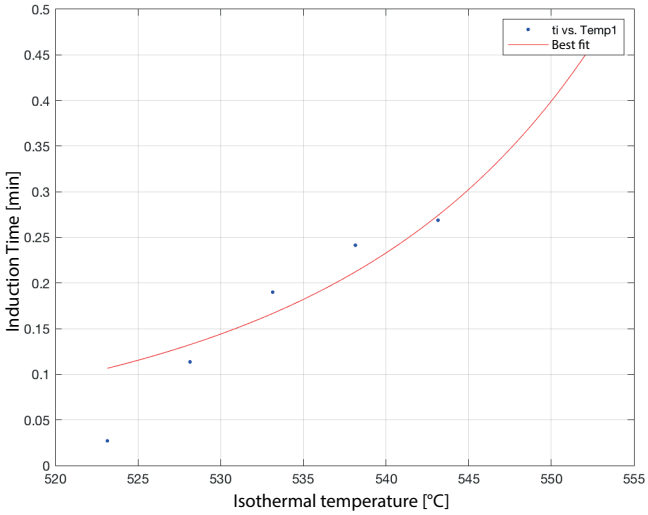

Figure 5.2: Isothermal temperature versus induction time

The variable of the best fit to the isothermal data for CF/PEKK

Table 5.1: Variables of best fit

	t_m	c
Cytec	1.021e+08	-4.448

Christian [132] stated that "the total time required to reach a specific amount of transformation, X_a ,is obtained by summing the fractions of time taken to reach this stage isothermally, until the sum reaches a value of one.". He called this the concept of additivity, which was aimed at the phase transitions of metals. Applying this concept to the

phase transition of crystalline polymers for PEEK was shown to be valid by Gordnian, Kamyar [133]. The induction time is taken as the point where $X_a = 0.001$ (sufficiently small degree but still measurable) and the mathematical expression for additivity is:

$$1 = \int_0^{t_1} \frac{dt}{t_i(T)} \tag{5.2}$$

Where $t_i(T)$ is the induction time for the isothermal conversion at the temperature T and t_i is the induction time for non-isothermal runs. Predicting the induction time of an arbitrary cooling rate, combining equation (5.1) along with equation (5.2) and the parameters from table 5.1 . In figure 5.3 the induction times derived by the model are compared to the experimentally determined induction times. The model could be applied for lower cooling rates with a small error but higher cooling rates are more critical. If the model predicts the induction time one minute later by a cooling rate of 40 °C/min this would mean the induction would start 40 °C later. A model which would predict induction on basis of a induction temperature would be more suited for predicting crystallization for an arbitrary cooling trajectory. The method assumes a starting temperature of 380 °C, although the starting temperature during experiments deviated from this temperature. To predict a correct indutiontime a correction should be included. Because the maximum temperature differs and the cooling rate is not constant the a induction time based on cooling rate will lead to errorous induction times. An induction temperature based on cooling rate will be much more practial. The next section will propose a method to relate the cooling rate to a induction temperature.

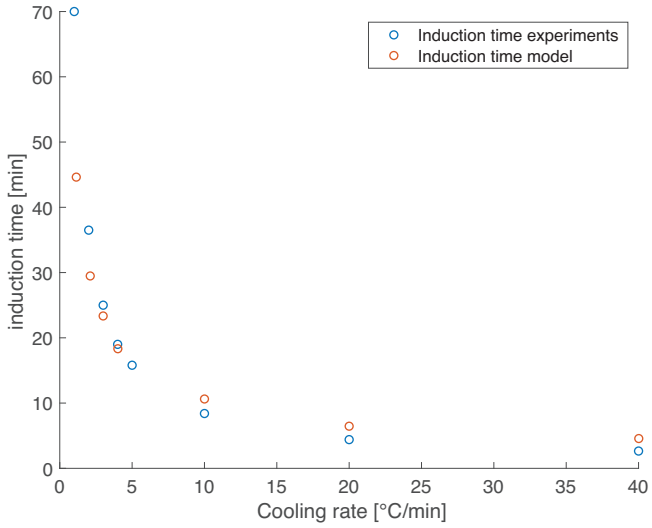

Figure 5.3: Induction time determined by experiments and predicted by the model

An new method to obtain the induction temperature is developed. The induction time of cooling rates of 5, 10, 15, 20, 40 and 80 °C/min are plotted in figure 5.4. Applying an exponential fit predicts a the induction time for higher cooling rates. From this plot the temperature at which the induction starts is calculated and plotted in figure 5.5. Choupin et al. [67] noted that a cooling rate of 140 °C/min was sufficient to prevent the formation

of crystalline regions. Our calculated induction time for 140 °C/min is 78.4651 seconds. The starting point is 183 °C, which is already out of the range in which crystallization happens. This indicate that model matches this condition. Figure 5.11 illustrate the range at which crystallization happens spanning from 188 °C until 310 °C. The induction time is translate to a induction temperature. The induction temperature versus cooling rate of figure 5.5 will be the first condition which has to be meet in the crystallization algorithm for applying the analytical model.

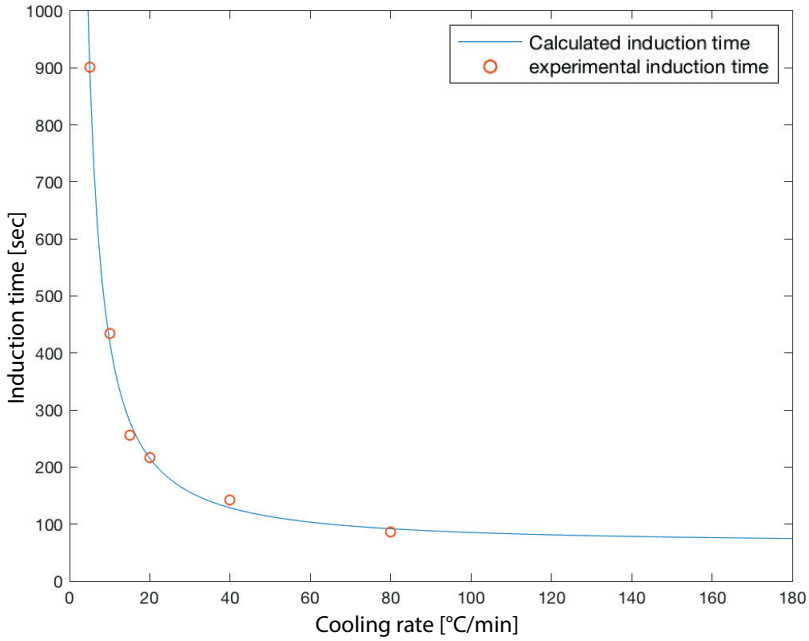

Figure 5.4: Induction time of different cooling rates

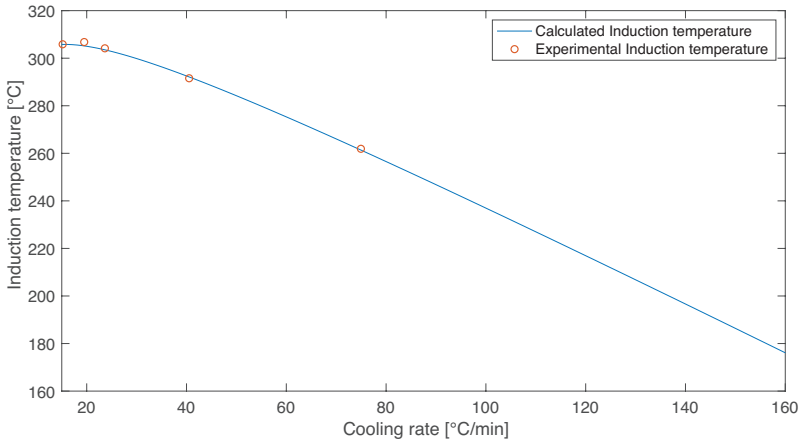

Figure 5.5: Induction temp of different cooling rates

5.2. ISOTHERMAL CRYSTALLIZATION

Isothermal DSC experiments are performed to study the crystallization kinetics of the CF/PEKK at different temperatures. Samples are prepared as described in section 3.1.1. Specimens are heated to 380 degrees and held for 5 minutes. They are cooled to temperatures between 265 °C and 285 °C at a rate of 140 °C /min to suppress crystallization. Complete crystallization was reached within 45 minutes for each temperature, as seen in figure 5.6 for an overview of the isothermal crystallization. As the isothermal temperature is raised towards the melting temperature the peak broadens and the area underneath the peak decreases. This means the crystallization rate decreases as the isothermal temperature comes closer to the melting temperature.

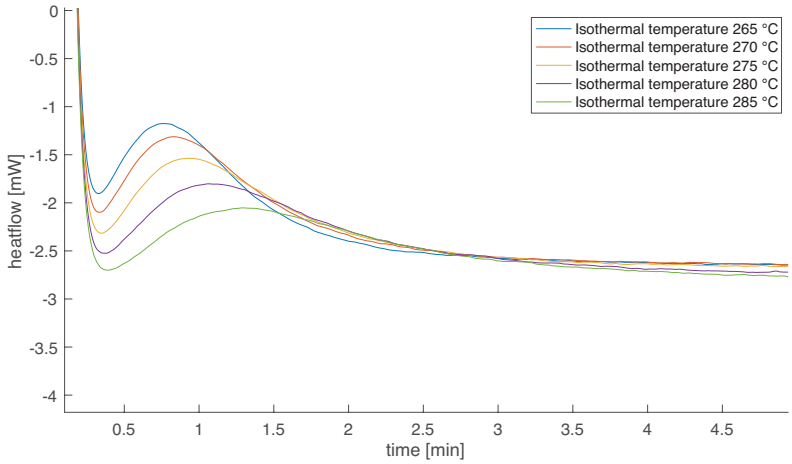

Figure 5.6: Overview of isothermal crystallization

5.3. NON-ISOTHERMAL

The non-isothermal experiments are based on heating and cooling the CF/PEKK with a controlled rate. The specimens are prepared in the manner described in section 3.1.1. The DSC measures the heat flow of the sample during the different programs and comparing it to a reference cup. The influence of the aluminium cup on the heat flow is eliminated by subtracting the heat flow from a run with an empty cup from the heat flow for a run with the sample in it. Due to sufficient age and misuse of the Perkin Elmer Differential Scanning Calorimeter DSC-7 at the Faculty of Applied Sciences it wasn't possible to measure the specimen and reference cup in one run. To compensate for this, two separate runs had to be conducted for each heating or cooling run. The first run containing the aluminium cup with the specimen and the second run with the reference pan, adding experimental time to the process. DSC experiments have been conducted at a broad range of cooling and heating runs.

Measurements were conducted on specimens with a weight between 8 and 10 mg. All specimen are first heated to 380 °C at a rate of 10 °C/min to remove any prior crystallinity from the polymer and obtain a fully amorphous polymer . For crystallization from the melt the specimen were cooled from 380 to 180 °C at various constant cooling rates be-

tween 1 and 80 °C/min. For glass crystallization the samples are cooled to 180 °C at a rate of 140 °, at this rate the polymers does not have enough time to crystallize. An overview of the crystallinity kinetics for non-isothermal crystallization is given in figures 5.8 and 5.11.

The ordering of the polymer chains occurs at temperatures between the equilibrium melting temperature and glass transition temperature. The process can be subdivided into three phases: induction, crystal growth and secondary crystallization. For all cases there is a clear induction time prior to crystallization. For higher crystallization temperatures the induction time increases. The glass and melt crystallization will be subdivided into two, the low rates and the higher rates. Low rate results in a similar degree of crystallinity whereas with high rates result in a lower degree of crystallinity, increasing rates cause a decrease in degree of crystallinity.

5.3.1. HIGH CRYSTALLIZATION RATES

The literature on isoconversion has highlighted two different rate regions to predict crystallization rates, using cooling and melting rate similar to the regime which you want to predict. Which has the advantage that is directly gives a indication on the crystallization rates within this region. The alternative is using low cooling rates, the advantage of low cooling rate is the distinguished crystallization region. Crystallization will happen at temperatures close to the glass transition en melting temperature. In these regions the K_g or U^* will be more dominant, resulting in a more accurate determination of K_g or U^*. An overview of the DSC experiments is shown in figure 5.8 The DSC produces one output value, the resulting heat flow $[mW/g]$. This output value is used to calculate the total degree of crystallinity, which is equal to the area underneath the peak. Other interesting information from the DSC data are the induction point, which is equal to the feet of the peak and the relative extent of conversion. As can be seen from the results for glass transition, for higher heating rates the start and end temperatures increase. Whereas the area under the degree of crystallinity decreases. Figure 5.7 shows the relative extent of crystallization versus temperature and time. The same trend is observed as in the case of melt crystallization. An increase in cooling rate results in a delay in onset temperature and the end of crystallization at lower temperatures.

Table 5.2: Onset and crystallinity obtained from DSC experiments

	Glass Transition		Melt Transition	
	Onset Temperature [°C]	Degree of crystallinity [%]	Onset Temperature [°C]	Degree of crystallinity [%]
5	193.7	19.8	305.3	20.7
10	196.8	16.8	304.9	18.3
20	202.3	10.6	303.1	11.1
40	207.5	8.35	285.8	8.5
80	240.0	5.8	259.69	6.3

Table 5.2 provides an overview of the results of the DSC experiments. General trends are

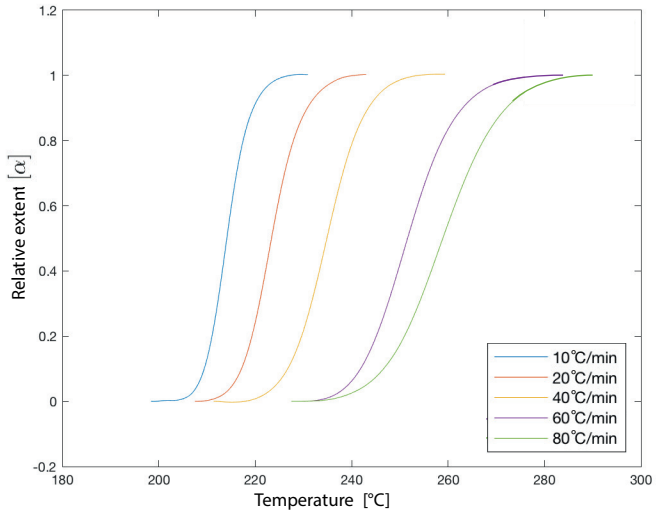

Figure 5.7: Overview of relative extent of conversion for glass transitsion

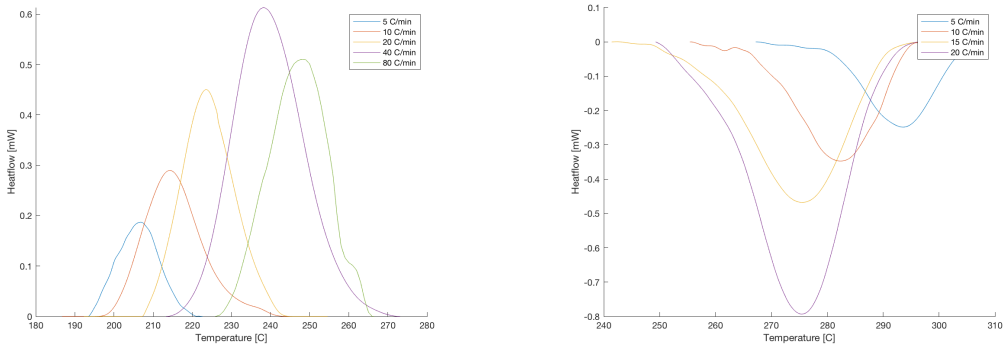

(a) Glass transition

(b) Melt transition

Figure 5.8: Heatflow versus temperature

that higher cooling or melting rates result in a lower degree of crystallinity. All degree of crystallinity measured with the assumption that the fiber volume fraction within the specimens is 60 %. This assumptions is made during the complete research, the precision of the measurement would increase as the DSC experiments would be follow by thermal gravimetric analysis (TGA) experiments which will determine the fiber fraction of the specimen by heating the part while measuring it's weight. As soon as the PEKK is completely degradated the loss in weight of the specimen can be used to determine the fiber volume fraction. Within this research a constant fraction is assumed but for follow up research determining the fiber fraction is advised. Figure 5.9 illustrates how the relative extent is translated to a rate of conversion. Figure 5.10 illustrates an informative plot of the rate of conversion normalized by the cooling or heating rate. There is a clear trend of decreasing rate for higher rates. The peaks all show a queue at long times that indicates the secondary crystallization process, similar as reported by other

authors [86, 118]. No clear distinction can be made whether this phenomenon is more pronounced for glass or melt crystallization. The higher cooling and melting rates overlap in the middle of the graph, in this region the rate of conversion is determined by some combination of U^* and K_g, although it is unknown which is Dominant.

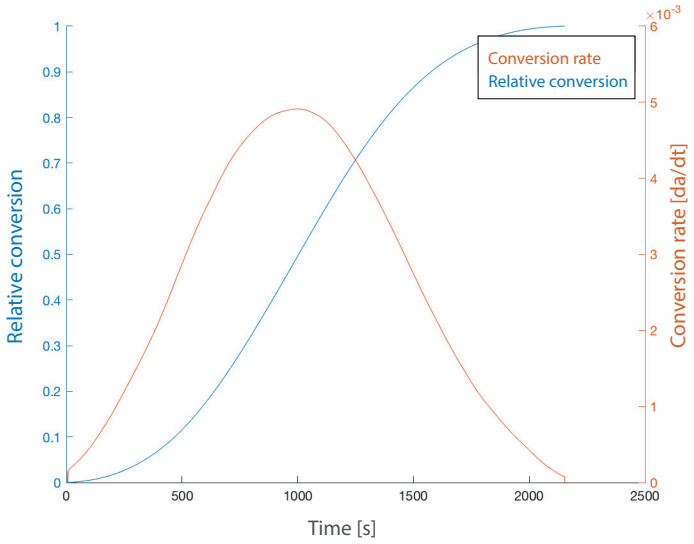

Figure 5.9: Translation of relative conversion to rate of conversion

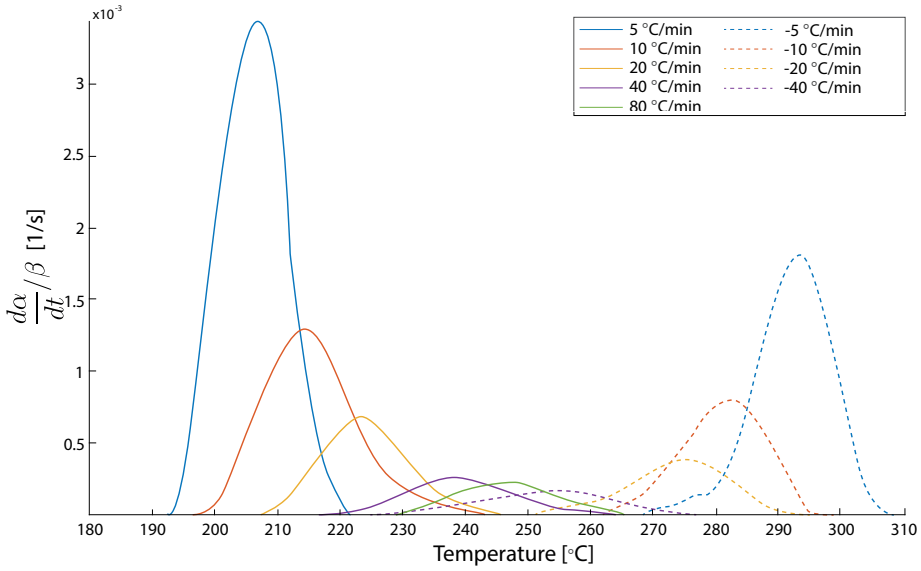

Figure 5.10: Induction time versus isothermal temperature

5.3.2. LOW CRYSTALLIZATION RATES

Unlike high crystallinity rates that occur over a large range of temperatures, low cooling rates happen at a narrower region however, the same trends are observed as for the higher rates. The sharp onset and steep beginning of the phase transition indicates the presence of a large number of preformed nuclei. The surface of the CFs could act as

possible nuclei onset points, whereas the CFs reduced the surface energy for nucleation. The sharp shape could be explained by nucleation on the CF surface.

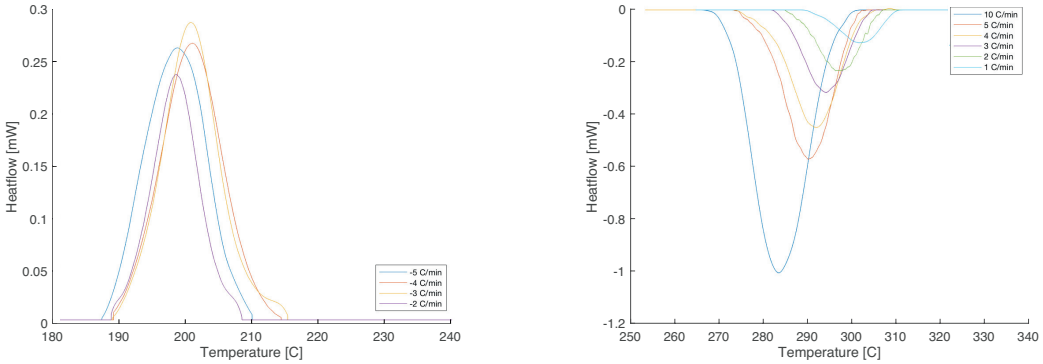

(a) Glass transition

(b) Melt transition

Figure 5.11: Heatflow versus temperature

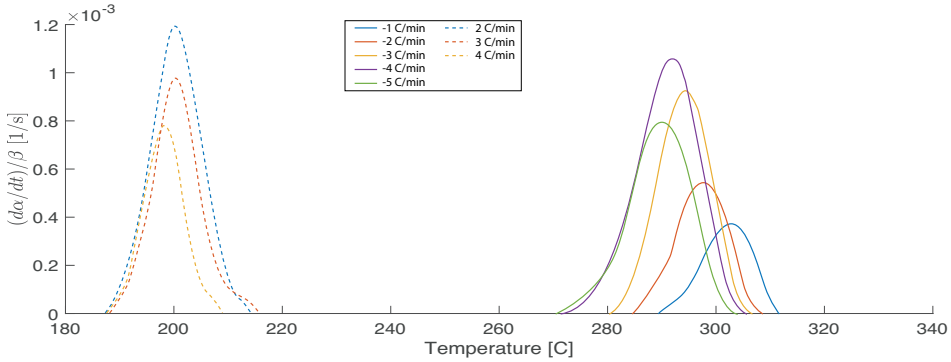

Figure 5.12: Relative conversion rate for low crystalliztion rates

5.3.3. DISCUSSION OF CRYSTALLIZATION DYNAMICS

Although the general trends within the crystallization of PEKK are the same as reported for the crystallization of other polymers [83, 85, 107], there are some results which differ from the trends. Curves that deviate form the trends are the 80 °C/min for the glass transition, or the curves 3-5 °C/min in figure 5.11 (a and b).However, due to the limited sample size of the experiments no immediate conclusions can be drawn. The reliability of results can be greatly increased by extending the number of test conducted with the same rates. Larger sample size provide more accurate mean values and help to identify outliers that could skew the data in a smaller data set as which may be the case for the example mentioned above. Considering the time span of a master thesis, larger sample sizes could not be considered.

5.3.4. ACTIVATION ENERGY

The activation energy is determined using the method developed by Ortega et al [113]. Depending on the cooling or heating rate, the same extent of conversion is reached at different temperatures. The same extent of conversion is used to evaluate an average temperature correlated with the [α] value. Figure 5.13 and 5.14 illustrates two graphs, the first graph illustrates the relation between the average temperature and the activation energy determined by the linear integral method of Ortega et al [113]. The second graph relates the extent of conversions to the activation energy, it depicts the typical bell shape. The activation energy converges to zero as the relative extent of conversion approaches full completion. The negative activation energy for melt crystallization is similar as reported by Vyazovkin et al [116]. The break point within the activation energy indicates more than on regime of crystallization as described in section 2.2. There are two breakpoints in both the melt and glass crystallization, they are indicated by the red stars. The multiple regimes require determination of U^* and K_g for each region separately. Making predictions of the crystallization is a complex procedure. The method of Farjas et al [118] provides a pathway to simplify it, as it determines the activation energy depending on the relative extent of conversion directly integrating switches of regimes within the method.

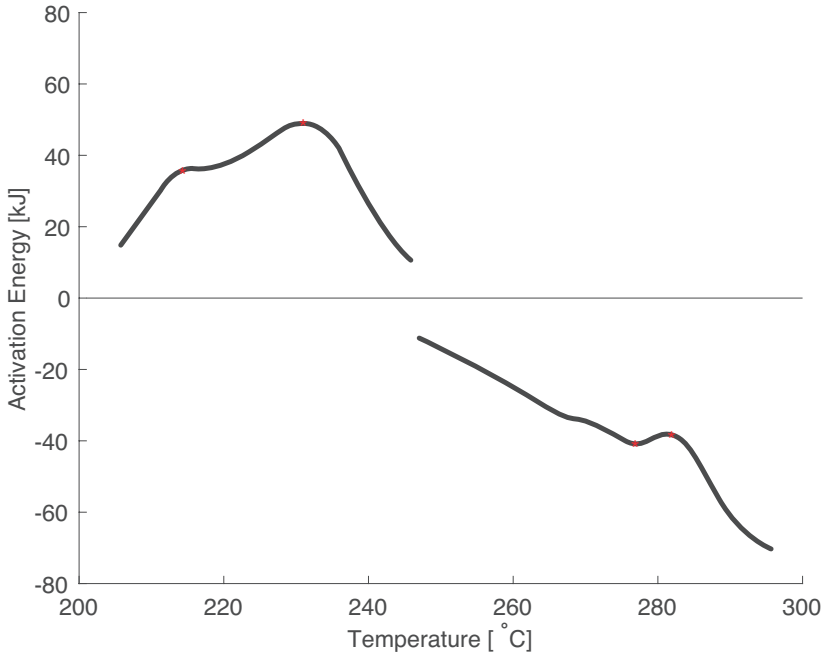

Figure 5.13: Activation energy versus Temperature

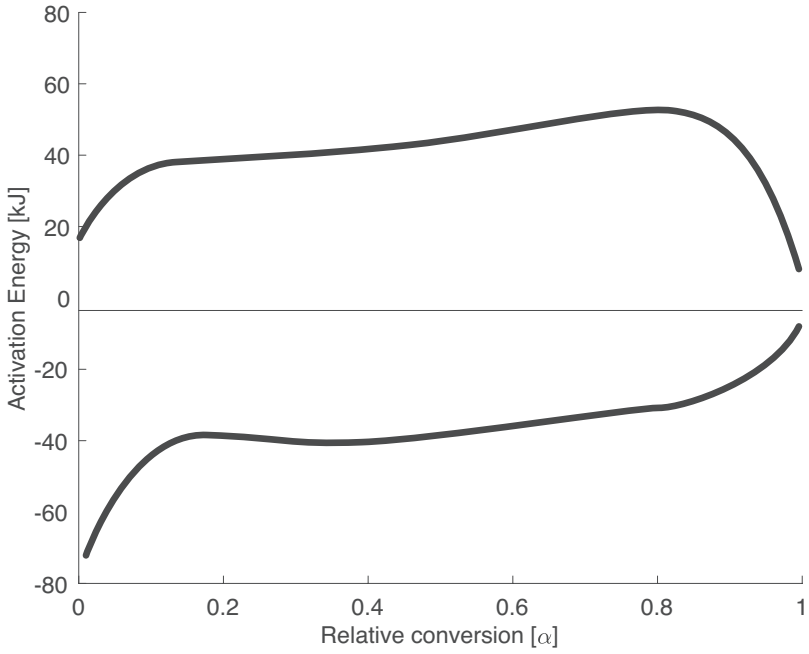

Figure 5.14: Activation energy versus relative crystallinity

6

ANALYTICAL MODEL

The results from chapter 4 will be used in order to model the crystallization at the weld interface. This chapter address the question of whether it is possible to predict the crystallization of Uni-Directional (UD) Carbon Fiber (CF) Poly Ether Ketone Ketone (PEKK) at the weld interface for an arbitrary cooling trajectory. An attempt was made to model the crystallization kinetics with the analytical model suggested by Farjas and colleagues [118]. To the best of the author's knowledge, the Farjas method is the first model to predict crystallization of isothermal runs with data from non-isothermal runs. This could be an indication that the model is capable to predict arbitrary cooling trajectories.

6.1. FARJAS MODEL

The analytical model is based on the assumption that the kinetic parameters, pre exponential term $k_0 g(\alpha)$, activation energy for chain diffusion (K_g) and activation energy for nucleation ($U^*(\alpha)$) are dependent on the extent of conversion. Relating the extent of conversion to total degree of crystallinity offers the opportunity to link changing cooling rates to each other. The model proposed in the next section is to the authors knowledge the first attempt to use the isoconversional method to predict the crystallinity of arbitrary cooling trajectories. Being able to predict these conditions is of much higher interest to the industry, due to the fact that one is no longer limited to DSC conditions (constant cooling rate of constant temperature). The method of determining the kinetic triplet is already briefly described in section 2.4.1. Figure 6.1 illustrates the procedure in more detail.

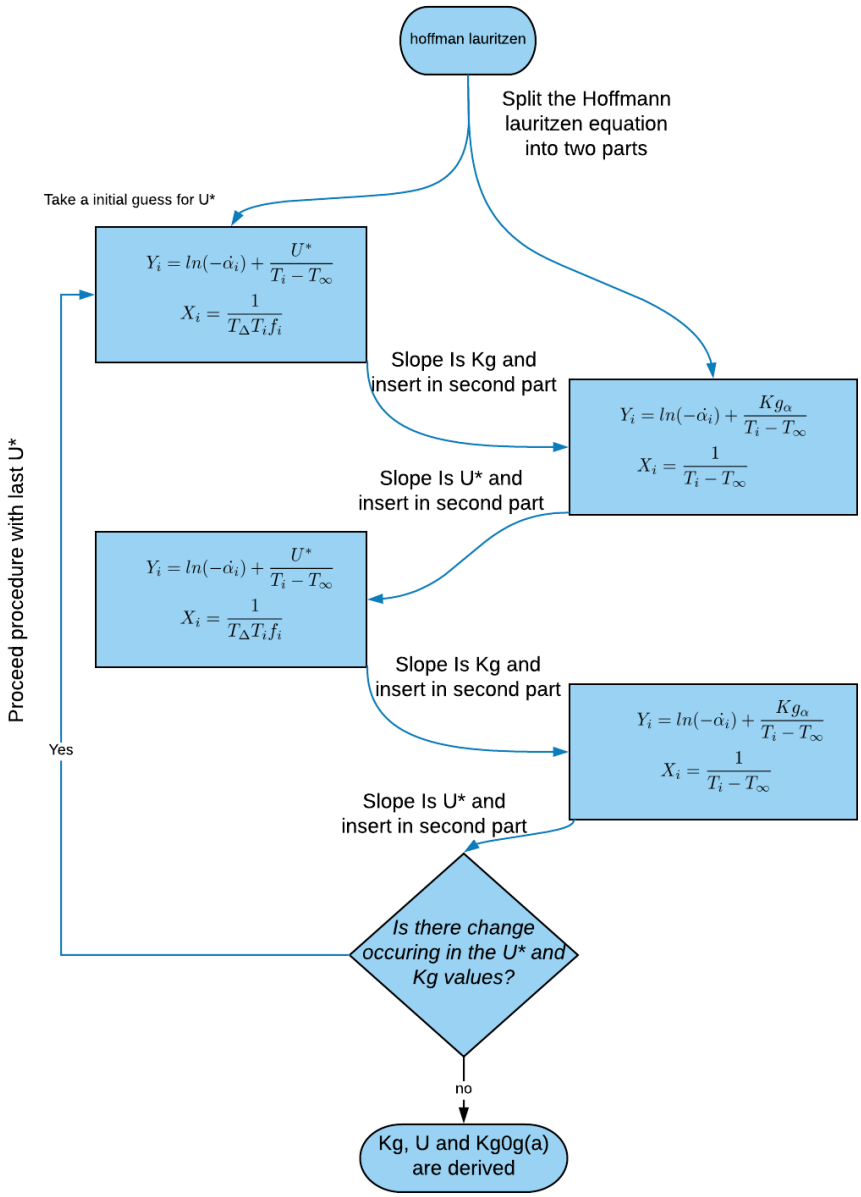

Figure 6.1: Flow chart of the interation method used to determine the Farjas parameters

6.1.1. FARJAS PARAMETERS

As described in section 2.4.1 the Farjas model is based on the assumption that for each relative extent of conversion there is a corresponding pre-exponential ($k_0 g(\alpha)$), activation energy for diffusion (K_g) and activation energy for nucleation(U^*). The method described in the section is used to find the three kinetic parameters. Figure 6.2 shows the procedure for 0.5 extent of conversion. The iterative procedure is terminated as soon as the R-square converges to a value close to 1. The pre-exponential factor $k_0 g(\alpha)$ scales the height of the bell shape and increasing the factor leads to a increase of the height. As the parameter does not depend on temperatures there are no temperatures the width of the bell shape will be constant. Decreasing (U^*) leads to a broadening of the bell shape

towards the glass transition temperature, U^* is the activation barrier for nucleation since and decreasing the barrier will allows nucleation at lower temperatures. The activation barrier for chain diffusion (K_g) will determines the width and height of the peak; decreasing K_g results in the peak slightly shifting towards the melting temperature but the effect is less pronounced when compared to U^*. The kinetic parameters and their dependence on α are shown in figure 6.3. U^* is lower then the universal value (6000 J/mol) described by Hoffman [108] and increases as the degree of relative crystallinity increases. This is a rather surprising outcome as polarized light microscopy and XPS have shown linear growth until impinging which indicates a constant U^* and K_g. This phenomenon is explained by the secondary crystallization processes occurring at the ends of the crystallization process and the U^* will be a combination of both activation energies for chain diffusion. The 'nucleation constant', K_g has two peaks,one at the start and one at the end of the relative extent(α). The first peak can be explained by the fact that nucleation has to overcome the free surface barrier at nucleation. The origin of the last peak is not clear but could be due to the secondary crystallization happening at the end of the DSC crystallization peak. The $K^*_{0\alpha}G(\alpha)$ is proportional to U^*.

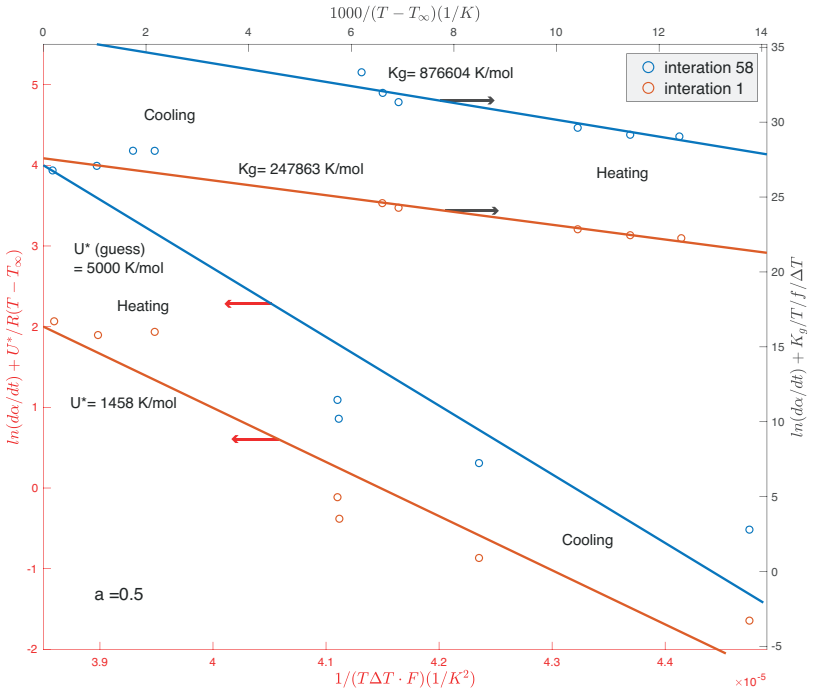

Figure 6.2: Iterative procedure used to determine the farjas parameters for 0.5 extent of conversion.

6.1.2. ISOTHERMAL PREDICTIONS

The strength of the Farjas method compared to other methods to predict crystallization is the fact that it is capable to predict Isothermal runs, with the kinetic parameters determined by non-isothermal runs. This hints on the capability of the model to predict the crystallization an over arbitrary temperature program. Figure 6.4 provides the results

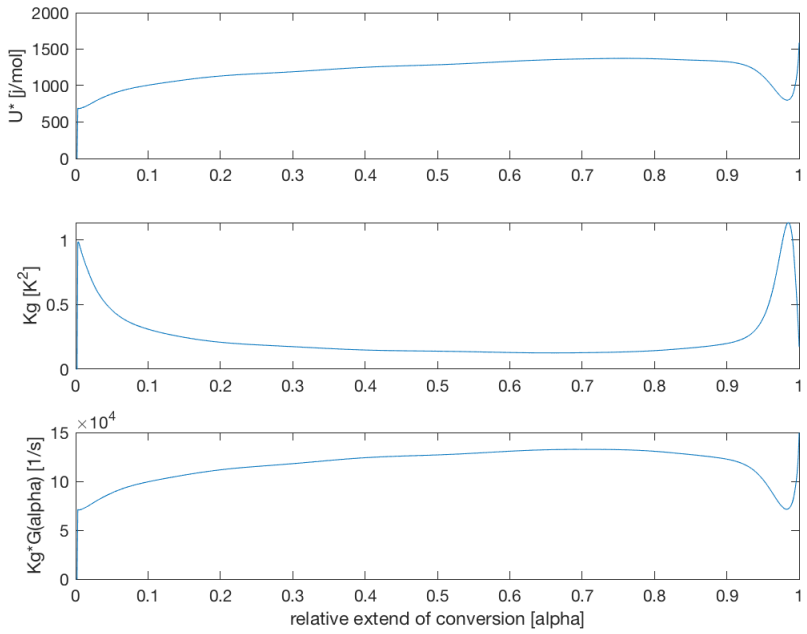

Figure 6.3: Dependence of the kinetic parameters of PEKK crystallization on the transformed fraction

6

obtained from the calculated conversion rate and the experimental conversion rate of an isothermal run of 290 °C. Due to model sensitivity, considering the correct induction time and relative extent of conversion are vital to predict correct conversion. For each run there is one discrete temperature per extent of conversion. A correct onset temperature is also important for accurate predictions. The model input variables are temperature and extent of conversion, in the case of incorrect onset temperature the relation between temperature, extent of conversion and resulting conversion rate will differ from the experiments. The increase in extent of conversion is related to the conversion rate, resulting in slightly higher or lower conversion rates. As a consequence, the shape of the predicted curve starts to deviate at later stages of the process when compared to the experiments. Nevertheless, the predictions provide a close approximation of the experiments, indicating the strength of the model.

6.1.3. NON-ISOTHERMAL PREDICTIONS

The predictions of the analytical model for non-isothermal cooling shown in figure 6.5 show good agreement for the lower rates. The induction temperature is close to the experimental runs. There is a clear trend within. In the current model, the dependence of $k_0 g(\alpha))$,(K_g) and (U^*) up to 0.05 and from 0.95 until the end is determined with insufficient accuracy.

$$\Delta T_c p = \frac{1\beta}{2D} h^2 \tag{6.1}$$

Where D and β are the thermal diffusivity ($10,7 * 10^{-7}$ for CF/PEKK) and cooling rate respectively, and h is the sample thickness (0.6 mm). The corrected results have a more

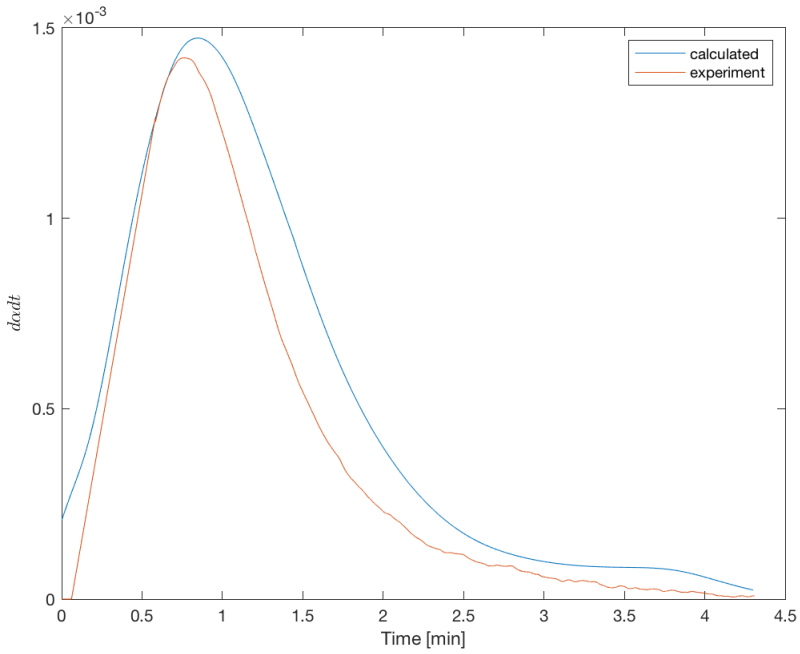

Figure 6.4: Isothermal prediction on the basis of kinetic parameters determined by non-isothermal data

uniform relation between different crystallization peaks, where increasing the cooling or heating rate shows the same crystallization kinetics trend as observed in other crystallization experiments [134, 135].

The figure clearly show the potential of the analytical model, its capability to predict a conversion rate based on the conversion and temperature. There is a clear order within the predictions, the conversion rate of the 2 °C/min is twice as high as the crystallization rate of the 1 °C/min, the same is observed for the 5 and 10 °C/min. This relationship between conversion rate and cooling rate is the same as reported in other crystallization kinetic articles [134, 135]. The kinetic parameters based on low cooling and heating rates were used to predict the crystallization of higher cooling rates. Figure 6.6 presents the crystallization kinetics predicted for higher cooling rates. What is striking about these predictions is that the analytical model is based on lower cooling rates but still is capable to estimate the shape and conversion rate of these experiments. This shows the capability of the analytical model to predict crystallization outside the original database of experimental results. This is essential for the analytical model. Whereas cooling rates deduced from measurements and the simulations span from 200 to 80 °C/min. DSC is only capable of measuring cooling rates up to 80 C/min with accuracy. So DSC experiments with similar cooling rates are not possible. As discussed in section 5.3.3, the limited size of the sample group will decrease the accuracy of the analytical model, however this shows the promising capability of the analytical model. The accuracy of the analytical model will only increase with increasing sample size.

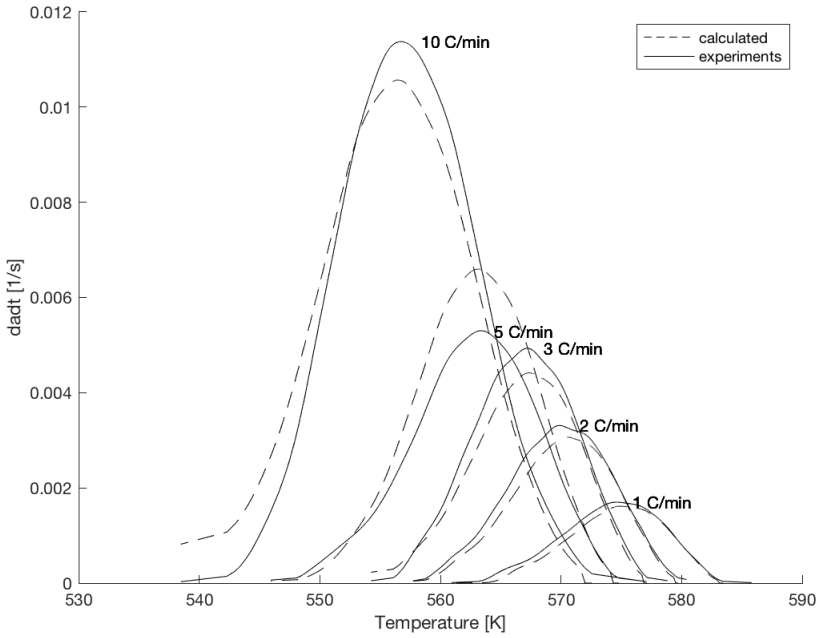

Figure 6.5: Prediction of low cooling rates

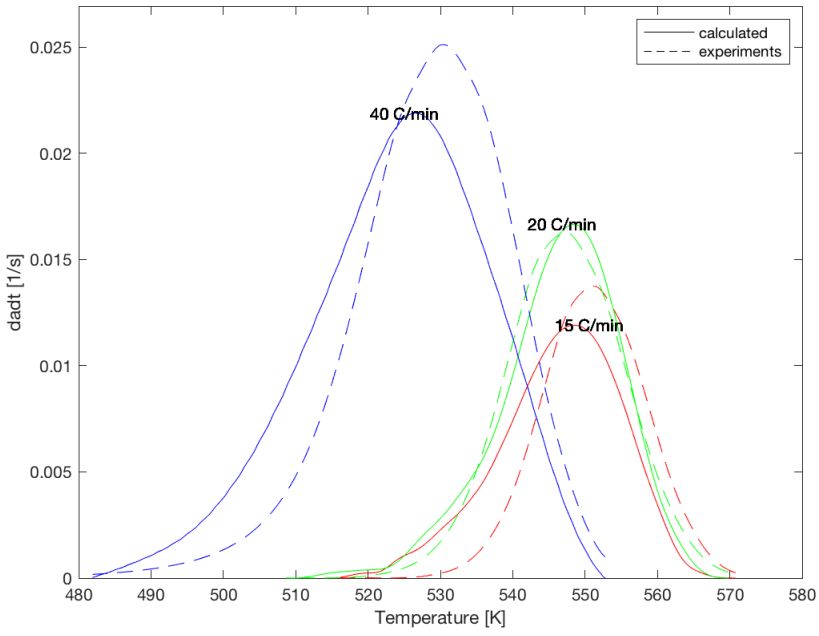

Figure 6.6: Prediction of high cooling rates

6.2. ANALYTICAL MODEL SET-UP

To use the analytical model to predict the crystallization rate for an arbitrary cooling trajectory, the relative conversion is translated to the degree of crystallinity for the current cooling rate. The flow chart on which the analytical model is based is shown in figure. 6.7.

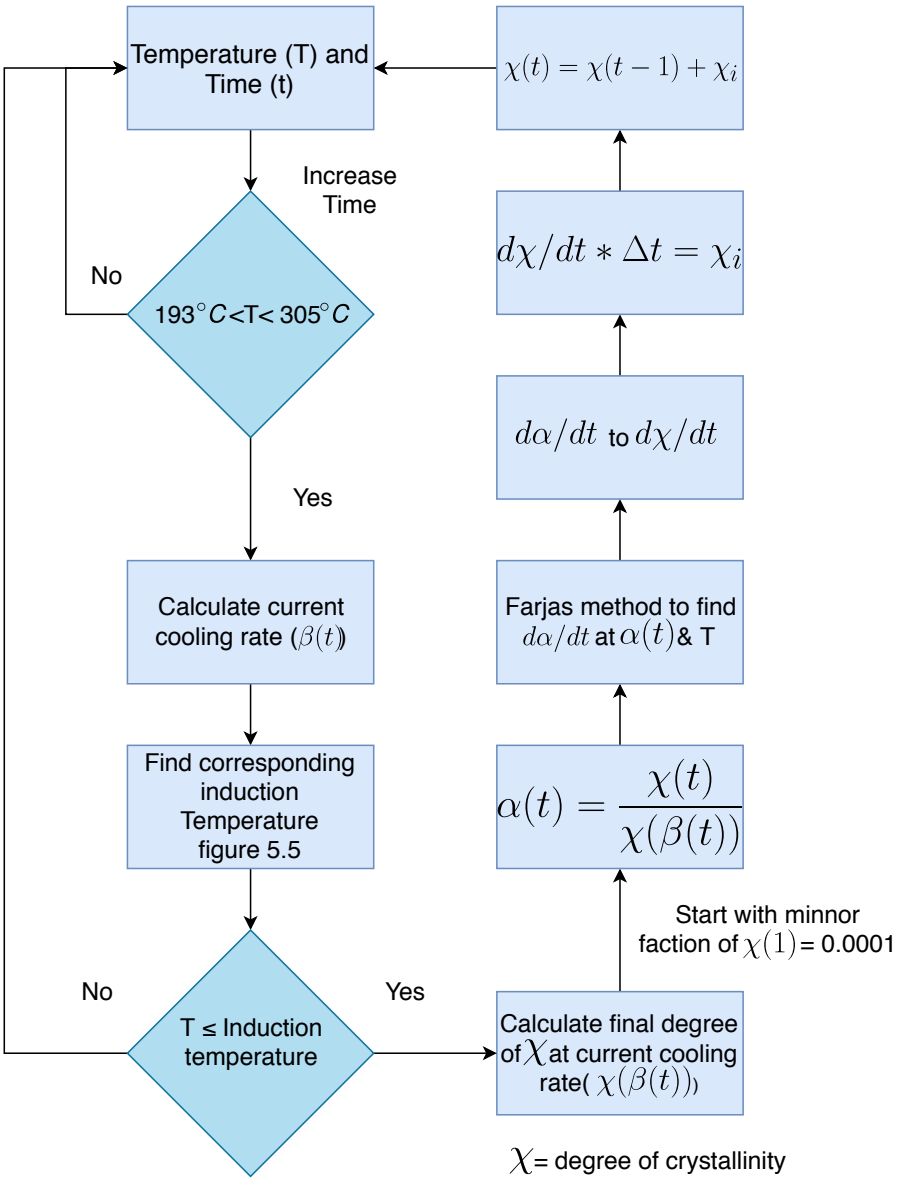

Figure 6.7: Flow chart analytical model

Computing the degree of crystallinity for a given temperature and time provided by the computational model or the experiments. The program will check if the temperature is between the bounds at which crystallization happens. If this is not the case the program will proceed to the next step (new time and temperature), if this is the case the current cooling rate is calculated. The current cooling rate corresponds to an induction

temperature determined as in section 5.1. If the temperature is lower than the induction temperature the crystallization will start. If not the program will proceed to the next step. As the crystallization starts, the total degree of crystallization for the current cooling rate is calculated ($\chi(\beta(t))$). The current degree of crystallization ($\chi(t)$) divided by the total degree of crystallization at this current cooling rate ($\chi(\beta(t))$) is the relative extent of conversion ($\alpha(t)$). The analytical method is used to determine the relative conversion rate at the current conversion and temperature. The analytical method predicts the relative conversion rate ($d\alpha/dt$); this is translated to a crystallization rate $d\alpha(t)/dt * d\chi(\beta(t))) = d(\chi)/dt$. The degree of crystallinity formed during the current step is added to the total degree crystallinity formed. The process is repeated until the temperature is below the crystallization temperature bounds.

6.2.1. CRYSTALLISATION ROAD MAP

The Farjas equations constructs a road map from which the rate of extent can determine if the extent of conversion and the temperature is known. The two basic examples can be provided for isothermal and non isothermal conditions. For the first we would start at for example 240 °C and 0 extent of conversion. The crystal will start to nucleated and grow, the temperature will be constant but the extent of conversion will increase. This will eventually result in a straight vertical line starting at 240 °C and 0 extent of conversion and ending at 240 °C and 1 extent of conversion. This would result in a rate of conversion graph as shown by figure 6.4. The non isothermal example is slightly more complex, for a cooling rate of 3 °C/min that starts to crystallize around 305 °C with the corresponding extent of conversion as 0, the crystallization ends at 283 °C and at an extent of conversion of 1. The line between the two would probably be a S curve because at the beginning and end there is a small rate of extent but a large range of temperature, resulting in relatively more motion in the horizontal direction and a small motion at the vertical direction. In the middle we would find a relative large motion in the vertical direction and a small motion at the horizontal direction. To use this principle for an arbitrary temperature program a second translation is needed. The extent of conversion has to be translated for each cooling rate. Figure 6.9 shows the relation between cooling rate and degree of crystallinity. For example, a specimen starts to nucleated at a temperature of 290 °C with a cooling rate of 20 °C/min. For this cooling rate the total degree of crystallinity is 13.8 % and an average rate of extent of 0.005 $\frac{d\alpha}{dt}$. After 30 seconds the temperature is 280 °C, in this period the relative conversion increased to 0.15 α. This would mean a degree of crystallinity of 2.07 % has been established, determined from figure 6.9. Now changing the cooling rate to 18 °C/min, the total degree of crystallinity is approximately 15 %. For this cooling rate a higher total degree of crystallinity can be reached and the 2.07 % is now only 0.138 α compared to it's previous 0.15 for the cooling rate of 20 °C/min. The result is a repositioning on the crystallinity road map at the vertical axis. This example showed the interaction between the changing cooling rate and the Crystallization road map. The map itself provides a fast insight on the global crystallization kinetics of CF-PEKK. The highest rates are obtained around 230 °C and with an extent of conversion around 0.5 α. At high and low relative extent there are low conversion rates, and the same is true for temperatures close to the Glass transitions temperature or melting temperature.

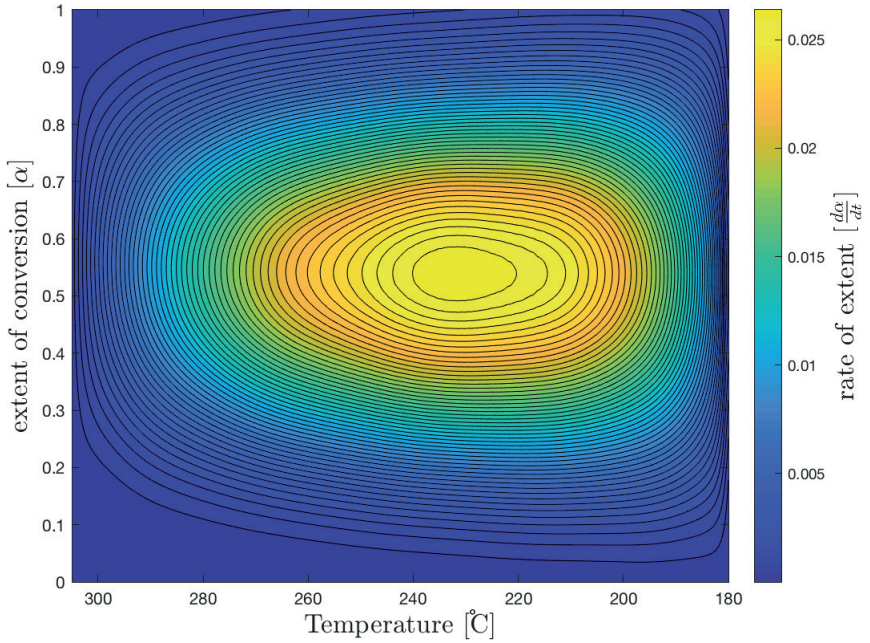

Figure 6.8: Relation between relative extent of conversion versus temperature and the resulting cooling rate

6.2.2. NON CONSTANT RATE DSC VALIDATION

Precise validation of the analytical model is complex, compared to validating for constant temperature and constant cooling. The validation of the analytical model would preferably be conducted in a conditioned environment. The Perkin Elmer DSC 8000 [136] allows one to program different sequential cooling rates which can approximate the cooling trajectory observed during welding. Figure 6.10 Illustrates the different cooling trajectories programmed into the DSC. The advantages of this method are that the DSC can closely control the cooling rate while directly measuring the temperature of the sample and it's heat flow. A small and light sample can be tested, limiting internal gradients within the material resulting in a more equal distribution within the sample. Figure 6.11 illustrates the heat flows measured during non constant cooling. The changing cooling rate requires the program to adjust its energy required to cool, this can be observed in the graph by little peaks. The program changing from cooling rate will result in a change of the baseline. This changing baseline makes observations about onset of the peak and the area underneath the peak difficult. As observed in section 5.1 changing temperature from constant rate to a constant temperature to a cooling rate will require the DSC to stabilize the signal. Due to this unclear baseline and peak area direct conclusions from the graph in figure 6.11, can not be drawn. A more conclusive matter to determine the crystallinity developed during the different cooling programs, is by a subsequent heating stage in which the crystallinity during heating is compared with enthalpy of melting as subscribed by in section 6.6. This method will find the crystallinity developed during the cooling stage. This degree of crystallinity is compared to the crystallinity predicted by the analytical model. Table 6.1 shows the crystallinity developed during the cooling

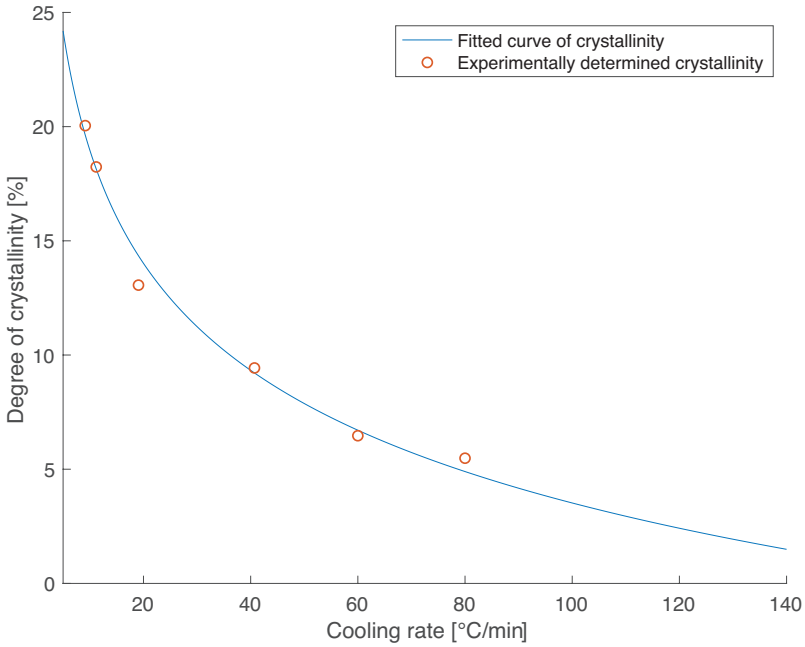

Figure 6.9: The effect of cooling rate on the total degree of crystallinity

stage measured by the experiments and the degree of crystallinity predicted by the analytical model. The degree of crystallization predicted by the analytical model follows the same trend as the degree of crystallization found during the experiments. The analytical model predicts a lower the degree of crystallinity than the observed degree of crystallinity. There could be multiple reasons for the deviation between the predictions and the results, the first is that the analytical model is based on the assumptions that the fibre volume fraction is 60 %. If the fibre volume fraction of the specimen is lower than the assumed fibre volume fraction this will lead to higher measurement, as can be seen from equation (3.4). To increase the precision of the validation an additional resin burn off in a thermal gravimetric analysis (TGA) should be applied, as previous mentioned. A second reason is that the extent of conversion is related to the degree of crystallinity which can be developed for different cooling rates. Figure 6.9 illustrates the relationship between cooling rate and degree of crystallinity used in the analytical model. We can see that this relationship is not a perfect fit, and one should recall the small sample size used in the experiments; a larger sample size would ensure a representative distribution of the population and increase the reliability of the experiment. The final reason, is that the induction temperature again is determined by a relatively small sample size and that this assumption for induction temperature is not yet validated. A method to find the induction temperature for non constant cooling rates has not been found. As can been seen from figure 6.11 concluding on the induction temperature based on the DSC experiments is not possible. An alternative method to validated the induction temperature cloud be the use of X-ray diffraction or Polarized light microscopy and neat PEKK, assuming programming of non constant cooling programs is possible. This methods will not be sensitive to the change in cooling rate observed by the DSC, which will allow

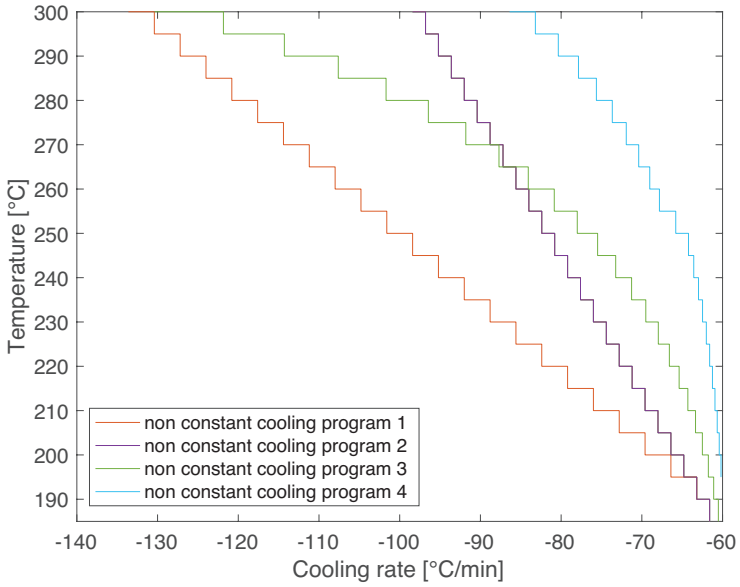

Figure 6.10: Different temperature programs with varying cooling rate

a more precise determination of the induction temperature. A note of caution for this method is that the absence of carbon fibres could influence the induction temperature as the carbon fibre surface will offer possible nucleation spots decreasing the desired nucleation energy. Taking in account all the assumptions made and the limited sample size the predictions fall in an acceptable agreement for this first attempt to predict the degree of crystallinity for non constant cooling rates.

Table 6.1: Non constant cooling validation of the model

Program [#]	Onset crystallization [%]	Degree of crystallinity [%]	Degree of crystallinity [%]
1	242	2.54	1.74
2	250	3.65	2.71
3	254	4.34	3.72
4	260	5.67	4.26

6.3. CRYSTALLIZATION OF THE SIMULATIONS

Using the analytical model the crystallization within the composites is predicted from the simulations. The simulations offer the possibly to investigate the development of crystallinity at different regions within the composite. The main focus is on at the crystallinity developed at the weld interface as in this region co-crystallization can be formed. The degree of crystallinity is determined for each node within the work piece .

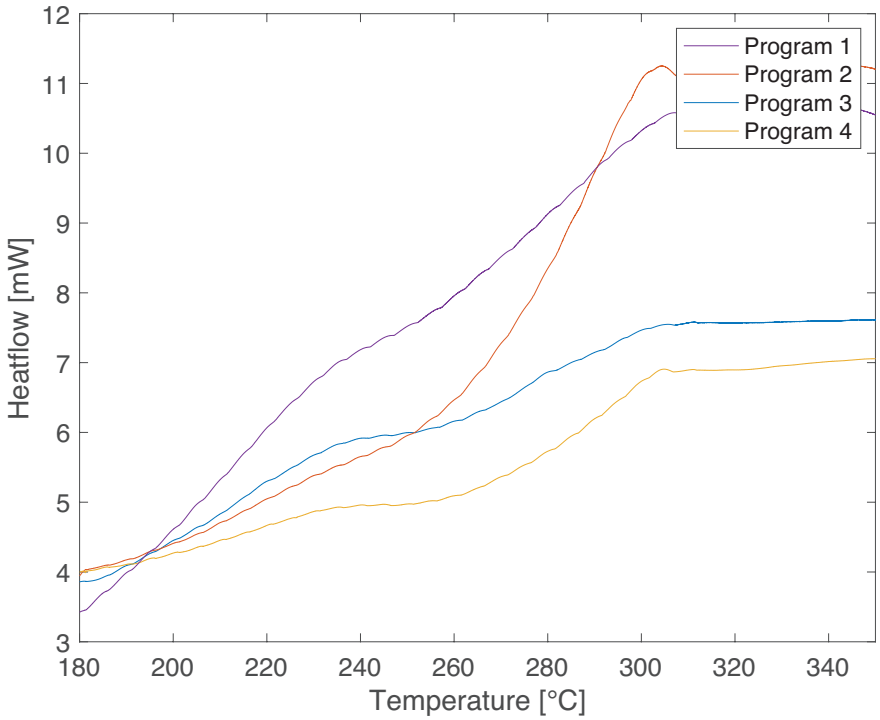

Figure 6.11: The heat flow measured during non constant cooling

6.3.1. STATIC SIMULATIONS

As can be seen from figure 6.12, a wide range of crystallinity will be developed across the weld interface. This results can be misleading, as the model assumes that the material is completely amorphous at the start of the cooling trajectory, but this is only true for points reaching the melting temperature and thereby erasing any prior state of crystallization. Therefore hence forth we will only focus on the area Proceeding from now area which has been molten ($T > 350°C$) and the surrounding surface will be represented as 0. The area shown is the region at which Cocrystallization between both parts of the interface is possible. The edges at the right side of the figure will not reach the melting temperature, so the prediction will underestimate the degree of crystallinity in these regions. The positive side of y axis from the figure is the end of the topside plate, this side will heat up slower and this will result in more crystallinity at this side. The asymmetry within the crystallization pattern is due to the asymmetry within the single lap shear configuration.

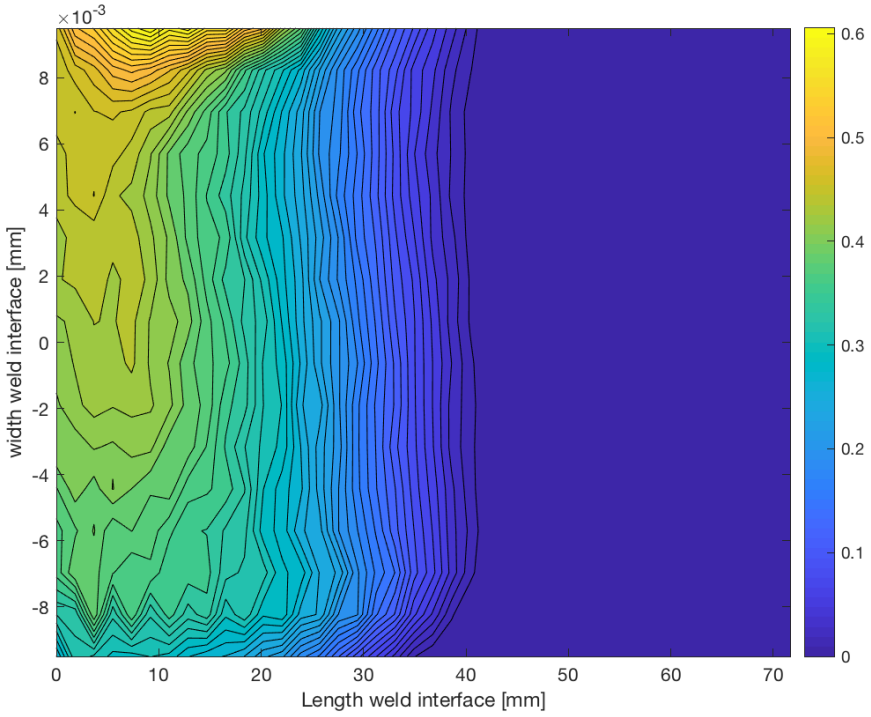

Figure 6.12: Crystallization pattern

KVE3

An overview of the relation between welding time and degree of crystallization for welding with the KVE3 heatsink is provided in figure 6.15. As suspected from section 4.2.1 the cooling capabilities of the KVE3 heatsink will almost suppress all formation of crystalline regions. Figure 6.13 will illustrate the relation between welding times and crystallinity. Crystallization is below 0.1% until the weld time is increased to 30 seconds. Experimentally determining the degree of crystallinity for these experiments will be close to the sensitivity of the DSC. The graph shows that longer welding times have a beneficial effect on the mean degree of crystallinity. The scatter observed within the results is due to the fact that not all simulations do exactly reach 380 °C. The different maximum temperature will lead to different cooling rates and as a result different degrees of crystallinity.

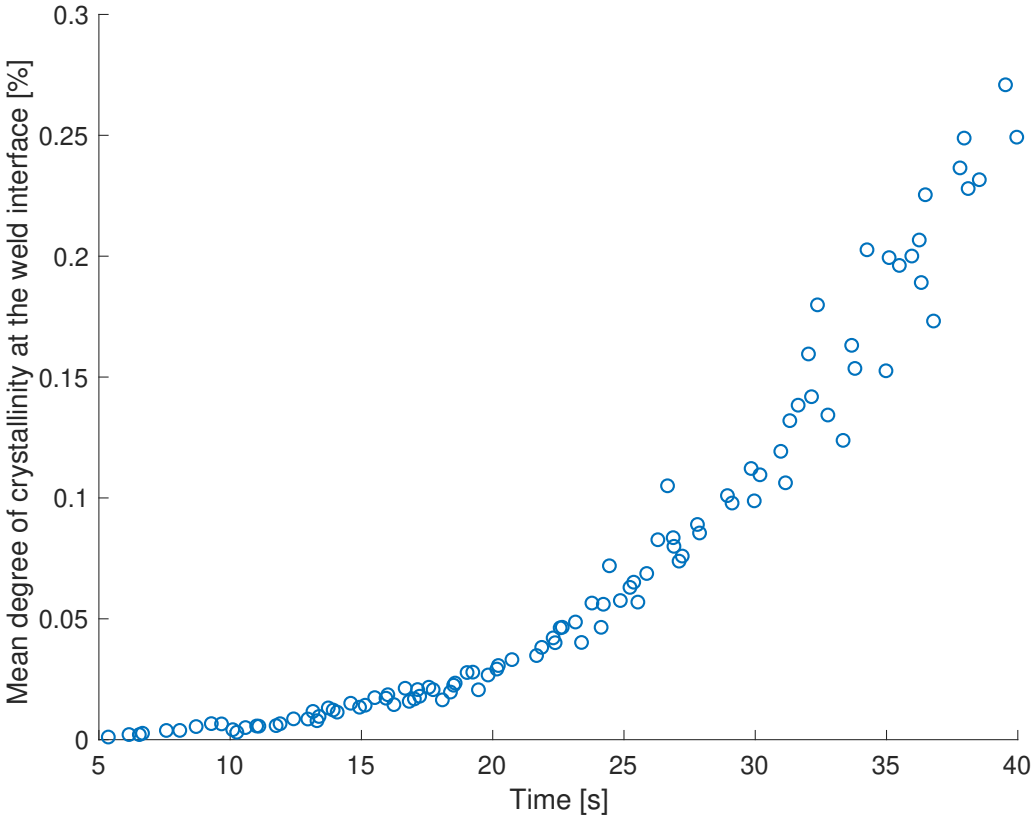

Figure 6.13: Mean degree of crystallization for different welding times

Figure 6.14 illustrates the degree of crystallinity developed after welding for 17, 22,5 and 34 seconds respectively. The first frame (a) shows a small almost amorphous weld interface, the second frame (b) degree of crystallinity slightly increases but this will still be hard to measure with the DSC. The last frame (c) demonstrates a crystalline area which has crystallized weld interface. There are only small fluctuations of crystallinity at the weld interface. The weld interface will generally follow the same cooling trajectory, because the temperature of a node is influenced by its surrounding . From the figure, it can be seen that the weld pool area increases for longer welding times.

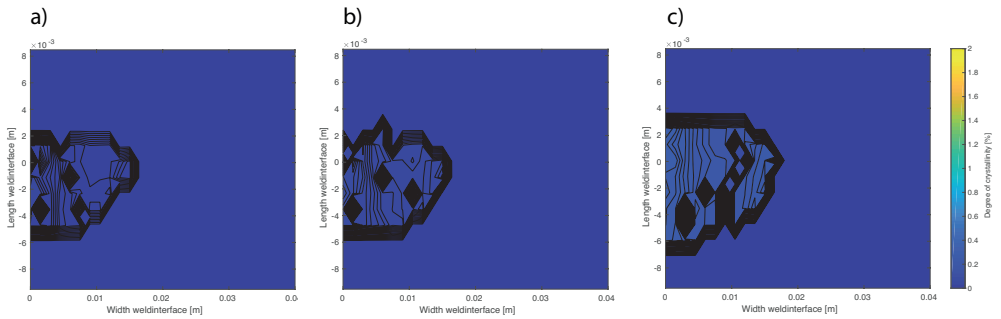

Figure 6.14: Crystallization pattern for three differnent welding times

KVE4

An overview of the relation between welding time and degree of crystallization for welding with the KVE4 heatsink is provided in figure 6.15. The effect of the parameters welding time on the degree of crystallization is straightforward, As increasing the welding time results in a higher degree of crystallinity. From the chart it can be seen that for example welding with a time of around 34 seconds results in an average crystallinity between 1.25 % and 2.25 %, The difference is due to the maximum temperature reached during the experiments. Lower maximum temperature result in a higher degree of crystallinity.

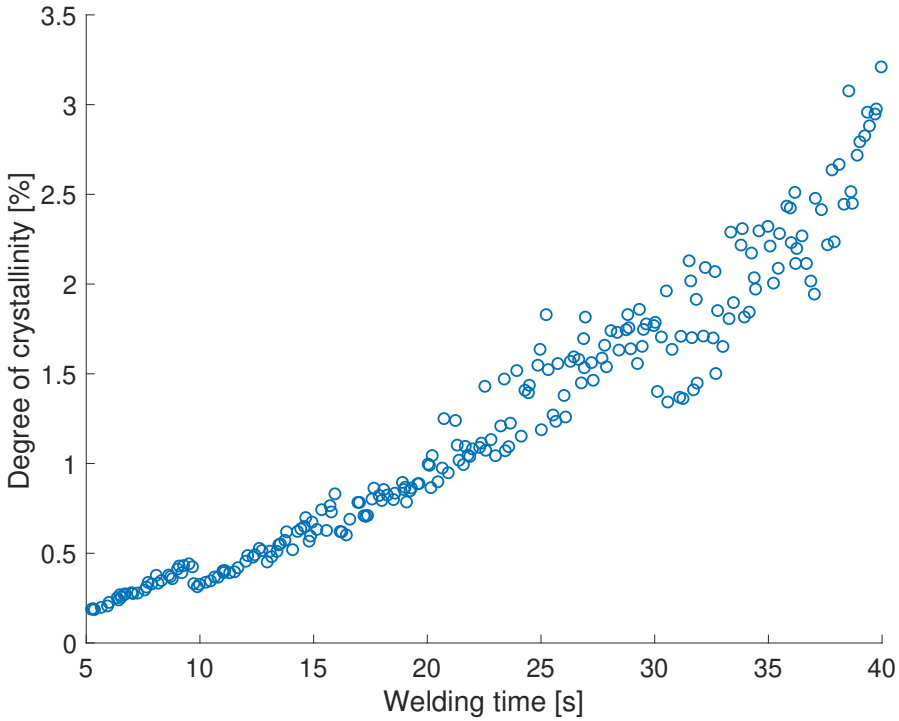

Figure 6.15: Degree of crystallization depenent on the welding time

The highest degree of crystallinity is outside the area of interest and will not contribute to better bonding. Contrary, to the heating pattern formed the maximum crystallization within the area of interest is located at the outer edges of the area. From the pattern in figure 6.16, it is apparent that the degree of crystallinity increases by a factor of 1.5 as the welding time doubles from 17 to 35 seconds. The weld pool area increases as seen for the KVE3 heatsink, but the increase is less significant as also illustrated in figure 4.13.

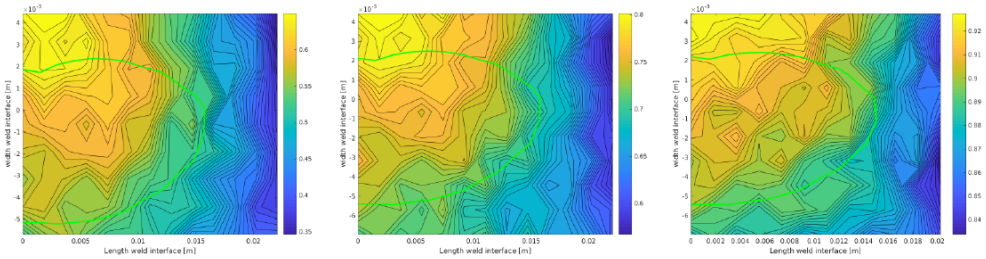

Figure 6.16: Crystallization pattern

The simulations shows the positive effect of the welding time on the degree of crystallinity, however as discussed in section 4.3.2, the model under predicts the cooling rate resulting in an over prediction of the crystallinity by the analytical model. For the static welding all experiments resulted in cooling rates above the threshold value and this would not result in any crystallinity. Therefore to validate model the dynamic tests were included into the research. The next section will first discuss the trends observed within the simulations. The simulations will compare 4 different welding configurations. Then a section applying the analytical model to the thermocouples at the weld interface. These results will be used as validation of the model in the last section in which the DSC samples from the weld interface are tested to find the resulting crystallinity.

6.4. DYNAMIC WELDING

The cooling trajectory differs from the static situation. The static case is a simple Newton cooling case in which the conduction of the heatsink will slow down or increase the cooling. For dynamic welding the heat source moving away will influence the cooling, resulting in another shape of the cooling trajectory. As soon as the heat source is no longer active, the same shape as the static cooling is observed. For the quasi-dynamic simulations the two heatsinks are simulated and in this section the developed crystallinity is discussed as well as the effect of coil speed on the crystallinity. As mentioned in section 4.6 for each heatsink two different coil speeds are simulated.

6.5. QUASI-DYNAMIC SIMULATION

From section 4.6 the temperatures of the simulations will be evaluated to see the crystallinity developed during this cooling trajectories applying the analytical model.

6.5.1. KVE3 HEATSINK

20 CM/MIN

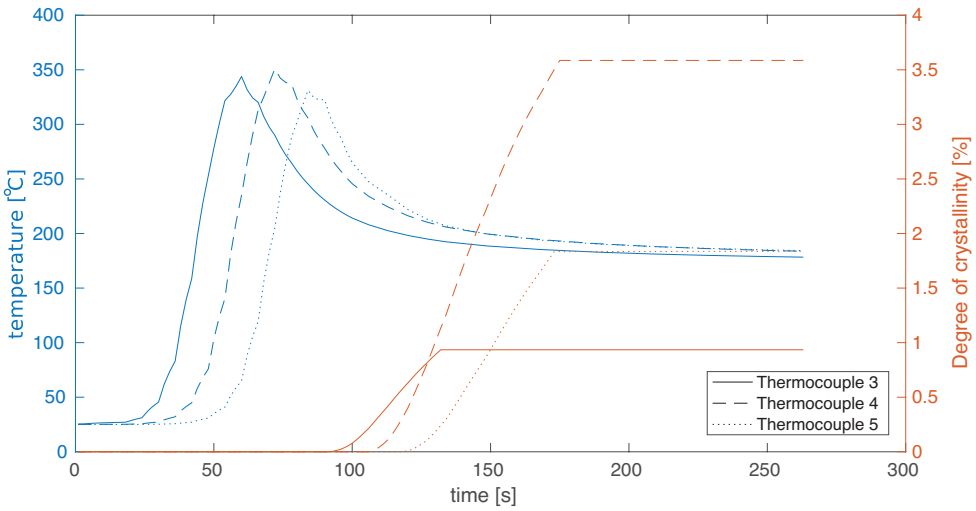

Figure 6.17: Temperature and the degree of crystallinity developed for thermocouple 3, 4 and 5

7.62 CM/MIN

As discussed in section 4.6.1, the cooling of the material is underestimated. If we compare the slopes of the curves, which indicates the cooling rate, the approximation is closer than for the static experiments. For the most accurate prediction of the crystallinity the temperature and the cooling rate at this temperature should correspond to the experiments. As a result the developed crystallinity should at this stage only be considered as being capable to indicated trends. The temperature and the resulting degree of crystallinity for thermocouple 3, 4 and 5 is shown in figure 6.18. It is apparent from this figure that the thermocouple 4 will reach the highest degree of crystallinity as the temperature at the interface is kept most constant during. Thermocouple 5 does not reach the threshold value 354 °C and the will not melt all of this crystals which will indicates that the model can not be correctly applied for this thermocouple. If the thermocouple data is translated to the crystallinity developed at the weld interface, one suspects an weld pool with a maximum degree of crystallinity located somewhere in the centre and two minimum at the outer edges.

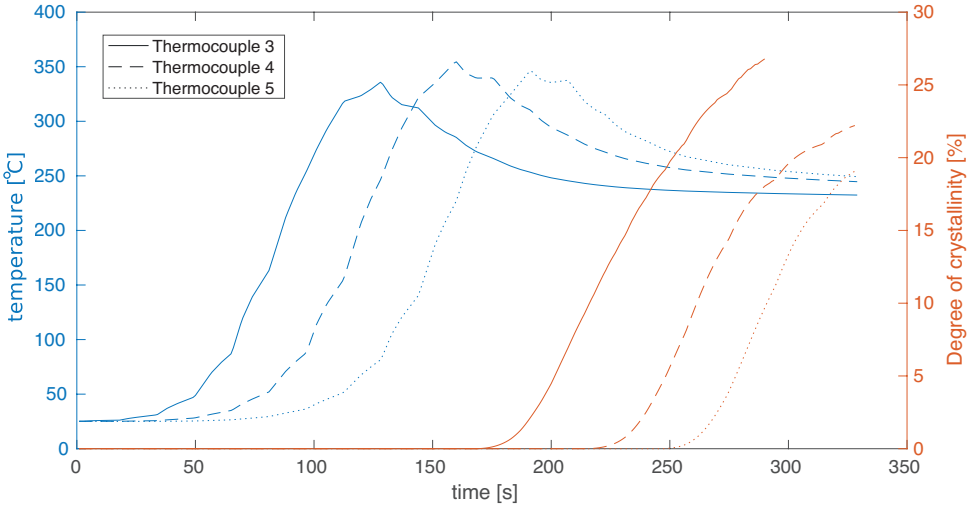

Figure 6.18: Temperature and the degree of crystallinity developed for thermocouple 3, 4 and 5

Figure 6.19 illustrates this crystallization pattern which is developed during dynamic welding. With the coil moving from right to left, the crystallization patten start with a induction period in which de surrounding material is not heated sufficiently the reduce the cooling. As the pattern moves closer towards the end the average temperature of the plate is increased as more energy is added into the material, resulting in a slower cooling rates and a maximum located slightly of centre. At the end, the coil moves away from the centre to the edge of the weld interface, which will lower the energy inserted in the plate as part of the magnetic field will lie outside of the work piece. eventually the coil is even turned of and no extra energy is inserted within the plates reducing the cooling rate and increasing the degree of crystallinity. An other noteworthy observation is the asymmetry across the length of the weld. Which is due to the assymmetry of the set up as shown in figure **??**. The bottom ply of the top plate will cool slower than the top of the bottom plate resulting in a asymmetry.

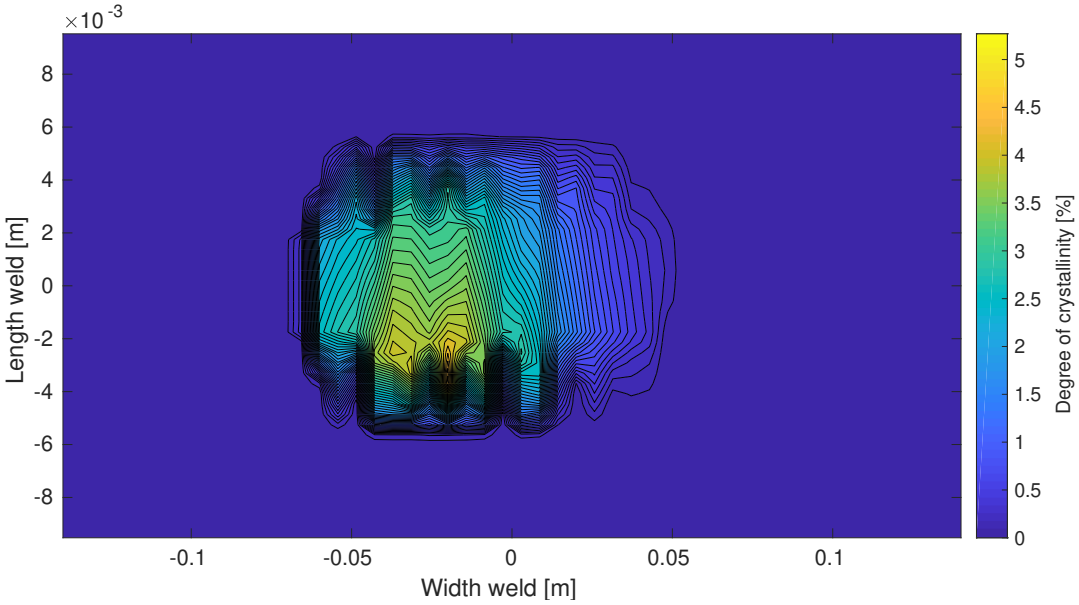

Figure 6.19

6.5.2. KVE4 HEATSINK

intro

20 CM/MIN

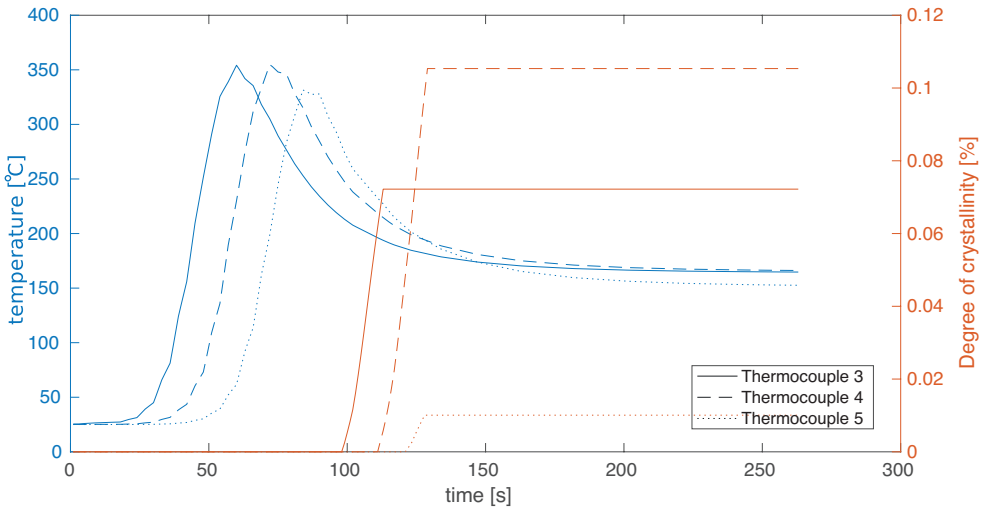

Figure 6.20: Temperature and the degree of crystallinity developed for thermocouple 3, 4 and 5

7.62 CM/MIN

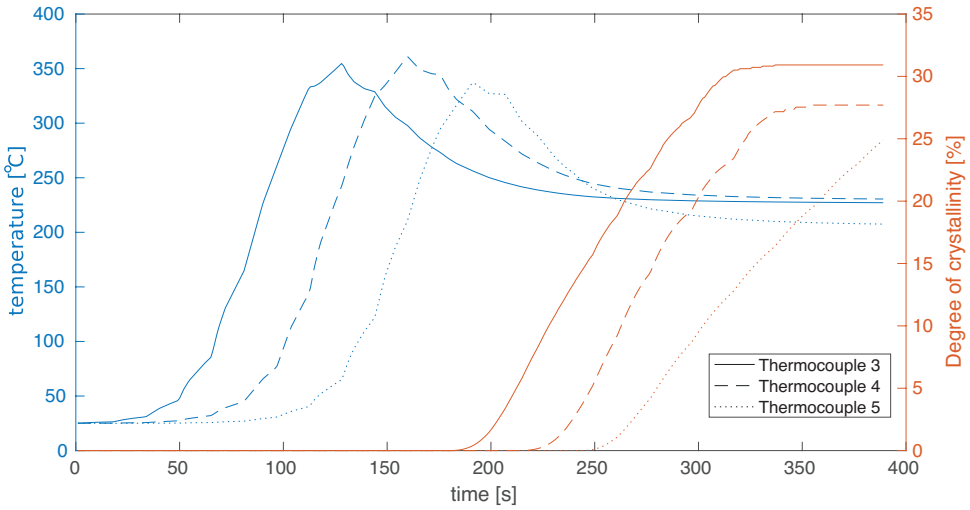

Figure 6.21: Temperature and the degree of crystallinity developed for thermocouple 3, 4 and 5

6.5.3. DYNAMIC CRYSTALLIZATION EXPERIMENTS

To test the effect of different coil speeds and heatsinks on the degree of crystallinity produced during welding the analytical model is applied. Three different dynamic experiments where conducted. The experiments are discussed in section 4.4.2 and this section will primarily focus on the crystallinity.

KVE3 HEATSINK

The welding experiments of section 4.4.1 showed considerably low cooling rates, this is a first indication of a sufficient degree of crystallinity at the weld interface, which was a bit surprising considering the good thermal properties of the KVE3 heatsink. From the graph at figure 6.22 we can see the cooling trajectories of the two thermocouples reaching the melting temperature and the degree of crystallinity which will be produced during cooling. The induction temperature is around 250 °C for both thermocouples. The effect of the magnetic field being turned off as discussed before, will also contribute to a slightly higher prediction for the degree of crystallinity, an upward shift in the temperatures cooling trajectory it will stay longer within the region in which crystallization is possible. Unfortunately the dynamic welding experiments for the KVE 3 heatsink were not successful and further research into the crystallization of PEKK when welding with the KVE 3 heatsink is advised. The surprising slow cooling rate and high degree of crystallinity will be an interesting part to explore more.

KVE4 HEATSINK

The model is only valid if all prior crystallinity is removed before the cooling stage. So only thermocouples which have reached 350 °C will be analysed. First, the faster coil speed will be discussed with the cooling rates shown in figure 4.32. It is apparent from this figure that only a small section of cooling trajectory is cooled below 140 °C/min

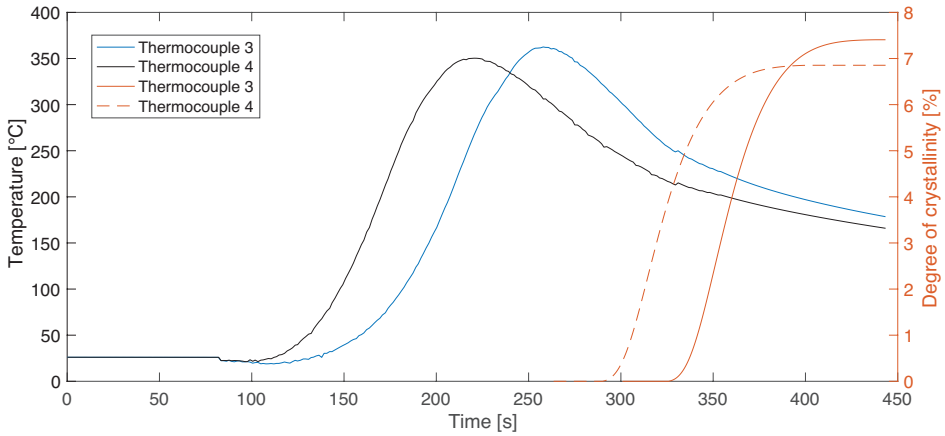

Figure 6.22: Overview of thermocouples located at the weld interface with the KVE3 heatsink and a coil speed of 7.62 cm/min

which indicated limited fractions of crystallinity. Figure 6.23 illustrates at which temperature the onset of crystallinity occurs is and how much crystallinity is developed. As can be seen from the figure there is small degree of crystallinity developed at the weld interface.

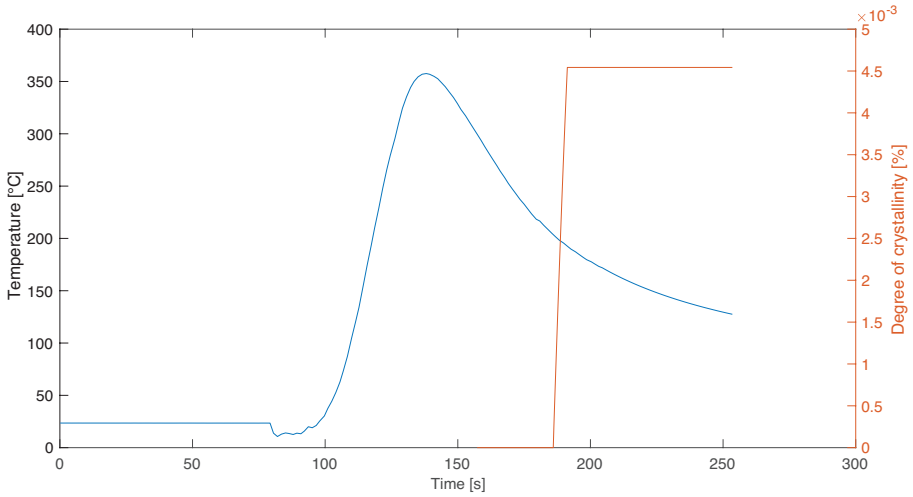

Figure 6.23: Crystallization pattern

Looking at the result shown in figure 4.34, the experiments for the slower coil speeds are more promising. The threshold cooling rates are reached at high temperature. Reaching the threshold value at a higher temperature allows the polymer chains more time to arrange in crystalline regions. Figure 6.24 shows the relation between temperature time and the developed crystallinity of thermocouple number 4. Comparing the figure to figure 6.23, there is a clear difference in broadness of the peaks. The broader peak means a lower cooling rate, which results in an earlier nucleation, increasing the degree of crystallinity. An overview of all the active thermocouples and the degree of crystallinity is

shown in figure 6.25. Spending more time investigation the welding settings which result in a more constant weld temperature will eventually lead to a more even distribution of the crystallinity at the weld interface. Even longer welds are suspected to lead a middle part which will reach a constant distribution of the crystallinity.

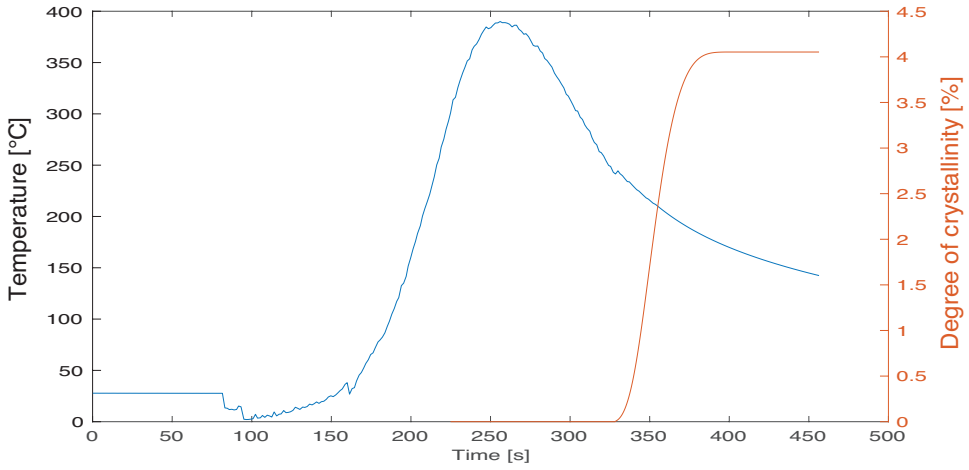

Figure 6.24: Crystallization pattern

6.6. CRYSTALLINITY OF DYNAMIC EXPERIMENTS

DSC can only provide valid results if the temperature or the cooling/heating rates are kept constant. This makes it impossible to find experimental results on the shape of conversion for arbitrary cooling rates. So, the validation of the model can only be done by comparing the predicted end result of crystallinity with the analytical model of the crystallinity obtained after welding experiments. It is not possible to compare the shape of the crystallization curve from the model with experiments, it can only be validated with the end result. The predictions of the analytical model are the crystallinity at this discrete location. DSC experiments need specimens with a weight of 5-15 mg (aiming for a low weight limiting through the thickness crystallinity), so the area of the specimens will cover multiple nodes of the FEA simulation. The resulting crystallinity from the DSC experiments is compared to an average of the crystallinity of all nodes within the specimen area.

The welding experiments with the KVE4 heatsink were used to validate the model. The crystallinity of the thermocouples are compared for both welding configurations. The thermocouples 3, 4 and 5, as described in appendix **??** are used for comparison. The goal is to inspect the crystallinity at the weld interface. Specimens have been prepared by a water jet cutter, this procedure ensured limited addition of heat during the cutting, so that th developed degree of crystallinity would not be perturbed. From the manufactured cylinder two cut outs were made at both sides of the weld interface. Striving for the smallest possible specimens. This is one of the limitations of this method, one will measure a volume of crystals and compare is to a calculation of temperature measured

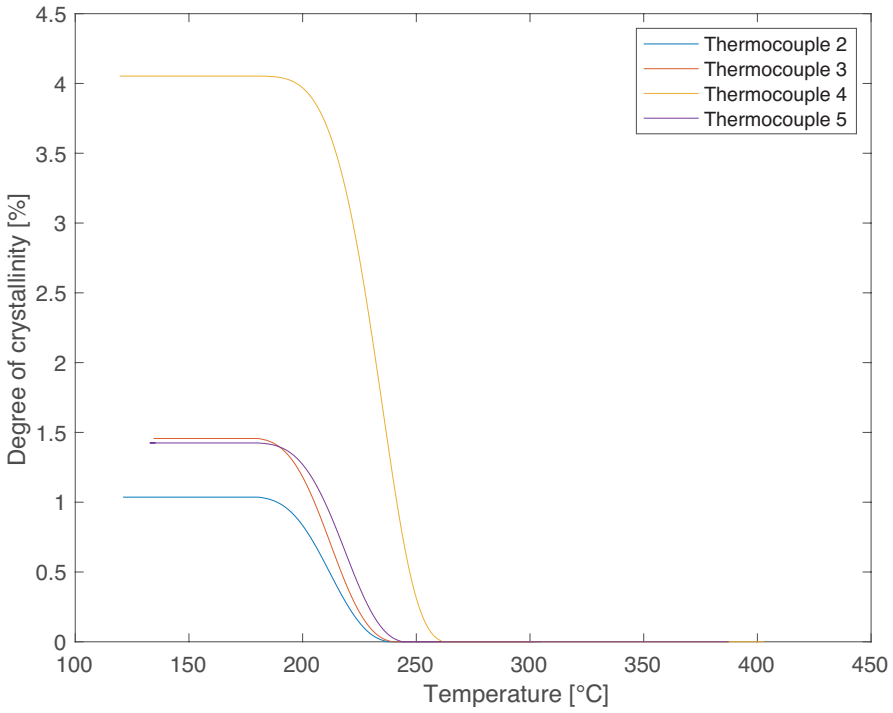

Figure 6.25: Crystallization pattern

at a point.

Thermocouple 4 is discussed firstly as this should be the most interesting thermocouple with a clear difference in degree of crystallinity between both the welds. The degree of crystallinity for the slower welding configuration should be clearly visible during DSC experiments as shown by figure 6.27. The image illustrates two peaks for each welding time. The first peak is the crystallization peak where hight and area is influenced by the cooling of the weld. The second peak is the melting peak and shows the energy required to melt all crystals within the polymer. The degree of crystallinity is calculated with equation (3.4). The physics behind the equation is that during the cooling from the weld crystallinity is formed. To determine this degree of crystallinity formed during cooling from the weld the specimen is heated to 380 °C with a heating rate of 10 °C/min. During this heating the polymer will first crystallize and than the crystals will melt. The area underneath the melting peak (ΔH_m) is the energy required to melt all crystals present in the polymer. The area underneath the crystallization peak(ΔH_c) is the energy required to form the crystals during the heating stage. The difference between $\Delta H_m - \Delta H_c$ is all the energy which is required to melt the crystals formed during cooling after welding. The fiber volume fraction W_f is assumed to be 0.6. This will differ for all samples and cause uncertainty in will result in a inaccuracy of the results.

Now directing the attention to figure 6.26 one can directly see the difference in crystallization peak while the melting peak are more similar. The same trend is observed in

figure 6.27 where the specimen is also located at thermocouple 4 but at the bottom of the weld interface. Table 6.2 presents the different degrees of crystallinity measured by the DSC. What is interesting about the data in this table is that thermocouple 4 follows the trend predicted by the model, with only a minor fraction of crystallinity for the faster coil speed configuration and a higher degree of crystallinity for the slower coil speed. However for the faster welding times the degree of crystallinity at thermocouple 3 and 5 differs from the trends predicted by the analytical model. For thermocouple 5 the specimen did not reach 350 °C ensuring melting of all prior crystallinity, which adds crystallinity produced during manufacturing of the plates and crystallinity during welding to the total. No valid prediction could be made on basis of the thermocouple temperature data. For thermocouple 3 it could be the case that for the top specimen the prior crystallinity was not completely melted during welding. More likely explaining the overall deviation between the analytical model and the DSC experiments is the temperature distribution through the thickness of the specimen as shown in figure 4.12. The figure illustrates that the temperature on top and bottom of the weld interface are lower than the temperature at the weld interface, as described in section 4.2.1 higher temperatures will pass the crystallization region with a lower cooling rate, resulting in higher degree of crystallinity than at the weld interface. The simulation model offers a possibility to observe this trend, which is impossible to observer during experiments. From thermocouple 4, which is the closest approximation of constant weld temperature over the complete length weld interface the same trend is observed as within the model. Adapting the dwell time and or changing the speed of the coil at the start and end will result in a more constant temperature and a more even crystallinity distribution. It is therefore likely that such connections exist between the coil speed and the degree of crystallinity at the weld interface as observed by thermocouple 4. These data must be interpreted with caution because the fiber volume fraction is assumed to be 60 %, Deviation of this fraction within the specimens will result in a different degree of crystallinity.

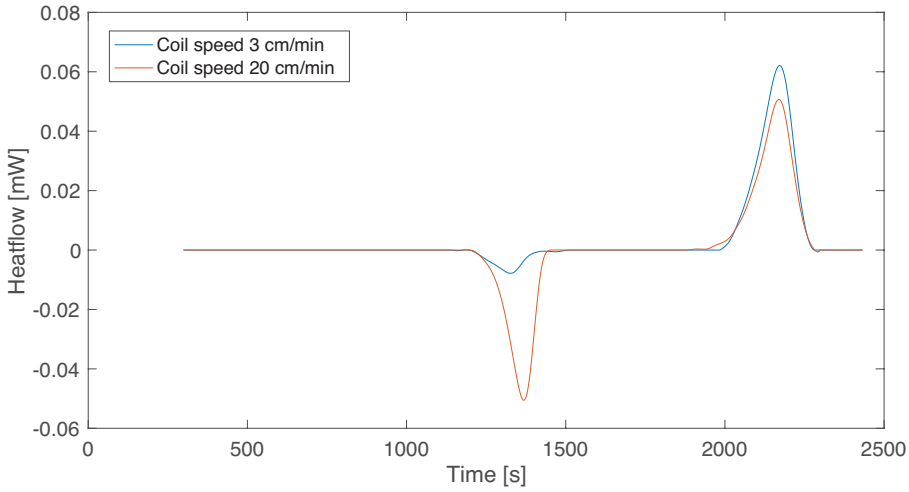

Figure 6.26: Heatflow of the specimen at thermocouple 4 on the top of the weld interface

[1]Specimen was damaged during production
[2]Specimen did not reach 350 °C ensuring melting of all prior crystallinity.

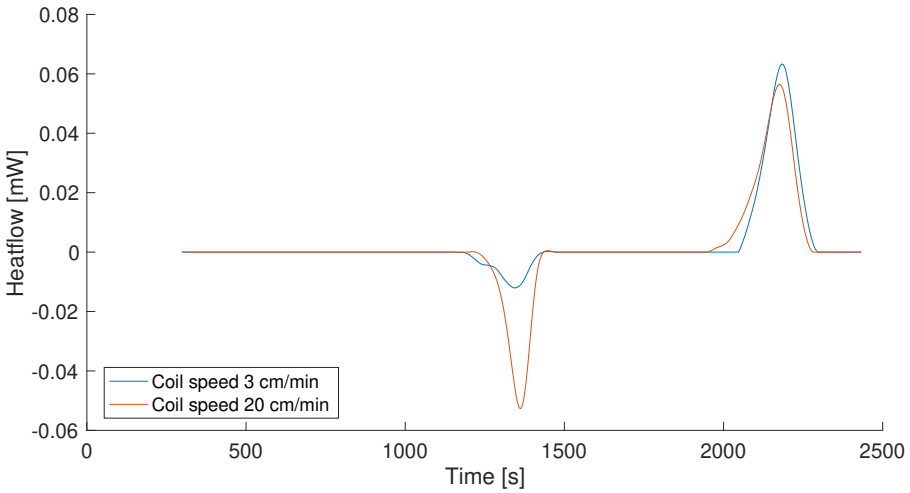

Figure 6.27: Heatflow of the specimen at thermocouple 4 on the bottom of the weld interface

Table 6.2: Overview of degree of crystallinity at different locations at the weld interface for different welding configurations

Coil speed	**Location at weld interface**	**Total crystallinitiy at Tc 3 [%]**	**Total crystallinitiy at Tc 4 [%]**	**Total crystallinitiy at Tc 5 [%]**
20 cm/min	Top	11.9	3.4	15.5 [2]
	Bottom	5.4	3.0	- [1]
7 cm/min	Top	- [1]	13.5	8.2
	Bottom	11.3	11.4	9.5

THROUGH THE THICKNESS CRYSTALLINITY

7

DISCUSSION

7.1. MATCH WITH PREVIOUS LITERATURE

Induction welding for composites materials is in the early stages of development when compared to the induction welding process for metals, where the physics of the process is better known. The induction welding process for composites is still reliant on a trial and error, but an increase in performance and consistency of the process requires more understanding of the physics. One of these under investigated fields is the crystallization of semi-crystalline polymers during induction welding.

This research is conducted to fill the gap about the crystallization of PEKK during induction welding. One of the most interesting properties of PEKK for its the manufactures is that they can lower the melting temperature by chancing its chemical composition, while the glass temperature stays almost constant. Up to the glass temperature, polymers have useful mechanical properties. This feature of PEKK allows manufactures to produce low melting PEKK, which requires less energy to produce a part. These lower melting PEKK have a side effect, slower crystallization rates. The slow crystallization rate and the fast cooling rates observed during induction induction welding require better understanding of the process.

we noted that prior research into the field of crystallization of polymers and predicting crystallization rates is mainly aimed towards DSC like conditions (constant temperature or constant cooling rate). These findings are of limited use for the industry, as the industry more often encounters non constant cooling trajectories. This leads to the research question: “Can we predict the crystallinity for an arbitrary cooling trajectory?”.

7.2. COMMENTARY ON THE FINDINGS

This first attempt at predicting the crystallinity for a given cooling is found to be capable of indicating the order of magnitude and predicting the trends observed during induc-

tion welding experiments. Due to the novelty of the model numerous assumptions had to be made, of which some of them still required more research. However, the capability to observe trends and make acceptable predictions is already valuable for optimizing the welding process. It was found that attention within the induction welding process was mainly aimed at the heating stage with the goal of reaching the desired temperature, the cooling stage and the resulting crystallinity was mainly neglected. This observation was found within the multi physics simulations developed by KVE as well. The simulations were found to predict the maximum temperature within a 10 % bound, but the cooling stage shows larger deviation. It predicts slower cooling rates than observed during the experiments. This leads to an overprediction of the degree of crystallinity when applying the analytical model to the simulations. Although the simulations were not fully predictive considering the cooling, the trends observed and the capability to investigate what is happening within the material, makes the simulations a valuable addition towards increased understanding of the induction welding process. Since it is common practice within the company KVE to strive, to speed up the welding process, there was a tendency to highest conductive heatsinks, which prevent degradation of the top surface while allowing to introduce a high degree of energy within the composites. Our simulations showed that for certain welding set ups lower conductive heatsinks would result in lower cooling rates, while preventing degradation of the top surface. This increased the crystallinity at the weld interface without altering the welding times.

A second observation found by the simulations was that longer welding times or slower coil speeds, result in a more even temperature distribution and slower cooling rates. This as a result produced a higher degree of crystallinity. The experiments showed the same trends; slower welding produced a more crystallinity at the weld interface. One unanticipated finding was that the cooling with the higher conductive heatsink KVE3 for dynamic welding resulted in lower cooling rates compared to the lower conductive KVE4 heatsink. At this stage of understanding, I believe this could be due to, first, the difference in size of both heatsinks used. And second, the way both heatsinks are embedded within the tooling station. The KVE4 heatsink is kept in place by aluminium tooling, which will subtract heat form the heatsink, whereas the KVE3 heatsink is surrounded by PEEK, which will isolate the material. As a consequence this causes the heatsink to fill up with heat, losing its capability to cool as sufficient as desired.

Investigating the crystallinity for the dynamic experiments, the trends predicted by the analytical model are observed in the experiments. Slower welding resulted in a higher degree of crystallinity at the weld interface. The measurements of the crystallinity found to be a sufficiently larger degree of crystallinity. This difference was much larger than the measurement done in a more conditioned environment. This is due to the fact that the input value for the analytical model is the temperature measured by thermocouples, which is the temperature at a discreet point, whereas measurement of the crystallinity of the dynamic welds are conducted on a volume of PEKK. Within these volumes different cooling rates are observed, which will result in different degree of crystallinity. The simulations were checked to see if these gradients were present in the material, which helped to explain these differences.

7.3. LIMITATIONS

The limitations of the present studies naturally included, the small sample size used during the experiments. This small sample sized allowed room for errors, which in hindsight, evaluating the experiments will most likely have occurred. Another limitation in the analytical model involves the issue of the fiber volume fraction. All experiments of the analytical model were conducted on one specimen so the fiber volume fraction was constant between these experiments. However, the degree of crystallinity is calculated assuming a 60 % fiber volume fraction, leading to the maximum degree of crystallinity for different cooling rates is used in the model to analyze non constant cooling rates. Deviation of this fraction will cause errors in the predictions and not knowing the precise fiber volume fraction makes a conclusive validation of the analytical model hard. These limitations are of major importance in interpreting the predictions, as well as the validation of the model. The analytical model is based on a small sample size and increasing the sample size will greatly increase the accuracy of the model.

7.4. PRACTICAL IMPLICATION

This explanatory study provides insight into the crystallization rate of polymers for an arbitrary temperature trajectory and allows direct implication into the induction welding process. These findings increases the understanding of the process and helps to optimize the weld quality. The changes in the induction welding process resulted in a high degree of crystallinity at the weld interface. I believe that the developed analytical model adds knowledge to an underexposed field of induction welding. This first attempt to predict the crystallinity for non constant cooling shows promising results and I have confidence that the accuracy can be increased by addressing the limitations mentioned above. Recommendation for further research is to investigate the effect of the degree of crystallinity on the mechanical properties of the weld. An other interesting development would concern the difference in material properties of semi crystalline PEKK and the amorphous PEKK. The analytical model could be simultaneously applied with the multi physics simulations, making the material properties dependent on temperature and crystalline fraction. An other interesting development would be to explore the validity of the analytical model for other slow crystallization polymers.

8

CONCLUSION

PEKK is a slow crystallization semi-crystalline polymers with respect to degree of crystallinity and crystallization rates. In the present research a new model was developed to predict the degree of crystallinity for a non-constant cooling rate. The model depends on temperature, the cooling rate and the degree of crystallinity. The analytical model is capable of predicting the observed trends and the degree of crystallinity within a 25% bound. These predictions are noteworthy, especially when considering the number of assumptions required and the small sample sizes used. This shows the promising capability of the analytical model. The model is not limited to constant cooling rates and because of that it can directly be applied to evaluate the induction welding process. In the literature and industry, attention within induction welding is mainly aimed at the heating stage and the cooling of the work piece is often neglected. This research tries to fill in this gap by evaluating the cooling and the resulting crystallinity. It was found that the present induction welding setting only resulted in minor fractions of crystallinity ($< 3\%$) and that by decreasing the coil speed the degree of crystallinity could be increased around the desired 10 % degree of crystallinity. Coupling the analytical model to the multi physics simulations allowed a deeper investigation of the crystallinity developed within the composites, which is very hard to investigate by any measurement device. This research advances on past research about the topic because it extends predictions on semi-crystalline polymer crystallization to non-constant cooling which provides with direct implication to the manufacturing process. This directly illustrates the importance of the research. The analytical model directly allows validation of the induction welding process in terms of degree of crystallinity, which would otherwise consist out of time-consuming and expensive experimental measurements.

A

APPENDIX

A.1. CHAPTER 3

A.1.1. MANUFACTURING COUPONS

A.2. COOLING TRAJECTORIES OF COOLING RATES WITH THE KVE4 HEATSINK

The next section provides a overview of all the cooling trajectories and cooling rates obtained with the experiments and the and a comparison with the computational model.

A.2.1. COOLING TRAJECTORIES

A.2.2. COOLING RATES

A

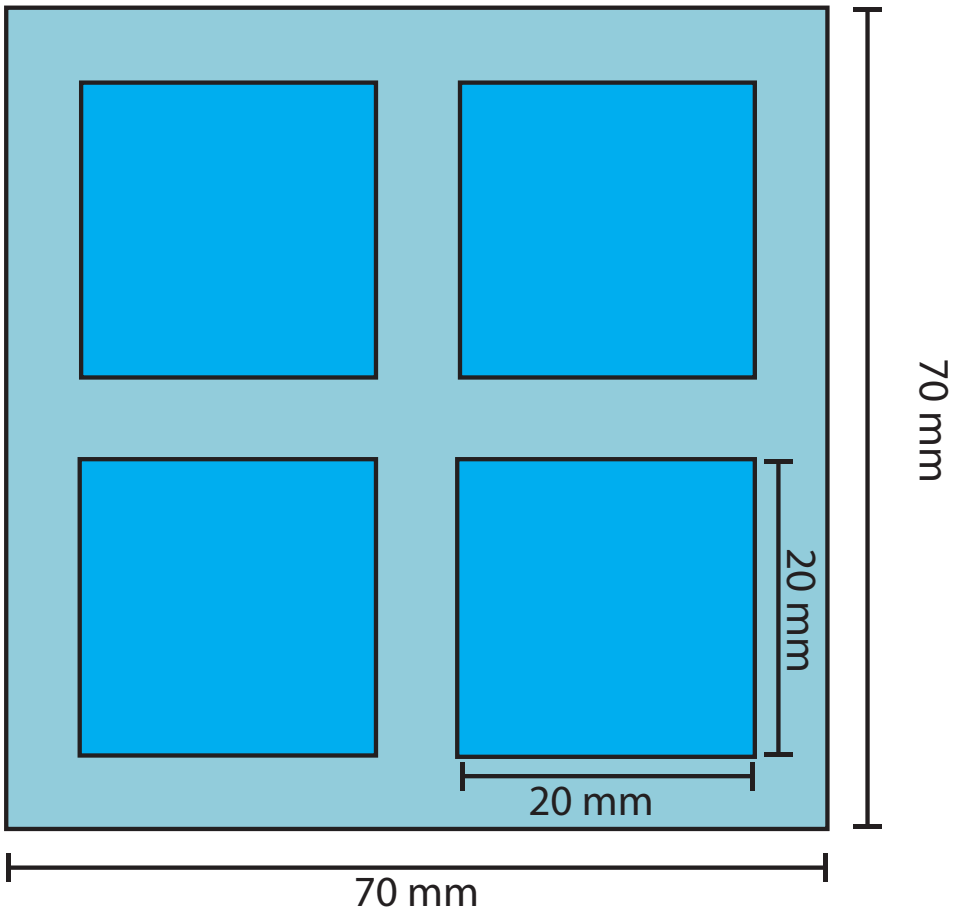

Figure A.1: Coupon manufacturing

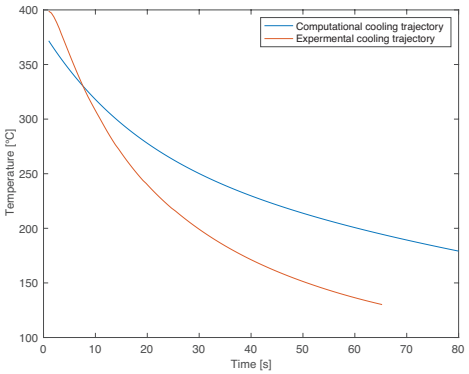

(a) Cooling trajectory after welding 17 seconds

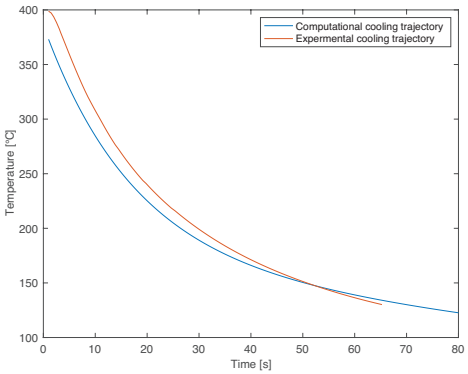

(b) Cooling trajectory after welding 22 seconds

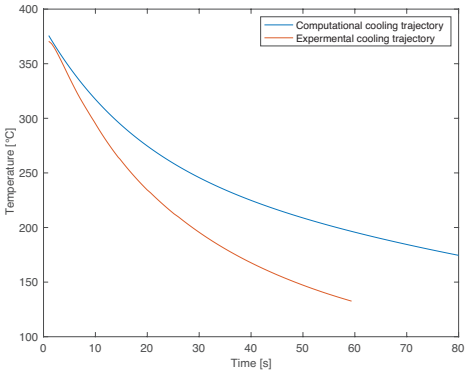

(a) Cooling trajectory after welding 17 seconds

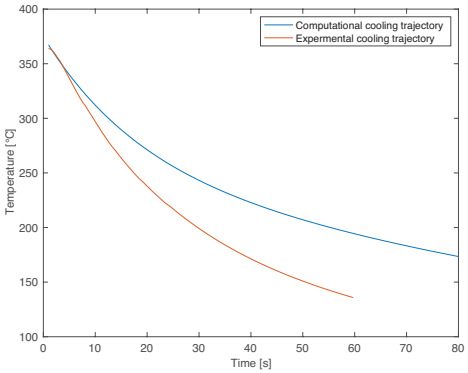

(b) Cooling trajectory after welding 22 seconds

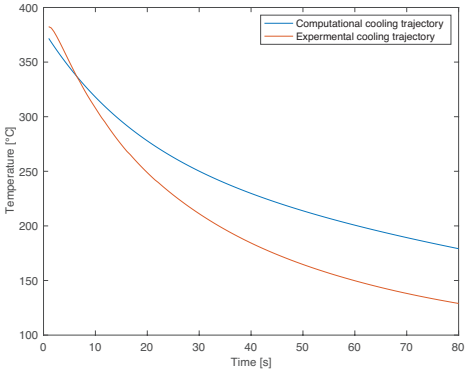

(a) Cooling trajectory after welding 17 seconds

A

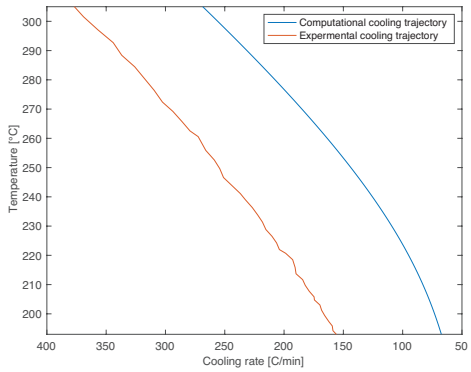

(a) Cooling trajectory after welding 17 seconds

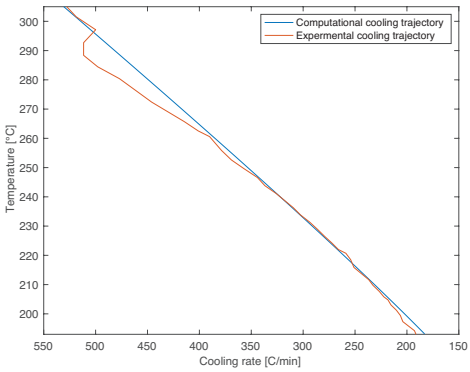

(b) Cooling trajectory after welding 22 seconds

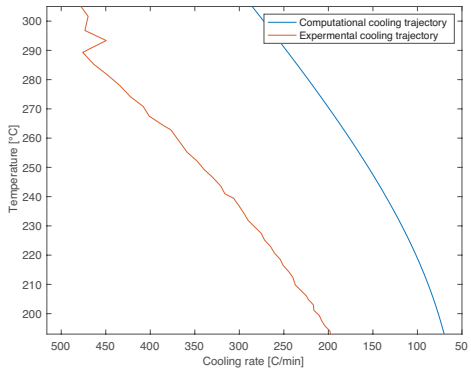

(a) Cooling trajectory after welding 27 seconds

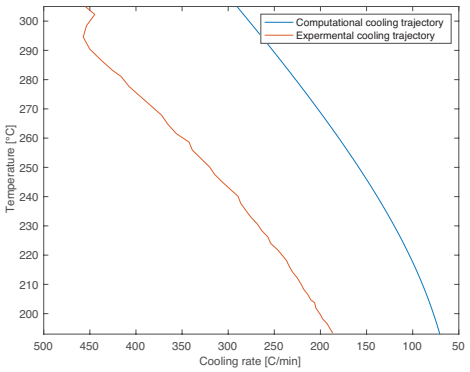

(b) Cooling trajectory after welding 30 seconds

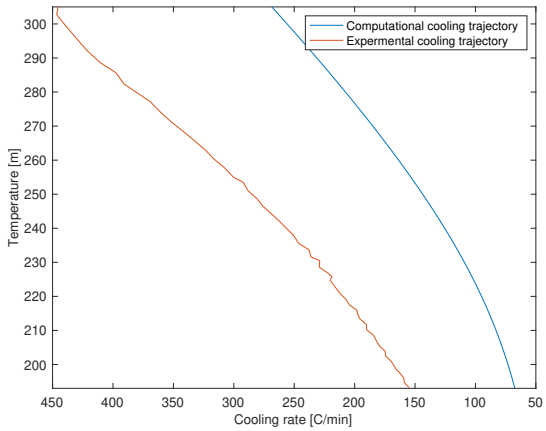

(a) Cooling trajectory after welding 34 seconds

REFERENCES

[1] Pan Zhao, Bijan Shirinzadeh, Yaoyao Shi, Simeon Cheuk, and Leon Clark. Multi-pass layup process for thermoplastic composites using robotic fiber placement. *Robotics and Computer-Integrated Manufacturing*, 49:277–284, 2018.

[2] M.H.J. Doldersum. Industrialization of thermoplastic control surfaces. *Tech. rep. GKN Fokker Aerostructures*, 2014.

[3] Stephanie M Todd. Joining thermoplastic composites. *Society for the Advancement of Material and Process Engineering,*, pages 383–392, 1990.

[4] Natassia Lona Batista, Philippe Olivier, Gérard Bernhart, Mirabel Cerqueira Rezende, and Edson Cocchieri Botelho. Correlation between degree of crystallinity, morphology and mechanical properties of pps/carbon fiber laminates. *Materials Research*, 19(1):195–201, 2016.

[5] Mark Holmes. Aerospace looks to composites for solutions. *Reinforced Plastics*, 61 (4):237–241, 2017.

[6] Micheal H Topping. Electromagnetic welding of thermoplastics and specific design criteria. Technical report, SAE Technical Paper, 1994.

[7] Vijay K Stokes. Experiments on the induction welding of thermoplastics. *Polymer Engineering & Science*, 43(9):1523–1541, 2003.

[8] Valery Rudnev, Don Loveless, and Raymond L Cook. *Handbook of induction heating*. CRC press, 2017.

[9] Richard E Haimbaugh. *Practical induction heat treating*. ASM international, 2001.

[10] Robert M Del Vecchio, Robert Del Vecchio, Bertrand Poulin, Pierre T Feghali, Dilipkumar M Shah, and Rajendra Ahuja. *Transformer Design Principles With Applications 3e: With Applications to Core-Form Power Transformers*. CRC press, 2017.

[11] Stanley Zinn and SL Semiatin. Coil design and fabrication: basic design and modifications. *Heat treating*, 12(3):32–36, 1988.

[12] AK Miller, Calvin Chang, ALEXANDER PAYNE, MICHA GUR, and ERIK MENZEL. The nature of induction heating in graphite-fiber, polymer-matrix composite materials. *SAMPE journal*, 26:37–54, 1990.

[13] Alan K Miller and Wendy Lin. Joining of composite materials by induction heating, August 31 1993. US Patent 5,240,542.

[14] John Border and Rik Salas. Induction heated joining of thermoplastic composites without metal susceptors. *Tomorrow's Materials: Today.*, 34:2569–2578, 1989.

[15] Shridhar Yarlagadda, Hee June Kim, John W Gillespie Jr, Nicholas B Shevchenko, and Bruce K Fink. A study on the induction heating of conductive fiber reinforced composites. *Journal of composite materials*, 36(4):401–421, 2002.

[16] Wendy Lin, Alan K Miller, and Oscar Buneman. Predictive capabilities of an induction heating model for complex-shape graphite fiber/polymer matrix composites. In *24th International SAMPE Technical Conference*, volume 24, pages T606–T620, 1992.

[17] JW Gillespie Jr, RL McCullough, and BK Fink. Induction heating of cross-ply carbon-fiber composites. *ANTEC 92–Shaping the Future.*, 2:2106–2109, 1992.

[18] Daniel Tan, Lili Zhang, Qin Chen, and Patricia Irwin. High-temperature capacitor polymer films. *Journal of electronic materials*, 43(12):4569–4575, 2014.

[19] Bruce K Fink, Roy L McCullough, and John W Gillespie Jr. A model to predict the through-thickness distribution of heat generation in cross-ply carbon-fiber composites subjected to alternating magnetic fields. *Composites science and technology*, 55(2):119–130, 1995.

[20] Shoukai Wang, Daniel P Kowalik, and DDL Chung. Effects of the temperature, humidity, and stress on the interlaminar interface of carbon fiber polymer-matrix composites, studied by contact electrical resistivity measurement. *The Journal of Adhesion*, 78(2):189–200, 2002.

[21] A Fosbury, Shoukai Wang, YF Pin, and DDL Chung. The interlaminar interface of a carbon fiber polymer-matrix composite as a resistance heating element. *Composites Part A: Applied Science and Manufacturing*, 34(10):933–940, 2003.

[22] E Karamuk, ED Wetzel, and JW Gillespie Jr. Modeling and design of induction bonding process for infrastructure rehabilitation with composite materials. *Society of Plastics Engineers(USA),*, pages 1239–1243, 1995.

[23] R Rudolf, P Mitschang, and M Neitzel. Induction heating of continuous carbon-fibre-reinforced thermoplastics. *Composites Part A: Applied Science and Manufacturing*, 31(11):1191–1202, 2000.

[24] Director Leonard J. Bond. Depth of penetration and current density, 2004. URL http://www.nde-ed.org/EducationResources/CommunityCollege/EddyCurrents/Physics/depthcurrentdensity.html.

[25] RP Wool, B-L Yuan, and OJ McGarel. Welding of polymer interfaces. *Polymer Engineering & Science*, 29(19):1340–1367, 1989.

[26] T Zach, J Lew, TH North, and RT Woodhams. Joining of high strength oriented polypropylene using electromagnetic induction bonding and ultrasonic welding. *Materials science and technology*, 5(3):281–287, 1989.

[27] Dustin Veazey, Tim Hsu, and Enrique D Gomez. Next generation high-performance carbon fiber thermoplastic composites based on polyaryletherketones. *Journal of Applied Polymer Science*, 134(6), 2017.

[28] Stephen Z. D. Cheng, Rong-Ming Ho, Benjamin S. Hsiao, and Kenncorwin H. Gardner. Polymorphism and crystal structure identification in poly(aryl ether ketone ketone)s. *Macromolecular Chemistry and Physics*, 197(1):185–213, jan 1996.

[29] Parina Patel, Terence Richard Hull, and Colin Moffatt. Peek polymer flammability and the inadequacy of the ul-94 classification. *Fire and Materials*, 36(3):185–201, 2012.

[30] Rogerio L Mazur, Pedro C Oliveira, Mirabel C Rezende, and Edson C Botelho. Environmental effects on viscoelastic behavior of carbon fiber/pekk thermoplastic composites. *Journal of Reinforced Plastics and Composites*, 33(8):749–757, 2014.

[31] James C Seferis. Polyetheretherketone (peek): Processing-structure and properties studies for a matrix in high performance composites. *Polymer composites*, 7(3): 158–169, 1986.

[32] DF Williams, A McNamara, and RM Turner. Potential of polyetheretherketone (peek) and carbon-fibre-reinforced peek in medical applications. *Journal of materials science letters*, 6(2):188–190, 1987.

[33] AR Boccaccini, C Peters, JA Roether, D Eifler, SK Misra, and EJ Minay. Electrophoretic deposition of polyetheretherketone (peek) and peek/bioglass® coatings on niti shape memory alloy wires. *Journal of Materials Science*, 41(24):8152–8159, 2006.

[34] Chris N. Velisaris and James C. Seferis. Crystallization kinetics of polyetheretherketone (peek) matrices. *Polymer Engineering and Science*, 26(22):1574–1581, dec 1986.

[35] P Avakian, KH Gardner, and RR Matheson Jr. A comment on crystallization in pekk and peek resins. *Journal of Polymer Science Part C: Polymer Letters*, 28(8):243–246, 1990.

[36] Mark A Lamontia and MARK B Gruber. Limitations on mechanical properties in thermoplastic laminates fabricated by two processes: automated thermoplastic tape placement and filament winding. In *26th SAMPE Europe conference, Paris*, 2005.

[37] Xavier Tardif, Baptiste Pignon, Nicolas Boyard, Jürn W.P. Schmelzer, Vincent Sobotka, Didier Delaunay, and Christoph Schick. Experimental study of crystallization of PolyEtherEtherKetone (PEEK) over a large temperature range using a nano-calorimeter. *Polymer Testing*, 36:10–19, jun 2014.

[38] DJ Blundell and AB Newton. Variations in the crystal lattice of peek and related para-substituted aromatic polymers: 2. effect of sequence and proportion of ether and ketone links. *Polymer*, 32(2):308–313, 1991.

[39] JN Hay, JI Langford, and JR Lloyd. Variation in unit cell parameters of aromatic polymers with crystallization temperature. *Polymer*, 30(3):489–493, 1989.

[40] Alain Jonas, Roger Legras, and J-P Issi. Differential scanning calorimetry and infrared crystallinity determinations of poly (aryl ether ether ketone). *Polymer*, 32(18): 3364–3370, 1991.

[41] Richard H Boyd. Relaxation processes in crystalline polymers: experimental behaviour—a review. *Polymer*, 26(3):323–347, 1985.

[42] Douglass S Kalika and Rajendra K Krishnaswamy. Influence of crystallinity on the dielectric relaxation behavior of poly (ether ether ketone). *Macromolecules*, 26(16): 4252–4261, 1993.

[43] RK Krishnaswamy and DS Kalika. Glass transition characteristics of poly (aryl ether ketone ketone) and its copolymers. *Polymer*, 37(10):1915–1923, 1996.

[44] Lin Jin, Jerry Ball, Tim Bremner, and Hung-Jue Sue. Crystallization behavior and morphological characterization of poly (ether ether ketone). *Polymer*, 55(20): 5255–5265, 2014.

[45] KennCorwin H. Gardner, Benjamin S. Hsiao, and Katherine L. Faron. Polymorphism in poly(aryl ether ketone)s. *Polymer*, 35(11):2290–2295, may 1994.

[46] Raymond J Abraham and Ian S Haworth. Molecular modelling of poly (aryl ether ketones): 2. chain packing in crystalline pek and peek. *Polymer*, 32(1):121–126, 1991.

[47] Ike Y Chang. Pekk as a new thermoplastic matrix for high-performance composites. *SAMPE Q.;(United States)*, 19(4), 1988.

[48] KennCorwin H Gardner, Benjamin S Hsiao, Robert R Matheson, and Barbara A Wood. Structure, crystallization and morphology of poly (aryl ether ketone ketone). *Polymer*, 33(12):2483–2495, jan 1992.

[49] Gunilla MK Ostberg and James C Seferis. Annealing effects on the crystallinity of polyetheretherketone (peek) and its carbon fiber composite. *Journal of Applied Polymer Science*, 33(1):29–39, 1987.

[50] Youngchul Lee and Roger S Porter. Crystallization of poly (etheretherketone)(peek) in carbon fiber composites. *Polymer Engineering & Science*, 26(9):633–639, 1986.

[51] B.S. Hsiao Y.I. Chang. Thermal properties of high performance thermoplastic composites based on poly(ether ketone ketone) (pekk). *36th Int. SAMPE symp*, page 1587–1601, 1991.

[52] P Weigel. Macromolecular physics. vol. 3: Crystal melting. von bernhard wunderlich. *Acta Polymerica*, 32(7):413, 1980.

[53] DJ Blundell and BN Osborn. The morphology of poly (aryl-ether-ether-ketone). *Polymer*, 24(8):953–958, 1983.

[54] Solvay company. APC (PEKK-FC). Technical report, PEKK-FC THERMOPLASTIC POLYMER PREPREG, 2017.

[55] A Keller. A note on single crystals in polymers: evidence for a folded chain configuration. *Philosophical Magazine*, 2(21):1171–1175, 1957.

[56] PH Till Jr. The growth of single crystals of linear polyethylene. *Journal of Polymer Science*, 24(106):301–306, 1957.

[57] George D Wignall. Semicrystalline polymers: Chain conformation and folging. Technical report, Oak Ridge National Laboratory (ORNL), Oak Ridge, TN (United States). High Flux Isotope Reactor (HFIR), 2016.

[58] K Armitstead, G Goldbeck-Wood, and A Keller. Polymer crystallization theories. In *Macromolecules: synthesis, order and advanced properties*, pages 219–312. Springer, 1992.

[59] RF Boyer. Dependence of mechanical properties on molecular motion in polymers. *Polymer Engineering & Science*, 8(3):161–185, 1968.

[60] EA DiMarzio and JH Gibbs. Chain stiffness and the lattice theory of polymer phases. *The Journal of Chemical Physics*, 28(5):807–813, 1958.

[61] JW Gibbs. The collected works, vol. 1, longmans, green and co. *New York*, 1928.

[62] Luis A Marky and Kenneth J Breslauer. Calculating thermodynamic data for transitions of any molecularity from equilibrium melting curves. *Biopolymers: Original Research on Biomolecules*, 26(9):1601–1620, 1987.

[63] D Turnbull and J Co Fisher. Rate of nucleation in condensed systems. *The Journal of chemical physics*, 17(1):71–73, 1949.

[64] M Volmer. M. volmer and a. weber, z. phys. chem. 119, 277 (1926). *Z. Phys. Chem.*, 119:277, 1926.

[65] Richard Becker and Werner Döring. Kinetische behandlung der keimbildung in übersättigten dämpfen. *Annalen der Physik*, 416(8):719–752, 1935.

[66] Lawrence A Wood and Norman Bekkedahl. Crystallization of unvulcanized rubber at different temperatures. *Journal of Applied Physics*, 17(5):362–375, 1946.

[67] T. Choupin, B. Fayolle, G. Régnier, C. Paris, J. Cinquin, and B. Brulé. Isothermal crystallization kinetic modeling of poly(etherketoneketone) (PEKK) copolymer. *Polymer*, 111:73–82, feb 2017.

[68] M Imai, K Kaji, and T Kanaya. Orientation fluctuations of poly (ethylene terephthalate) during the induction period of crystallization. *Physical review letters*, 71 (25):4162, 1993.

[69] Kostas Ch Daoulas, Marcus Müller, Juan J De Pablo, Paul F Nealey, and Grant D Smith. Morphology of multi-component polymer systems: single chain in mean field simulation studies. *Soft Matter*, 2(7):573–583, 2006.

[70] JI Lauritzen and John D Hoffman. Theory of formation of polymer crystals with folded chains in dilute solution. *J. Res. Natl. Bur. Stand. A*, 64(1):73102, 1960.

[71] John D Hoffman. Regime iii crystallization in melt-crystallized polymers: the variable cluster model of chain folding. *Polymer*, 24(1):3–26, 1983.

[72] John D Hoffman, G Thomas Davis, and John I Lauritzen. The rate of crystallization of linear polymers with chain folding. In *Treatise on solid state chemistry*, pages 497–614. Springer, 1976.

[73] FC Frank. Nucleation-controlled growth on a one-dimensional growth of finite length. *Journal of Crystal Growth*, 22(3):233–236, 1974.

[74] Daxaben Patel and DC Bassett. On spherulitic crystallization and the morphology of melt-crystallized poly (4-methylpentene-1). *Proc. R. Soc. Lond. A*, 445(1925): 577–595, 1994.

[75] John D Hoffman. Regime iii crystallization in melt-crystallized polymers: the variable cluster model of chain folding. *Polymer*, 24(1):3–26, 1983.

[76] JJ Point. A new theoretical approach of the secondary nucleation at high supercooling. *Macromolecules*, 12(4):770–775, 1979.

[77] Paul J Phillips. Polymer crystals. *Reports on Progress in Physics*, 53(5):549, 1990.

[78] JD Hoffman, JI Lauritzen, E Passaglia, GS Ross, LJ Frolen, and JJ Weeks. Kinetics of polymer crystallization from solution and the melt. *Kolloid-Zeitschrift und Zeitschrift für Polymere*, 231(1-2):564–592, 1969.

[79] JJ Point, M Ch Colet, and M Dosiere. Experimental criterion for the crystallization regime in polymer crystals grown from dilute solution: possible limitation due to fractionation. *Journal of Polymer Science Part B: Polymer Physics*, 24(2):357–388, 1986.

[80] G Ungar and A Keller. Inversion of the temperature dependence of crystallization rates due to onset of chain folding. *Polymer*, 28(11):1899–1907, 1987.

[81] John D Hoffman, Robert L Miller, Herve Marand, and Daniel B Roitman. Relationship between the lateral surface free energy. sigma. and the chain structure of melt-crystallized polymers. *Macromolecules*, 25(8):2221–2229, 1992.

[82] David M Sadler and George H Gilmer. Selection of lamellar thickness in polymer crystal growth: a rate-theory model. *Physical Review B*, 38(8):5684, 1988.

[83] Shang-Lin Gao and Jang-Kyo Kim. Cooling rate influences in carbon fibre/peek composites. part 1. crystallinity and interface adhesion. *Composites Part A: Applied science and manufacturing*, 31(6):517–530, 2000.

[84] AJ Waddon, MJ Hill, A Keller, and DJ Blundell. On the crystal texture of linear polyaryls (peek, pek and pps). *Journal of Materials Science*, 22(5):1773–1784, 1987.

[85] Glenn P Desio and Ludwig Rebenfeld. Crystallization of fiber-reinforced poly (phenylene sulfide) composites. i. experimental studies of crystallization rates and morphology. *Journal of applied polymer science*, 44(11):1989–2001, 1992.

[86] Benjamin S Hsiao, Ike Y Chang, and Bryan B Sauer. Isothermal crystallization kinetics of poly(ether ketone ketone) and its carbon-fibre-reinforced composites. *Polymer*, 32(15):2799–2805, jan 1991.

[87] A Arzak, JI Eguiazabal, and J Nazabal. Effect of annealing on the properties of poly (ether ether ketone). *Polymer Engineering & Science*, 31(8):586–591, 1991.

[88] Elodie Bugnicourt, Patrizia Cinelli, Andrea Lazzeri, and Vera Alejandra Alvarez. Polyhydroxyalkanoate (pha): Review of synthesis, characteristics, processing and potential applications in packaging. *Express Polymer Letters*, 2014.

[89] Annette C Renouf-Glauser, John Rose, David F Farrar, and Ruth Elizabeth Cameron. The effect of crystallinity on the deformation mechanism and bulk mechanical properties of plla. *Biomaterials*, 26(29):5771–5782, 2005.

[90] Michael J Doyle. On the effect of crystallinity on the elastic properties of semicrystalline polyethylene. *Polymer Engineering & Science*, 40(2):330–335, 2000.

[91] Michael J. Troughton. Chapter 11 - induction welding. In *Handbook of Plastics Joining (Second Edition)*, pages 113 – 120. William Andrew Publishing, Boston, second edition edition, 2009.

[92] Roger J Wise. *Thermal welding of polymers*. Woodhead Publishing, 1999.

[93] Pierre-Giles de Gennes. Reptation of a polymer chain in the presence of fixed obstacles. *The journal of chemical physics*, 55(2):572–579, 1971.

[94] Donald S Dugdale. Yielding of steel sheets containing slits. *Journal of the Mechanics and Physics of Solids*, 8(2):100–104, 1960.

[95] Y-Q Xue, TA Tervoort, and PJ Lemstra. Welding behavior of semicrystalline polymers. 1. the effect of nonequilibrium chain conformations on autoadhesion of uhmwpe. *Macromolecules*, 31(9):3075–3080, 1998.

[96] Christan Bonten and Ernst Schmachtenberg. A new hypothesis to describe the mechanisms acting in a welded joint of semicrystalline thermoplastics. *Polymer Engineering & Science*, 41(3):475–483, 2001.

[97] Deutscher Verband für Schweißen und Verwandte Verfahren. *Taschenbuch DVS-Merkblätter und-Richtlinien: Fügen von Kunststoffen: Ausbildung und Prüfung/erarb. von der Arbeitsgruppe W4" Fügen von Kunststoffen" im Ausschuss für Technik des DVS-Deutscher Verband für Schweißen und Verwandte Verfahren eV, Düsseldorf*. DVS Media, 2006.

[98] Nabanita Banik. A review on the use of thermoplastic composites and their effects in induction welding method. *Materials Today: Proceedings*, 5(9):20239–20249, 2018.

[99] Melvin Avrami. Granulation, phase change, and microstructure kinetics of phase change. III. *The Journal of Chemical Physics*, 9(2):177–184, feb 1941.

[100] B Wunderlich. Vol. 2: Crystal nucleation, growth, annealing. macromolecular physics, 1976.

[101] W Banks, A Sharples, and JN Hay. The effect of simultaneously occurring processes on the course of polymer crystallization. *Journal of Polymer Science Part A: Polymer Chemistry*, 2(9):4059–4067, 1964.

[102] CW Price. Use of kolmogorov-johnson-mehl-avrami kinetics in recrystallization of metals and crystallization of metallic glasses. *Acta Metallurgica et Materialia*, 38(5):727–738, 1990.

[103] Stephen ZD Cheng and Shi Jin. Crystallization and melting of metastable crystalline polymers. *Handbook of thermal analysis and calorimetry*, 3:167–195, 2002.

[104] I. H. Hillier. Modified avrami equation for the bulk crystallization kinetics of spherulitic polymers. *Journal of Polymer Science Part A: General Papers*, 1965.

[105] Arnaldo T. Lorenzo, María Luisa Arnal, Julio Albuerne, and Alejandro J. Müller. DSC isothermal polymer crystallization kinetics measurements and the use of the avrami equation to fit the data: Guidelines to avoid common problems. *Polymer Testing*, 26(2):222–231, apr 2007.

[106] Sergey Vyazovkin. Modification of the integral isoconversional method to account for variation in the activation energy. *Journal of Computational Chemistry*, 22(2): 178–183, 2001.

[107] Sergey Vyazovkin. Nonisothermal crystallization of polymers: Getting more out of kinetic analysis of differential scanning calorimetry data. *Polymer Crystallization*, 1(2):e10003, 2018.

[108] John D Hoffman and JI Lauritzen. Crystallization of bulk polymers with chain folding-theory of growth of lamellar spherulites. *Journal of Research of the National Bureau of Standards*, 1(4):297–+, 1961.

[109] Akihiko Toda, Tatsuro Oda, Masamichi Hikosaka, and Yasuo Saruyama. A new method of analysing transformation kinetics with temperature modulated differential scanning calorimetry: application to polymer crystal growth. *Polymer*, 38 (1):231–233, 1997.

[110] Sergey Vyazovkin and Ion Dranca. Isoconversional analysis of combined melt and glass crystallization data. *Macromolecular Chemistry and Physics*, 207(1):20–25, 2006.

[111] Sergey Vyazovkin and Charles A Wight. Model-free and model-fitting approaches to kinetic analysis of isothermal and nonisothermal data. *Thermochimica acta*, 340:53–68, 1999.

[112] Henry L Friedman. Kinetics of thermal degradation of char-forming plastics from thermogravimetry. application to a phenolic plastic. *Journal of Polymer Science: Polymer Symposia*, 6(1):183–195, 1964.

[113] A Ortega. A simple and precise linear integral method for isoconversional data. *Thermochimica Acta*, 474(1-2):81–86, 2008.

[114] Sergey Vyazovkin. Some basics en route to isoconversional methodology. In *Isoconversional Kinetics of Thermally Stimulated Processes*, pages 1–25. Springer, 2015.

[115] Amandine Codou, Nathanael Guigo, Jesper van Berkel, Ed De Jong, and Nicolas Sbirrazzuoli. Non-isothermal crystallization kinetics of biobased poly (ethylene 2, 5-furandicarboxylate) synthesized via the direct esterification process. *Macromolecular Chemistry and Physics*, 215(21):2065–2074, 2014.

[116] Sergey Vyazovkin and Nicolas Sbirrazzuoli. Isoconversional approach to evaluating the hoffman–lauritzen parameters (u* and kg) from the overall rates of non-isothermal crystallization. *Macromolecular rapid communications*, 25(6):733–738, 2004.

[117] Nicolas Bosq, Nathanaël Guigo, Jacques Persello, and Nicolas Sbirrazzuoli. Melt and glass crystallization of pdms and pdms silica nanocomposites. *Physical Chemistry Chemical Physics*, 16(17):7830–7840, 2014.

[118] Jordi Farjas, Joan Pere López-Olmedo, and Pere Roura. Model-free isoconversional method applied to polymer crystallization governed by the hoffman-lauritzen kinetics. *Polymer*, 120:111–118, jun 2017.

[119] J Farjas and P Roura. Isoconversional analysis of solid state transformations. *Journal of thermal analysis and calorimetry*, 105(3):757–766, 2011.

[120] Scott T Holmes and John W Gillespie Jr. Thermal analysis for resistance welding of large-scale thermoplastic composite joints. *Journal of Reinforced Plastics and composites*, 12(6):723–736, 1993.

[121] Junghoon Cha, Jungki Seo, and Sumin Kim. Building materials thermal conductivity measurement and correlation with heat flow meter, laser flash analysis and tci. *Journal of thermal analysis and calorimetry*, 109(1):295–300, 2012.

[122] Günther Walther Heinrich Höhne, Wolfgang Hemminger, and H-J Flammersheim. Theoretical fundamentals of differential scanning calorimeters. In *Differential Scanning Calorimetry*, pages 21–40. Springer, 1996.

[123] Matthias Wagner. *Thermal analysis in practice*. Mettler Toledo, 2010.

[124] Rudolf Riesen. Choosing the right baseline. *User Com*, 25(1):1–6, 2007.

[125] John D Hoffman and James J Weeks. Melting process and the equilibrium melting temperature of polychlorotrifluoroethylene. *J Res Natl Bur Stand A*, 66(1):13–28, 1962.

[126] Xiaolin Wang, Jiuchun Yan, Ruiqi Li, and Shiqin Yang. Fem investigation of the temperature field of energy director during ultrasonic welding of peek composites. *Journal of Thermoplastic Composite Materials*, 19(5):593–607, 2006.

[127] AB Comsol. Ac/dc module–user's guide. *COMSOL*, 3:151, 2011.

[128] Andrea Saltelli, Paola Annoni, Ivano Azzini, Francesca Campolongo, Marco Ratto, and Stefano Tarantola. Variance based sensitivity analysis of model output. design and estimator for the total sensitivity index. *Computer Physics Communications*, 181(2):259–270, 2010.

[129] Stephen Joe and Frances Y Kuo. Remark on algorithm 659: Implementing sobol's quasirandom sequence generator. *ACM Transactions on Mathematical Software (TOMS)*, 29(1):49–57, 2003.

[130] Francesca Lionetto, Silvio Pappadà, Giuseppe Buccoliero, and Alfonso Maffezzoli. Finite element modeling of continuous induction welding of thermoplastic matrix composites. *Materials & Design*, 120:212–221, 2017.

[131] Yu K Godovsky and GL Slonimsky. Kinetics of polymer crystallization from the melt (calorimetric approach). *Journal of Polymer Science: Polymer Physics Edition*, 12(6):1053–1080, 1974.

[132] John Wyrill Christian. *The theory of transformations in metals and alloys*. Newnes, 2002.

[133] Kamyar Gordnian. *Crystallization and thermo-viscoelastic modelling of polymer composites*. PhD thesis, University of British Columbia, 2017.

[134] Shahab Kashani Rahimi and Joshua U Otaigbe. The role of particle surface functionality and microstructure development in isothermal and non-isothermal crystallization behavior of polyamide 6/cellulose nanocrystals nanocomposites. *Polymer*, 107:316–331, 2016.

[135] Arun K. Kalkar, Vineeta D. Deshpande, and Bhakti S. Vatsaraj. Isoconversional kinetic analysis of DSC data on nonisothermal crystallization: Estimation of hoffman-lauritzen parameters and thermal transitions in PET/MMT nanocomposites. *Polymer*, 55(26):6948–6959, dec 2014.

[136] Bruce Cassel, Robert Packer, and CT Shelton. Modulated temperature dsc and the dsc 8000: a step up in performance. *PerkinElmer, Inc. http://las. perkinelmer. com*, 2010.

[137] Theodore L Bergman, Frank P Incropera, David P DeWitt, and Adrienne S Lavine. *Fundamentals of heat and mass transfer*. John Wiley & Sons, 2011.

[138] Xiaosong Huang. Fabrication and properties of carbon fibers. *Materials*, 2(4): 2369–2403, 2009.

[139] B Kamala Priya, KMV Ravi Teja, et al. Modeling of frp composites for the prediction of effective thermal conductivity. *Materials Today: Proceedings*, 4(2):2832–2840, 2017.

[140] Haiqing Jiang, Zhibing Yi, Pan Cheng, Chuncai Kong, Mufang Li, Xiaojun Wang, Ke Liu, Hitoshi Takagi, Dong Wang, and Zhimao Yang. Modified thermal resistance networks model for transverse thermal conductivity of unidirectional fiber composite. *Composites Communications*, 6:52–58, 2017.

[141] Ich-Long Ngo and Chan Byon. A generalized correlation for predicting the thermal conductivity of composite materials. *International Journal of Heat and Mass Transfer*, 83:408–415, 2015.